Time-dependent density functional tight binding combined with the Liouville-von Neumann equation applied to AC transport in molecular electronics

Dissertation

zur Erlangung des Doktorgrades
der Naturwissenschaften (Dr. rer. nat.)
der Fakultät für Physik
der Universität Regensburg

vorgelegt von
Christian Oppenländer
aus
Regensburg
im Jahr 2014

Die Arbeit wurde angeleitet von: Prof. Dr. Thomas Niehaus
Das Promotionsgesuch wurde eingereicht am: 07.10.2014
Das Promotionskolloquium fand statt am: 23.01.2015

Prüfungsausschuss:

Vorsitzender: Prof. Dr. Jascha Repp
1. Gutachter: Prof. Dr. Thomas Niehaus
2. Gutachter: Prof. Dr. Klaus Richter
weiterer Prüfer: Prof. Dr. Karsten Rincke

Korrekturen/Änderungen zur ursprünglich eingereichten Version:

- S. V: Inhaltsverzeichnis aktualisiert.
- S. 59: Achsenbeschriftung zur Grafik 3.17. korrigiert von "'Gridpoint in carbon chain"' zu "'Grid point in Al-benzenediol-Al device"'.
- S. 79: Grafik 4.7. zeigte nicht die beschriebenen Daten und wurde ersetzt.
- S.101: Danksagungen wurden hinzugefügt.

List of publications:

[1] Christian Oppenländer, Björn Korff, Thomas Niehaus.
Higher harmonics and ac transport from time dependent density functional theory.
Journal of Computational Electronics, 12(3), 420-427. (2013)

[2] Christian Oppenländer, Björn Korff, Thomas Frauenheim, Thomas Niehaus.
Atomistic modeling of dynamical quantum transport.
physica status solidi (b), 250(11), 2349-2354 (2013)

[3] Christian Lotze, Jingcheng Li, Coral Herranz-Lancho, Gunnar Schulze, Martina Corso, Setianto, Christian Oppenländer, Mario Ruben, Katharina J. Franke, Alessandro Pecchia, Thomas A. Niehaus, Jose Ignacio Pascual.
The effect of conformational flexibility on the electrical transport through flexible molecules.
to be published.

Contents

Introduction

Molecular electronics is the bottom-up approach to the ultimate miniaturization of circuits, using individual molecules as the basic building blocks [1, 2]. While the idea itself is many decades old, only recently we have gained the experimental and theoretical capabilities necessary to do basic research in this field. Compared to silicon-based electronics, the long term goal is to provide a smaller, faster, cheaper and more flexible alternative. Even if it eventually turns out that conventional architectures cannot be efficiently replaced, a lot of valuable insight into novel quantum transport phenomena will have been gained. Today, an interdisciplinary field has emerged, combining efforts of mesoscopic physics, chemistry, material science and electrical engineering among others.

Modern molecular electronics were arguably born by the work of Aviram and Ratner [3] showing how single molecules can act as rectifiers. Due to the lack of fitting experimental techniques, a dry spell followed, which recently made way for tremendous progress: on the experimental side, the invention of the scanning tunneling microscope provided the tool to measure the conductance of single molecules. Although still a big challenge due to the large fluctuations in the acquired data, these measurements were carried out successfully, also using techniques like mechanically controlled or electrochemical break junctions. Early attempts of describing the new phenomena theoretically were succeeded by the development of the non-equilibrium Green's function formalism. Its application to quantum transport through molecules was predominantly pioneered by Landauer, Büttiker, Meir and Wingreen. Especially when combined with sophisticated electronic structure descriptions like density functional theory, the resulting ab-initio predictions are reasonably close to experiment and became today's standard.

Within molecular electronics, time-dependent phenomena are an appealing topic due to the possibility of manipulating the current in a junction, i.e. enhancing or decreasing the conductance by an external electromagnetic field [4, 5]. It may be possible to create optoelectronic elements like photoswitches and contacted molecules can be identified by their optical properties when emitting [6]. Below the respective plasma frequency, the laser induces an oscillating voltage of unknown amplitude in the leads and can therefore be modelled by an ac voltage under the assumption that only the leads are absorbing. This makes it possible to investigate interesting questions regarding rectification processes (also called photon-assisted tunneling), the formation of higher harmonics in the current trace or the dependence of the ac current on the incident frequency. Radiation-induced dc currents have been observed in molecular junctions by STM experiments, predominantly in the microwave regime [7], but also for optical frequencies [8], and confirmed to at least partially originate from rectification processes. For the theoretical interpretation of these experiments, the heuristic approach of Tien and Gordon is largely still in use [9], combined with a dc transmission usually calculated within density functional theory. Due to the limited accessibility, experimental data on admittance properties is much more scarce and detailed theoretical discussions are ahead of their validation.

In order to describe quantum transport with harmonic oscillations in the bias theoretically, one can choose between frequency domain and time domain approaches. Using suitable approximations and for small voltages and bias amplitudes, it is possible to write down compact equations in frequency space similar to the standard time-independent Landauer formalism [10]. On the other hand, time-resolved approaches are much more flexible: their time-dependent bias profile is not limited to harmonic oscillations, the respective amplitude can be far away from linear response, and in the case of ac transport, the frequency may be chosen in otherwise inaccessibly high regimes. Also, additional information like transients induced by switching on the bias is included. The approaches to transport may then be combined with first-principles electronic structure theory. Especially, time-dependent density functional theory (TD-DFT) has become very popular in recent years due to its efficiency that allows for realistic lead-molecule-lead systems to be calculated [11, 12, 13]. Again, there are numerous ways to describe dynamical transport using TD-DFT. One idea is to treat the whole system as a finite cluster and propagate the Kohn-Sham states through time [14, 15]. However, there are disadvantages: unphysical current oscillations persist even for large evolution times and a steady state is only transiently reached. The approach we choose is partitioning the whole system into semi-infinite leads and a device region including layers of lead material, very similar to standard time-independent DFT-NEGF Landauer calculations. Using TD-DFT, numerous efforts in this direction have been made before [16, 17, 18]. Since any calculation resolving the electron dynamics in a realistic system is very time-consuming, instead of DFT we use its tight-binding approximation TD-DFTB [19] to be able to calculate current traces of large systems efficiently. [20]

In Chapter 1, the necessary theoretical background will be reviewed. This includes the tight-binding approximation to density functional theory, which is later combined with an equation of motion approach for the device density matrix, derived in the framework of the non-equilibrium Green's function formalism. In order to treat time-dependent systems, some modifications to the ground state approach have to be made, especially the solution of the Poisson equation in each time step to obtain a time-dependent potential profile. These modifications along with notes about the implementation in our code including example calculations are the topic of Chapter 2. The first of the time-dependent phenomena, the dependence of the current response amplitude on the incident frequency, is discussed in Chapter 3. Interesting questions include the information on admittance properties provided by the dc transmission, the distinction of capacitive versus inductive systems, the influence of the device potential profile and the application of the model on quantum capacitors. In Chapter 4, we investigate photon-assisted tunneling, improving on many limitations of the standard Tien-Gordon approach. The occurrence of higher harmonics and the validity of quasi-static approximations to the current response are briefly touched. Finally, Chapter 5 is reporting on a joint experimental and theoretical project in which a large, flexible molecule is lifted off a copper surface and experiences characteristic jumps in its conductance.

Chapter 1

Theoretical foundation

1.1. Electronic structure theory

1.1.1. Density functional theory

Since one of the projects discussed below uses density functional theory (DFT) directly and it is also the basis of the electronic structure method we are employing in our code, this section will contain a brief review. For further details, please turn to one of the many comprehensive reviews published by the community, for example ref. [21]. and especially [22]. For DFT in the larger context of computational chemistry, see ref. [23].

Although earlier theories using density functionals exist, the main achievement lay in the two Hohenberg-Kohn theorems [24] and the Kohn-Sham equations [25] which made them a proper tool for electronic structure calculations.

Hohenberg-Kohn theorems

In many-body quantum theory, the whole information about a quantum-mechanical system is embedded in the many body wave function $\Psi_{tot}(\mathbf{r}_1, \ldots, \mathbf{r}_N, \mathbf{R}_1, \ldots, \mathbf{R}_M)$, which depends on the coordinates of all the electrons $\mathbf{r}_i$ and nuclei $\mathbf{R}_\alpha$. In the (usually very good) Born-Oppenheimer-approximation, one only has to solve for the electronic wave function Ψ, which is assumed to only depend on the coordinates of the electrons.

In principle, the exact Ψ for a molecule or solid could be calculated for an arbitrary non-relativistic Hamiltonian out of the time-independent Schrödinger equation [1]

$$\left[\sum_i \left(-\frac{\nabla_i^2}{2} - \sum_\alpha \frac{Z_\alpha}{|\mathbf{r}_i - \mathbf{R}_\alpha|}\right) + \sum_{i<j} \frac{1}{|\mathbf{r}_i - \mathbf{r}_j|}\right] \Psi(\mathbf{r}_1, \ldots, \mathbf{r}_N) = E\Psi(\mathbf{r}_1, \ldots, \mathbf{r}_N) \quad (1.1)$$

where Z_α is the atomic number of the respective element with core α. For a non-relativistic Coulomb-interacting system, the characterizing part is the external potential $V_{ext} = \sum_i v_{ext}(\mathbf{r}_i) = -\sum_{i\alpha} \frac{Z_\alpha}{|\mathbf{r}_i - \mathbf{R}_\alpha|}$. The various possible systems only differ by this part of the Schrödinger equation if N is given.

Now, DFT states that you can use the ground-state electron density $\rho_G(\mathbf{r})$ - which is an observable - as the system-determining quantity instead of the external potential, and all the other ground state quantities (including Ψ) become *functionals of the electronic density*. This is a non-trivial suggestion since the electronic density is a function of only one vectorial variable, while Ψ depends on N vectorial variables. The many-body problem is formally reduced to a one-particle problem depending on ρ implicitly including the information of the many-body problem. Besides its versatility, the main reason for the success of DFT stems from the fact that the transition to densities hides information which is usually not relevant, but still gives access to good approximations to quantities which are, like the total energy and as a consequence, geometries, spectra etc., resulting in an excellent ratio of practical usefulness to computational cost.

The constrained search [26] algorithm is looking for the ground state wave function Ψ_G, which - according to the variational principle - minimizes the energy in potential v_{ext}, $E_{v_{ext},G}$, and at the same time yields the ground state electronic density ρ_G, which is stated as an additional condition in the minimization:

$$E_{v_{ext},G} = \min_{\Psi_G \to \rho_G} \langle \Psi | T + U + V_{ext} | \Psi \rangle = \min_{\Psi_G \to \rho_G} \langle \Psi | T + U | \Psi \rangle + \int d^3 r \rho_G(\mathbf{r}) v_{ext}(\mathbf{r}) \quad (1.2)$$

$T = T[\rho]$ and $U = U[\rho]$ are so-called universal functionals, since they are independent of the external potential. Due to the conceptual equality of the information included in Ψ_G and ρ_G, the usual variational principle also extends to the energies calculated out of the electronic densities. This fact is usually called the second HK-theorem.

$$E[\rho] \geq E[\rho_G] \quad (1.3)$$

---

[1] Throughout this thesis, atomic units will be used.

In order to find the variational minimum of $E[\rho]$, one needs reasonable approximations to the explicit form of $T[\rho]$ and $U[\rho]$, which is a highly non-trivial issue.

Kohn-Sham DFT

Kohn and Sham addressed the first challenge of finding a suitable $T[\rho]$ [25] and also gave the whole theory the form of single-particle equations. In the general case, the electronic density corresponds to an interacting system with a kinetic energy of T_{full}. In Kohn Sham theory, this quantity is approximated by the kinetic energy T_{KS} which would emerge from a non-interacting system which yields the same density as the interacting one. This hypothetical non-interacting system has - apart from Koopman's theorem [27] for exact DFT - no apparent physical meaning. In this approach, the kinetic energy is simply the sum of the kinetic energies of non-interacting particles in an effective potential specified by the interacting system to be modeled. Note that T_{KS} becomes an implicit functional of ρ and direct minimization isn't possible anymore.

$$T_{KS}(\psi[\rho]) = -\frac{1}{2}\sum_{i}^{N}\int \psi_i^*(\mathbf{r})[\rho]\nabla^2\psi_i(\mathbf{r})[\rho]d^3r \tag{1.4}$$

As pointed out in [22], there are various ways to understand the approximation made here. Perhaps the most plastic one is that a wave function being a single slater determinant built out of single particle orbitals $\psi[\rho]$ cannot represent a full many body wave function, since it ignores the effect that electrons strive to avoid each other. If the many-body wave function is a product of single particle orbitals, this simple probability superposition implies that the orbitals are independent of each other - in other words: it ignores electron correlation. The correlation part of the kinetic energy, $T_{corr} = T_{full} - T_{KS}$, is put into a term called the exchange-correlation energy E_{XC} together with all interaction effects going beyond the Hartree term U_H:

$$U_H[\rho] = \frac{1}{2}\int d^3r \int d^3r' \frac{\rho(\mathbf{r})\rho(\mathbf{r}')}{|\mathbf{r}-\mathbf{r}'|} \tag{1.5}$$

$$E_{XC} = (T_{full} - T_{KS}) + (U - U_H) \tag{1.6}$$

Every information lost by approximating exact DFT resides in approximations to this term. If it was known exactly, one could in principle calculate the full many body wave function out of the electronic density. It may be assumed that this is equally next-to-impossible as solving the Schrödinger equation itself.

However, the great advantage of DFT is that E_{XC} is small and even rough approximations work with very good efficiency. One can also tailor the various approximations in a way suitable for the systems and quantities under study.

E_{XC} may be decomposed in an exchange and correlation part, but as described in [23], one cannot calculate the exchange part from wave mechanic methods and use it in DFT, since its definition is different. In DFT, the definitions of exchange and correlation are short-range only - they depend on the given point in space and the immediate vicinity around it. In wave mechanics however, both exchange and correlation have a long-range part (also called "‘static"’ correlation) which cancels out. Calculating exchange with wave mechanic methods and correlation with DFT, this cancellation does not longer work and leads to poor results [28].

Kohn-Sham equations

The non-interacting auxiliary system consists of single-particle equations using an effective potential:

$$\left[-\frac{1}{2}\nabla^2 + v_{KS}(\mathbf{r})\right]\psi_i(\mathbf{r}) = \epsilon_i \psi_i(\mathbf{r}) \tag{1.7}$$

$$v_{KS} = v_{ext} + v_H + v_{XC} \tag{1.8}$$

where v_{ext} is the potential one would like to solve the many-body system for, v_H is the Hartree potential and $v_{XC} = \frac{\delta E_{XC}[\rho]}{\delta\rho}$. Note that the symbol δ means a *functional derivative*. The density solving this set of single-particle Schrödinger equations is equal to the density minimizing the energy functional, thus all that is left to be done is solving these *Kohn-Sham equations*. Since the electronic density is calculated from the occupied orbitals (the lowest N spin-eigenfunctions are filled),

$$\rho(\mathbf{r}) = \sum_i^{occ} |\psi_i(\mathbf{r})|^2 \tag{1.9}$$

while the effective potential and thus the orbitals are modified by the electronic density via:

$$\frac{\delta(V_{ext}[\rho] + U_H[\rho] + E_{XC}[\rho])}{\delta\rho} = v_{KS}(\mathbf{r}) \tag{1.10}$$

These equations have to be solved self-consistently. Once convergence has been reached, all relevant observables can be calculated from the obtained approximate ground state electronic density. With $E_{KS} = T_{KS} + \int d^3 r v_{KS}(\mathbf{r}) = \sum_i^N \epsilon_i$ (note that the total energy of the KS-system is not the total energy of the interacting system), one can easily derive a good-to-handle formula for the ground state energy E_G:

$$E_G = \sum_i^N \epsilon_i - \underbrace{\frac{1}{2}\int\int d^3r d^3r' \frac{\rho_G(\mathbf{r})\rho_G(\mathbf{r}')}{|\mathbf{r}-\mathbf{r}'|}}_{U_H[\rho_G]} - \int d^3 r v_{XC}(\mathbf{r})\rho_G(\mathbf{r}) + E_{XC}[\rho_G] \quad (1.11)$$

General DFT performance and used XC functionals

One of the main reasons DFT performs very well even for quantities which scale at tiny fractions of the total energy (like cohesive energies) is that most of the error the standard XC functionals make is systematic and benefits from error correction. One has to be careful comparing properties in reactions involving phase transitions or other significant system changes, though. Obviously, since DFT is formally exact, the key quantity for the accuracy - apart from numerical limitations - is the XC functional one decides to use.

Local density approximation

The LDA is a very crude, simple approximation and still works surprisingly well. It assumes that the density varies slowly and the resulting exchange energy E_X^{LDA} can be described as the one of an uniform electron gas [26] [29]:

$$E_X^{LDA}[\rho] = -\text{const} \cdot \int d^3 r \rho(\mathbf{r})^{\frac{4}{3}} \quad (1.12)$$

The correlation part E_C^{LDA} of the LDA is added from quantum monte carlo simulations, and the available methods [30] [31] yield very similar results. It systematically (!) underestimates E_X by about 10% [23], yet overestimates E_C, and therefore benefits from error correction in most systems.

Important for later discussions is the characteristic of LDA to overbind molecules and solids. Binding energies are generally too large, leading to lattice constants and molecular binding distances about 1-3 % too small. But since these deviations are systematic, comparisons between similar systems can still be very good. Since LDA is local, it fails to describe Van-der-Waals interactions which leads to error correction with the general overbinding.

Generalized gradient approximations

As mentioned, LDA takes the density to be constant in the vicinity of the space point it is evaluated at. GGAs include information about the change in density close to the evaluation point. These functionals are often called semi-local, but since they mathematically only depend on one space-point, it makes more sense to also call them local. The general form of these functionals is:

$$E_{XC}^{GGA}[\rho] = \int d^3r f(\rho(\mathbf{r}), \nabla\rho(\mathbf{r})) \tag{1.13}$$

While it could be stated there is only "one" LDA, this is entirely untrue for GGAs. They differ in the amount of empirical parameters, assumptions and their entire functional form within the general concept. GGAs yield binding energies closer to the experimental results, but their error is less systematic: although they usually under-bind, they can also overbind. This leads to problems when comparing systems in which the functional behaves differently. In our code for time-dependent calculations, we choose to build our DFTB Hamiltonian using the GGA functional PBE [32] for its overall good performance.

1.1.2. Density functional tight-binding

Although DFT is fast compared to wave function methods, the quantum mechanical treatment of larger systems is still a tedious business, and especially time-dependent approaches can become very expensive. There is room for another (reasonable) approximation, and despite its crude appearance, DFTB is a sophisticated approach towards a quantum mechanical description narrowing the gap in computational cost between DFT and force field methods.

Tight-binding

Tight-binding approaches became common due to Slater and Koster in 1954 [33] who approximated the full LCAO (linear combination of atomic orbitals) method for solids. The exact many-body Hamiltonian is approximated by parametrized matrix elements. The wave function is expanded into atomic-like orbitals ϕ_ν located at center α which are not necessarily solutions to the atomic problem, but share the same symmetries. Since they are non-orthogonal in the general case, they have to be transformed to an orthogonal basis by a Löwdin transformation using their overlap matrix S:

$$\psi_{\alpha\nu} = \sum_{\alpha'\nu'} S^{-1/2}_{\alpha\alpha'\nu\nu'} \phi_{\alpha'\nu'} \tag{1.14}$$

For a solid, the Hamiltonian is now written in Bloch sums over the atomic orbitals as

$$H_{\nu\alpha,\mu\beta} = \sum_{\mathbf{R}_\beta} e^{i\mathbf{k}(\mathbf{R}_\beta - \mathbf{R}_\alpha)} \int d\mathbf{r} \psi^*_{\nu\alpha}(\mathbf{r} - \mathbf{R}_\alpha) H \psi_{\mu\beta}(\mathbf{r} - \mathbf{R}_\beta) \tag{1.15}$$

The various different tight-binding models have in common that the integral in the above equation is replaced by a parameter which only depends on the distance $|\mathbf{R}_\alpha - \mathbf{R}_\beta|$ between two centers and the symmetry of the respective orbitals [34]. The first assumption implies the two center approximation, which states that all matrix elements connecting three or more centers are neglected.

If the method is to be used on a finite system, a total energy expression is needed. In addition to the bandstructure term E_{BS}, a repulsive energy resulting from a sum of pair terms is used to approximate the terms not included in the bandstructure energy, yielding a tight-binding total energy E_{TB} as [35].

$$E_{TB} = \underbrace{\sum_{i=1}^{N} \epsilon_i}_{E_{BS}} + \frac{1}{2} \sum_{\alpha} \sum_{\alpha \neq \beta} E_{rep}(|\mathbf{R}_\alpha - \mathbf{R}_\beta|) \tag{1.16}$$

where the first term is the sum of the occupied single electron energy eigenvalues of the above Hamiltonian and the second term is the repulsive correction which also depends only on the distance between two centers. All terms which do not fit in this form are neglected. Most tight-binding approaches and especially the classical ones are semi-empirical, they use a set of parameters given by experiment to build up the necessary terms for calculating the total energy, leading to limited transferability. However, the scheme is very fast since there are few things to calculate at runtime.

DFTB

The idea is now to find transferable parameter sets from DFT with ab-initio functionals, making the whole TB-approach completely free of experimental data, while keeping the advantage of in this case pre-calculated look-up tables to considerably speed up the calculations.

It is not straightforward why casting DFT into the tight-binding form and dropping all self-consistency should be a reasonable approximation, for a justification see [36]. In short, DFTB can be seen as a stationary approximation to DFT. At the core of DFTB is an expansion of the total energy expression around a reference density ρ_0, which takes the following form [36] [37]:

$$E_{DFTB} = \sum_i^{occ} \langle \psi_i | H_0 | \psi_i \rangle - \frac{1}{2} \int \int' d^3r d^3r' \frac{\rho_0' \rho_0}{|\mathbf{r} - \mathbf{r}'|} + E_{XC}[\rho_0] - \int d^3r v_{XC}[\rho_0]\rho_0 \tag{1.17}$$

$$+ \frac{1}{2} \sum_{\alpha,\beta}^{M} \frac{Z_\alpha Z_\beta}{|\mathbf{R}_\alpha - \mathbf{R}_\beta|} + \frac{1}{2} \int \int' \left(\frac{1}{|\mathbf{r} - \mathbf{r}'|} + \frac{\delta^2 E_{XC}}{\delta\rho\delta\rho'}\Big|_{\rho_0} \right) \delta\rho\delta\rho' ... \tag{1.18}$$

where H_0 is a non-self-consistent DFT Hamiltonian evaluated at the reference density. The last term is the second order contribution and constitutes second order DFTB or *self consistent charge (SCC)* DFTB. Even without this term, the method performs quite well - however, in order to describe systems with large charge transfers, one has to self-consistently reposition the partial charges using this second order term [37]. For now, we concentrate on the zeroth order (there are no linear terms).

Applying the LCAO method on DFT,

$$\psi_i(\mathbf{r}) = \sum_\nu C_{\nu i} \phi_\nu(\mathbf{r} - \mathbf{R}_\alpha) \tag{1.19}$$

one has to solve the set of single particle Kohn Sham equations

$$\sum_\nu C_{\nu i} (\underbrace{\langle \phi_\mu | H | \phi_\nu \rangle}_{H_{\mu\nu}} - \epsilon_i \underbrace{\langle \phi_\mu | \phi_\nu \rangle}_{S_{\mu\nu}}) = 0 \tag{1.20}$$

with the mentioned (two-center) approximations to the Hamiltonian matrix, defining an effective potential $V_{eff}(\mathbf{r}) = V_{ext}(\mathbf{r}) + V_H[\rho(\mathbf{r})] + V_{XC}^{LDA}[\rho(\mathbf{r})]$:

$$H_{\mu\nu} = \begin{cases} \epsilon_\mu^{Atom} & \text{if } \mu = \nu \\ \langle \phi_\mu | T + V_{eff}[\rho_0^\alpha + \rho_0^\beta] | \phi_\nu \rangle & \text{if } \mu \in \alpha, \nu \in \beta \\ 0 & \text{otherwise} \end{cases} \tag{1.21}$$

In the two-center term, one can either choose a density superposition ($V_{eff}[\rho_0^\alpha + \rho_0^\beta]$) or a potential superposition ($V_{eff}[\rho_0^\alpha] + V_{eff}[\rho_0^\beta]$). In the case of our calculations, a density superposition is chosen.

If the expansion around ρ_0 is to be accurate, it has to be a good approximation to the density DFT calculations would yield. Therefore, ρ_0 is assumed to be a superposition of compressed atomic densities calculated within DFT. In molecules and solids, the electrons have less space to move, and therefore a compression term adds to a better description of the superposed densities. Furthermore, the atomic DFT calculations yield wavefunctions that can be used as a minimal set of basis functions which perform very well, since they in turn consist of multiple basis functions. The modified single-electron Kohn-Sham equations to calculate the pseudo-atomic orbitals read [19]:

$$\left[T + V_{eff}(\mathbf{r}) + \left(\frac{r}{r_0}\right)^2\right]\phi_\nu(\mathbf{r}) = \epsilon_\nu^{psat}\phi_\nu(\mathbf{r}) \tag{1.22}$$

with a compression radius r_0. The atomic-like orbitals are hereby written in terms of Slater-type orbitals (STOs) and spherical harmonics Ω_{lm} as [19]

$$\phi_\nu(\mathbf{r}) = \sum_{n,\beta,l_\nu,m_\nu} r^{l_\nu+n} e^{-\beta r}\Omega_{l_\nu m_\nu}\left(\frac{\mathbf{r}}{r}\right) \tag{1.23}$$

with the quantum numbers n, l, m and β being a parameter of which five different values have been shown to be a sufficient description for elements within the first three rows. [38]

Once the band structure energy has been calculated, the repulsive part can be fitted with a spline to self-consistent DFT calculations. The reference system used for the fit depends on the systems one would like to calculate with the DFTB approach. Generally, one can use diatomic molecules as a reference, but the closer the reference system of the fit is to the properties of the system DFTB is used for, the more accurate the repulsive part of the total energy will be. However, one can in principle access the full information contained in the self-consistent calculation.

$$E_{rep}(|\mathbf{R}_\alpha - \mathbf{R}_\beta|) = (E_{DFT} - E_{BS})|_{\text{reference system}} \tag{1.24}$$

Together with the spline, the Hamiltonian and Overlap ($S_{\mu\nu}$) matrices are stored for finite step sizes in the interatomic distance. Implementations of DFTB look up these tables - called Slater Koster (SK) files - and can immediately write down and diagonalize the matrices out of information about the system geometry.

SCC-DFTB

SCC-DFTB takes the next step towards a better description - especially of highly inhomogeneous systems - but reintroduces the need of a self-consistent cycle at runtime. The key arguments of Elstner et al. [37] will be restated here. First, one divides the density fluctuations into atom-centered parts $\delta\rho_\alpha$ and $\delta\rho_\beta$, writes down a multipole expansion into radial (F_{ml}) and angular (Ω_{lm}) parts, cutting after the monopole term:

$$\delta\rho_\alpha(\mathbf{r}) = \sum_{l,m} K_{ml} F^\alpha_{ml}(|\mathbf{r}-\mathbf{R}_\alpha|)\Omega_{lm}\left(\frac{\mathbf{r}-\mathbf{R}_\alpha}{|\mathbf{r}-\mathbf{R}_\alpha|}\right) \tag{1.25}$$

$$\approx \Delta q_\alpha F^\alpha_{00}(|\mathbf{r}-\mathbf{R}_\alpha|)\Omega_{00} \tag{1.26}$$

Here, Δq_α is the net charge on the respective atom and F^α_{00} the normalized spherical density fluctuation. Inserting this expansion into the 2nd order term yields the following form:

$$E_{2nd} = \frac{1}{2}\sum_{\alpha,\beta}^{N} \Delta q_\alpha \Delta q_\beta \gamma_{\alpha\beta} \tag{1.27}$$

$\gamma_{\alpha\beta}$ contains all quantities of the expansions excluding the net charges $\Delta q_{\alpha,\beta}$. According to [39], the on-site terms $\gamma_{\alpha\alpha}$ can be approximated by the difference between the atomic ionization potential I_α and electron affinity A_α of the atom centered at α, which again can be well approximated by the so-called Hubbard parameter U_α. This quantity can be calculated within DFT as follows:

$$U_\alpha = \frac{\partial^2 E_\alpha}{\partial n^2_{HOAO}} \approx I_\alpha - A_\alpha \tag{1.28}$$

where n_{HOAO} is the occupation number of the highest occupied atomic orbital and E_α the total energy of the neutral atom at α. In the limit of large distances, $\gamma_{\alpha\beta}$ shows a $\frac{1}{|R_\alpha - R_\beta|}$ behavior, the interaction is thus decaying into a purely Coulomb-like one with vanishing XC contributions. Ref. [37] describes the derivation of an analytical expression for $\gamma_{\alpha\beta}$ with the correct long range behavior. The authors assume an exponential decay of the density and determine the decay constant through the Hubbard parameters. The total energy expression now reads to second order of DFTB:

$$E_{2nd}(U_\alpha, U_\beta, |R_\alpha - R_\beta|) = \sum_i^{occ} \langle \phi_i | H_0 | \phi_i \rangle + \frac{1}{2} \sum_{\alpha,\beta}^{N} \gamma_{\alpha\beta} \Delta q_\alpha \Delta q_\beta + E_{rep} \tag{1.29}$$

In order to get the net charges Δq, one calculates the Mulliken charges as an approximation to the atomic charge and subtracts the charge of the neutral atom.

$$\Delta q_\alpha = \frac{1}{2} \sum_i^{occ} n_i \sum_{\mu \in \alpha} \sum_\nu^N (C^*_{\mu i} C_{\nu i} S_{\mu\nu} + C^*_{\nu i} C_{\mu i} S_{\nu\mu}) - q^0_\alpha \tag{1.30}$$

with $C_{\mu i}, C_{\nu i}$ being the expansion coefficients of the LCAO. The Kohn-Sham equations look the same as before, with an additional term in the Hamiltonian matrix.

$$H_{\mu\nu} = \langle \phi_\mu | H_0 | \phi_\nu \rangle + \frac{1}{2} S_{\mu\nu} \sum_\xi^N (\gamma_{\alpha\xi} + \gamma_{\beta\xi}) \Delta q_\xi \tag{1.31}$$

1.2. Transport using many-body perturbation theory

1.2.1. Green's functions

The goal of this section is to review the non-equilibrium Green's function (NEGF) formalism [40, 41] which is able to tackle a variety of even time-dependent transport scenarios. These include also interacting electrons in the device region (not within the leads) to all orders of perturbation theory and far away from equilibrium. The application of this NEGF (or Keldysh) formalism to static transport using a mean-field approximation like in the Landauer [42, 43] context is only a small part of what it is capable of and does not use its full potential. However, a combination of NEGF with DFT became a very popular approach also to static time-independent transport [44, 45] as explained below. Please note that in the whole theoretical introduction, we assume the overlap matrix $S_{\mu\nu} = \langle \phi_\mu | \phi_\nu \rangle$ of the atomic orbitals to be equal to the identity matrix for simplicity. The results must therefore be straightforwardly generalized to fit to the non-orthogonal basis sets in use by our DFTB implementation. The first part of this introduction roughly follows Ref. [46].

Basics

One first needs to introduce the simplest kind of Green's Functions for non-interacting single particles. In the mathematical sense, a Green's Function is a way to solve a linear differential equation and its usefulness is therefore not limited to the Schrödinger equation. However, in its context, the Green's Function operator G solves

$$\left(i\frac{d}{dt} - H\right) G^{r/a}(t) = \mathbb{1}\delta(t) \tag{1.32}$$

where $\mathbb{1}$ is the identity matrix and the r/a subscript indicates two solutions: The retarded Green's Function $G^r(t - t_0)$ propagates the state vector forward in time from t_0 to t. It includes information about the history of the entire system. Its counterpart, the advanced Green's Function $G^a(t - t_0)$, propagates the state backwards in time from t_0 to a t with $t < t_0$. It includes information about the future state of a system.

Formally, the solutions to the equations of motion for these Green's Functions look very much alike the time propagation operator for a time-independent Hamiltonian:

$$G^r(t - t_0) = \begin{cases} -ie^{-iH(t-t_0)} & t > t_0 \\ 0 & t < t_0 \end{cases} \tag{1.33}$$

$$G^a(t - t_0) = \begin{cases} 0 & t > t_0 \\ +ie^{-iH(t-t_0)} & t < t_0 \end{cases} \tag{1.34}$$

$$\tag{1.35}$$

Both solutions are connected via

$$[G^r(t)]^\dagger = G^a(-t) \tag{1.36}$$

In the following, $G^{r/a}(t)$ will refer to the Green's Functions defined by a Schrödinger equation with the full Hamiltonian of a system consisting of the kinetic term and a scattering potential $V(\mathbf{r})$:

$$H_{tot} = -\frac{1}{2}\nabla^2 + V(\mathbf{r}) \tag{1.37}$$

whereas $G_0^{r/a}(t)$ are solutions to the "'free"' Hamiltonian without any scattering potential. Note that this kind of Green's Functions does only depend on the time difference $(t - t_0)$ and it is therefore possible to Fourier transform them into energy space. However, in order to converge the integration, one has to add an exponential term $e^{\pm \eta t}$ with an infinitesimal $\eta > 0$ as shown below. The sign in front of this parameter is also the distinction between retarded and advanced Green's Functions in energy space.

$$G^r(E) = \int_{-\infty}^{+\infty} dt\, e^{iEt} e^{-\eta t} G^r(t) \tag{1.38}$$

One then easily obtains

$$G^r(E) = [E\mathbb{1} - H + i\eta]^{-1} \tag{1.39}$$
$$G^a(E) = [E\mathbb{1} - H - i\eta]^{-1} \tag{1.40}$$
$$\tag{1.41}$$

showing that these functions have poles at the energy eigenvalues of the respective Hamiltonian.

Self-Energy and the Dyson equation

In general, the self-energy Σ describes the effects of an interaction with its environment on the energy of a single particle. Treating the interactions as a perturbation series, one can visualize them as Feynman diagrams as known from quantum field theory. What exactly the self-energy is describing depends on what is defined as the environment. It could only include the effects of leads on a nanodevice with non-interacting electrons like in the Landauer approach, or it could additionally include the effects of electron-electron and/or electron-phonon interactions on the single particles subjected to them. If the perturbative series is converging, there is a finite self-energy one can - in principle - calculate and modify the single particle energies so they contain all the respective interactions.

In the context of Green's Functions, one can easily calculate $G_0^{r/a}$ for an unperturbed Hamiltonian, but needs $G^{r/a}$ for the description of the system. The relation between the two depends on the interactions added by the perturbation and thus on the self-energy. The important Dyson equation [2] is stating exactly this:

---

[2] Which equations are called "Dyson equation" is not uniform in the literature. The true, most general Dyson equation looks very similar to the equation given here but contains operators defined by many-body perturbation theory, unlike the simple Green's Functions in this section. It is able to describe interacting systems out of equilibrium as stated in the NEGF sections.

$$G^{r/a}(t-t_0) = G_0^{r/a}(t-t_0) + \int_{t_0}^{t} dt' \int_{t_0}^{t'} dt''\, G_0^{r/a}(t-t')\Sigma^{r/a}(t'-t'')G^{r/a}(t''-t_0) \tag{1.42}$$

$$= G_0^{r/a}(t-t_0) + \int_{t_0}^{t} dt' \int_{t_0}^{t'} dt''\, G^{r/a}(t-t')\Sigma^{r/a}(t'-t'')G_0^{r/a}(t''-t_0) \tag{1.43}$$

The integration sums up interactions for an ingoing propagator at t_0 which is affected by interactions at the intermediate times and becomes the outgoing propagator at time t. One can extract the orders of the perturbation by attempting an iterative solution: set $G^{r/a} = G_0^{r/a}$ (Born approximation) and keep re-inserting the so-calculated approximative full Green's Function into the Dyson equation. This way the equation is transformed into an infinite series.

In the case of the mean-field approximation employed in the Landauer formalism, the self-energy is simply the scattering potential:

$$\Sigma(t'-t'') = V\delta(t'-t'') \tag{1.44}$$

and the Dyson equation reduces to the Lippmann-Schwinger equation in the scattering context:

$$G^{r/a}(t-t_0) = G_0^{r/a}(t-t_0) + \int_{t_0}^{t} dt'\, G_0^{r/a}(t-t')VG^{r/a}(t'-t_0) \tag{1.45}$$

$$= G_0^{r/a}(t-t_0) + \int_{t_0}^{t} dt'\, G^{r/a}(t-t')VG_0^{r/a}(t'-t_0) \tag{1.46}$$

Generally, if the Green's functions only depend on time differences, the Dyson equation can be transformed into energy space, where it looks more convenient.

$$G^{r/a}(E) = G_0^{r/a}(E) + G^{r/a}(E)\Sigma^{r/a}(E)G_0^{r/a}(E) \tag{1.47}$$

More importantly, there is an alternative form of the Dyson equation often encountered,

$$G^{r/a}(E) = \left[E\mathbb{1} - H - \Sigma^{r/a}(E) \mp i\eta\right]^{-1} \tag{1.48}$$

which nicely shows how the self-energy affects (renormalizes) the single-particle energies at the poles of the Green's function defined by the Hamiltonian eigenvalues. The real part adds a shift to the energy levels and the imaginary part adds a lifetime for these states to which it is inversely proportional. In the above case of a full unpartitioned mean-field system Hamiltonian, the imaginary part of the self-energy is zero and consequently, the lifetime of the states is infinite. The real part here adds a rigid shift which is not energy dependent.

However, it is important to realize here that this shape of the self-energy only applies to a scattering system which is described as a whole by a full Hamiltonian and not partitioned into leads and device region. For all practical purposes we only want to describe a device region artificially coupled to semi-infinite leads, as described in the next section. In this case, the self-energy looks different even in a Landauer scattering approach using the mean-field approximation, since now it describes the effect of the interaction with the leads on the energies of single electrons within the device only.

Standard partitioning

As mentioned in the last section, the two-probe systems we would like to investigate are usually partitioned into a device region (D) and two semi-infinite leads, left (L) and right (R). The device region itself consists of a molecule or an atomic chain which will be called inner device (ID) and a few layers of lead material (see Fig. 1.1). Adding lead material provides screening at the interfaces and a smoother potential transition to the semi-infinite leads that are assumed to be uniform. The coupling between leads and device is mediated by short-ranged off-diagonal blocks of the system Hamiltonian, T_{LD} and T_{RD}.

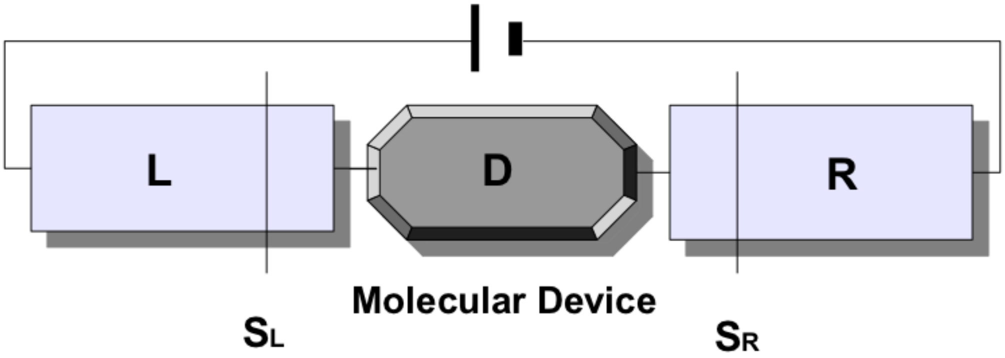

Figure 1.1: Schematic of the setup. The device region is connected to the left and right semi-infinite lead by open boundary conditions. The device contains lead material, the current is measured at the interfaces S_L, S_R.

The Hamiltonian may then be partitioned (in matrix notation) as

$$\begin{pmatrix} H_L & T_{LD} & 0 \\ T_{LD}^{\dagger} & H_D & T_{RD}^{\dagger} \\ 0 & T_{RD} & H_R \end{pmatrix} \begin{pmatrix} |\phi_L\rangle \\ |\phi_D\rangle \\ |\phi_R\rangle \end{pmatrix} = E \begin{pmatrix} |\phi_L\rangle \\ |\phi_D\rangle \\ |\phi_R\rangle \end{pmatrix} \tag{1.49}$$

and inserting the Green's Functions of the lead regions as

$$G_{L,R}^{r/a} = \left[E\mathbb{1} - H_{L,R} \pm i\eta\right]^{-1} \tag{1.50}$$

leaves us, after solving the system of equations, with an expression for $|\phi_D\rangle$:

$$[E\mathbb{1} - H_D - \underbrace{T_{LD}^{\dagger} G_L^{r/a}(E) T_{LD}}_{\Sigma_L^{r/a}(E)} - \underbrace{T_{LR}^{\dagger} G_R^{r/a}(E) T_{RD}}_{\Sigma_R^{r/a}(E)}]\,|\phi_D\rangle = 0 \tag{1.51}$$

Comparing with the definition of the non-interacting single-particle Green's function and the alternative form of the Dyson equation leads to an identification of the self energy terms as shown in the curly brackets above.

$$G^{r/a}(E) = \left[E\mathbb{1} - H_D - \Sigma_L^{r/a}(E) - \Sigma_R^{r/a}(E)\right]^{-1} \tag{1.52}$$

Please note the difference between the Green's function of the isolated device region $G_C^{r/a}$ and the Green's function of the device region in the presence of the leads $G^{r/a}$, the one we are looking for.

So, in order to obtain $G^{r/a}$, we need the coupling terms of the Hamiltonian and the Green's functions of the leads. Since the leads are assumed semi-infinite, this is not straightforward. However, there are methods to calculate a so-called surface Green's function which uses the periodicity of the leads to obtain a finite function. It can then be used to calculate the self-energy and thus the device Green's function which contains all the information about the transport properties. Along the transport direction, the leads are divided up in identical principal layers which only interact with their nearest neighbor layer. Since there is also one principal layer of lead material in the device region, the coupling block between device and lead is restricted to one lead principal layer and almost identical to the repeating coupling between two lead layers. Therefore, only the surface block of the lead Green's functions is needed to obtain the self-energy. How exactly the surface Green's functions are being calculated will be explained in section 3.2.2.

For now, let us review the consequences of the system partitioning on the shape of the self-energy and the implications of that. The real part of $\Sigma^{r/a}_{L/R}$ and therefore the energy shift is generally energy-dependent. More importantly, the self energy will acquire an imaginary part adding a finite lifetime to the states in the device, describing a scattering from the device into the leads. We define the energy-dependent scattering rates

$$\Gamma_{L,R}(E) = -2\mathrm{Im}\{\Sigma^{r}_{L,R}(E)\} \tag{1.53}$$

This is equivalent to a broadening of the level in energy space, which is why the $\Gamma = \Gamma_R + \Gamma_R$ will frequently be called linewidth or broadening (matrix).

Note that the partitioning does not add any new physics at all, and the different shape of the self-energy is only due to the fact that we are looking at a part of the system only. Of course, the same energy level shift and broadening would also be there if one looks at the full unpartitioned Hamiltonian - but it would be well hidden in a massive Green's function for the whole system and not be describable by self-energies.

Landauer transmission using Green's functions

At this point it is possible to derive an explicit Landauer transmission using the Green's functions we introduced. In the literature, this expression is frequently derived employing the NEGF formalism, but employing the same approximations as the derivation via the scattering approach. Especially this means that we are looking at a time-independent steady state, interactions are only treated at mean-field level and we have no electron-electron interactions explicitly included. An equation for the current I through the the junction from left to right of the form

$$I = \frac{1}{\pi}\int_{-\infty}^{+\infty} dE\,[f_L(E) - f_R(E)]\,T(E) \tag{1.54}$$

is called "Landauer formula" when the transmission function T(E) can be written in this simple form only dependent on energy. f_L and f_R denote the Fermi functions of the respective lead subjected to a voltage V. At zero temperature, they are equal to one at $E_F \pm \frac{eV}{2}$, respectively, and equal to zero above the respective energies, defining a bias window. The NEGF formalism is able to additionally derive an equation that also describes a scattering approach, but with interacting electrons in the device region (not in the leads though). The resulting equation is often referred to as Meir-Wingreen formula or extended Landauer formula [47].

Without introducing NEGF and employing many-body perturbation theory, it is still possible to derive the following Landauer-type expression by the use of the Fisher-Lee-relations [48] which create a connection between the Green's functions and the scattering matrix of the usual wave-function-based scattering approach.

$$I = \frac{1}{\pi} \int_{-\infty}^{+\infty} dE \, [f_L(E) - f_R(E)] \, \mathrm{Tr}[\Gamma_R G^r \Gamma_L G^a] \tag{1.55}$$

Comparison with 1.54 identifies the transmission function. The current is determined by the trace over a matrix with the dimension of the number of orbitals in the device region. Using NEGF in the time-independent non-interacting limit will yield the same expression. It is the main equation for static single-electron Landauer transport.

1.2.2. Keldysh formalism

Preparation: equilibrium

In order to use Green's functions to go beyond static non-interacting transport, one has to employ many-body perturbation techniques. The resulting propagators are not simply a solution to a linear differential equation as the functions introduced before, but are nevertheless called by the same name. Specifically, they may contain averages over four or more field operators and there exists no corresponding closed differential equation that the respective Green's function can solve [49]. One should therefore view many-body Green's functions as a different object which still share many of the features of their non-interacting single-particle version.

NEGF is exact for time-dependent closed systems (which may have open boundary conditions, but they must not be "open" in the sense that Hamiltonian dynamics are not valid anymore) and far away of equilibrium. It uses all orders of perturbation theory, but obviously the description breaks down once used in cases where many-body perturbation theory isn't applicable at all, like the Kondo effect. Since the Keldysh formalism is a natural extension to equilibrium many body techniques, the latter are introduced here beforehand. The following review will be based on the book by Cuevas and Scheer [1].

The time-evolution operator in the interaction picture as a perturbation expansion reads

$$\hat{S}_I(t,t_0) = \sum_{n=0}^{\infty} \frac{(-i)^n}{n!} \int_{t_0}^{t} dt_1 \int_{t_0}^{t} dt_2 \int_{t_0}^{t} dt_n \hat{T}[V_I(t_1)V_I(t_2)...V_I(t_n)] \tag{1.56}$$

where V_I is the perturbation transformed to the interaction picture, $\hat{T}$ is the time ordering operator and $\hat{S}_I$ is defined by $\Psi_I(t) = \hat{S}_I(t,t_0)\Psi_I(t_0)$. We assume that the perturbation can be switched on adiabatically from an unperturbed ground state by replacing $V \to Ve^{-\eta|t|}$ with an infinitesimal positive parameter η. In equilibrium, this means that the perturbation is zero for $t = \pm\infty$ and the ground state of the system, Ψ_G, is the starting point for the wave function and also recovered in the infinite future.

Defining the basic form of a many-body causal Green's function in second quantization, a discrete basis and the Heisenberg picture as

$$G^c_{\alpha\beta}(t,t') = \frac{\langle\Psi_H|\, \hat{T}\left[c_{\alpha\sigma}(t)c^{\dagger}_{\beta\sigma}(t')\right] |\Psi_H\rangle}{\langle\Psi_H|\Psi_H\rangle} \tag{1.57}$$

where the $c_{\alpha\sigma}$-operators are creation/annihilation operators for an electron at site α with spin σ, respectively. Transforming this equation into the interaction picture making use of the adiabatic switch-on mentioned above, one obtains

$$G_{\alpha\beta}(t,t') = \frac{\langle\Psi_G|\, \hat{S}_I(\infty,0)\hat{T}\left[\hat{S}_I(0,t)c^{(0)}_{\alpha\sigma}(t)\hat{S}_I(t,t')c^{(0)\dagger}_{\beta\sigma}(t')\hat{S}_I(t',0)\right] \hat{S}_I(0,-\infty)\,|\Psi_G\rangle}{\langle\Psi_G|\, \hat{S}_I(\infty,-\infty)\,|\Psi_G\rangle} \tag{1.58}$$

contracting the time evolution operators to $\hat{S}_I(\infty,-\infty)$ within the time-ordered product and inserting its expansion, the Green's function series looks like

$$G_{\alpha\beta}(t,t') = \frac{1}{\langle\Psi_G|\, \hat{S}_I(\infty,-\infty)\,|\Psi_G\rangle} \times \tag{1.59}$$

$$\left[\sum_{n=0}^{\infty} \frac{(-i)^n}{n!} \int_{-\infty}^{\infty} dt_1 ... \int_{-\infty}^{\infty} dt_n \,\langle\Psi_G|\, \hat{T}\left[c^{(0)}_{\alpha\sigma}(t)c^{(0)\dagger}_{\beta\sigma}(t')V^{(0)}(t_1)...V^{(0)}(t_n)\right] |\Psi_G\rangle\right] \tag{1.60}$$

The normalization factor makes sure that the phase acquired by the adiabatic switch-on is canceled out. The perturbation expansion can now be treated with the usual techniques, such as using Wick's theorem to set up a diagrammatic representation of the series. The self energy hereby becomes the sum of the irreducible, connected interaction graphs, and the full system Green's function can be written down in terms of the unperturbed Green's function by the many-body version of the Dyson equation, formally equivalent to Eq.1.48:

$$G^{r/a}(E) = \left[E\mathbb{1} - H - \Sigma^{r/a}(E) \mp i\eta\right]^{-1} \tag{1.61}$$

Thus, the solution of the perturbation problem means knowledge of the corresponding self-energy matrices.

Non-equilibrium

When moving the system out of equilibrium, the argumentation is analogous to the previous section. The major change lies in the fact that when assuming the adiabatic turn-on, the system does not longer reproduce the ground state for $t \longrightarrow +\infty$. This means that the usual time evolution operator can no longer be contracted to $\hat{S}_I(\infty, -\infty)$ as in the equilibrium case. The idea of the Keldysh formalism is now to redefine time by putting it onto the Keldysh contour which, after moving from $t = -\infty$ to $t = +\infty$, returns back to $t = -\infty$ to recover the ground state. This way, the equilibrium formalism can be adapted with few changes to also be valid in the non-equilibrium case. Time-ordering operators $\hat{T}_c$ now rearrange operators onto the contour instead of real time, and time evolution $\hat{S}_c$ also takes place on the contour. After the necessary calculations have been carried out, it is possible to return to normal time by applying the Langreth rules [50] of analytical continuation.

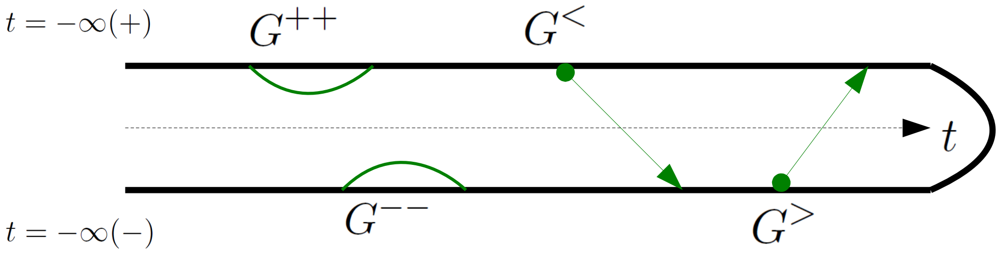

Figure 1.2: The Keldysh contour. The imaginary time starts at $-\infty$, proceeds to $+\infty$ and back to $-\infty$. The Green's functions connecting same and different branches are visualized.

In complete analogy, the causal Green's function is

$$G^{c}_{\alpha\beta}(t_a, t'_b) = -i \frac{\langle \Psi_H | \hat{T}_c \left[c_{\alpha\sigma}(t_a) c^{\dagger}_{\beta\sigma}(t'_b) \right] | \Psi_H \rangle}{\langle \Psi_H | \Psi_H \rangle} \tag{1.62}$$

where the dominator evaluates to $\langle \Psi_H | \Psi_H \rangle = 1$ in this case. This leads to four different combinations on which of the branches (- and +) the time arguments t and t' can be located:

$$\begin{aligned}
G^{++}_{\alpha\beta}(t, t') &= -i \langle \Psi_H | \hat{T}_c \left[c_{\alpha\sigma}(t_+) c^{\dagger}_{\beta\sigma}(t'_+) \right] | \Psi_H \rangle && (1.63) \\
G^{<}_{\alpha\beta}(t, t') &= +i \langle \Psi_H | c_{\beta\sigma}(t'_+) c^{\dagger}_{\alpha\sigma}(t_-) | \Psi_H \rangle && (1.64) \\
G^{>}_{\alpha\beta}(t, t') &= -i \langle \Psi_H | c_{\alpha\sigma}(t_+) c^{\dagger}_{\beta\sigma}(t'_-) | \Psi_H \rangle && (1.65) \\
G^{--}_{\alpha\beta}(t, t') &= -i \langle \Psi_H | \hat{T}_c \left[c_{\alpha\sigma}(t_-) c^{\dagger}_{\beta\sigma}(t'_-) \right] | \Psi_H \rangle && (1.66) \\
& && (1.67)
\end{aligned}$$

with a similar distinction for the self-energies. $G^{>}_{\alpha\beta}$ and $G^{<}_{\alpha\beta}$ are called greater and lesser Green's functions, respectively. The lesser Green's function is connected to its unperturbed counterpart $g^{<}_{\alpha\beta}(E)$ by

$$G^{<}(E) = [\mathbb{1} + G^{r}(E)\Sigma^{r}(E)] g^{<}(E) [\mathbb{1} + \Sigma^{a}(E) G^{a}(E)] - [G^{r}(E)\Sigma^{<}(E)G^{a}(E)] \tag{1.68}$$

As mentioned, it is possible to re-derive the atomistic Landauer formula in the above framework. But now, it can be extended to interacting and time-dependent systems. The challenge is usually to find the self-energy; in the case that it is determined by a non-interacting device region coupled to leads, the calculation is formally equivalent to the self-energy found in Eq. [1.51]. With the formalism introduced, it will now be shown how to derive the equation of motion technique implemented in tranDFTB.

1.2.3. Reduced density matrix propagation

We use a time-resolved transport approach based upon the equation of motion for the reduced (device) density matrix (RDM) of the system. With the help of the Keldysh formalism, Chen et al. derived a closed equation for the RDM by finding an expression for the dissipation terms appearing due to the partitioning of the system. Being closely related to the standard DFT-NEGF approaches for static transport, the method can be readily combined with DFT, as was implemented by the original authors into a package called LODESTAR [51]. Since time-resolved calculations for molecular junctions are very demanding with respect to computational time, it was sensible to also use a DFTB-Hamiltonian instead, as realized in our program tranDFTB. The initial conversion was done mainly by Yang Wong, a former member of our group. Later, Björn Korff was a tremendous help with maintenance and bugfixes to put the code into its current working state.

As explained in Chen's paper to their approach [52], the main quantity in the formalism is the reduced single-electron density matrix σ which is propagated in the time domain. In real space representation written in atomic orbital basis ϕ_ν, it is defined as

$$\sigma_{\mu\nu}(t) = \int d\mathbf{r} \int d\mathbf{r}' \phi^*_\mu(\mathbf{r}') \underbrace{\sum_p^{\text{occ}} \psi^*_p(\mathbf{r}' t) \psi_p(\mathbf{r}, t)}_{\sigma(\mathbf{r},\mathbf{r}',t)} \phi_\nu(\mathbf{r}) \tag{1.69}$$

where ψ_p is the p-th occupied molecular orbital. We start from the Liouville-van Neumann equation

$$i \frac{\partial}{\partial t} \sigma(t) = [H(t), \sigma(t)] \tag{1.70}$$

The system is now partitioned into Leads L,R (Left and Right) and device region D, which also contains several layers of contact material. With this choice, the Hamiltonian and the reduced density matrix also split up into a block format.

$$\sigma = \begin{pmatrix} \sigma_L & \sigma_{LD} & 0 \\ \sigma_{DL} & \sigma_D & \sigma_{DR} \\ 0 & \sigma_{RD} & \sigma_R \end{pmatrix}, \qquad H = \begin{pmatrix} H_L & T_{LD} & 0 \\ T_{DL} & H_D & T_{DR} \\ 0 & T_{RD} & H_R \end{pmatrix} \tag{1.71}$$

The interactions between the leads, $T_{RL,LR}$ and $\sigma_{RL,LR}$ are assumed to vanish. If one writes down a equation of motion for the device part of the reduced density matrix only, furthermore assuming an orthonormal basis set for simplicity, it looks like [52]

$$i\dot{\sigma}_D = [H_D, \sigma_D] + \sum_{\alpha=L,R} (T_{D\alpha}\sigma_{\alpha D} - \sigma_{D\alpha} T_{\alpha D}) \tag{1.72}$$

$$= [H_D, \sigma_D] - i \sum_{\alpha,\beta} Q_\alpha \tag{1.73}$$

Thus, the Q_α contain all the information about the coupling between device and leads and are called dissipation terms. If the leads are not connected, they both vanish.

In order to prove a closed equation exists, one needs the so-called *holographic electron density theorem* which states that the electron density of an arbitrary nonzero subsystem uniquely determines the electron density of the whole system, a consequence of the density being real and analytical. For the time-independent case, this has been proven by Riess and Münch [53] and then extended to the time-dependent case by Chen et al. [52], who proved the real analyticity in space and time. Consequently, the density of a subsystem determines all excited state properties of the whole system, implying that all quantities are explicit or implicit functionals of the electronic density. The dissipation Q_α is no exception and consequently, $Q_\alpha = Q_\alpha[\rho_D]$ if the subsystem is chosen to be the device region. The equation of motion is now formally closed and constitutes the core of the approach:

$$i\dot{\sigma}_D = [H_D[\rho_D], \sigma_D] - i\sum_{\alpha,\beta} Q_\alpha[\rho_D] \tag{1.74}$$

Writing the quantities in an atomic basis and with single-electron states k_α of lead α,

$$i\dot{\sigma}_{\mu\nu} = \sum_{\xi\in D}(H_{\mu\xi}\sigma_{\xi\nu} - \sigma_{\mu\xi}H_{\xi\nu}) - i\sum_{\alpha=L,R} Q_{\alpha,\mu\nu} \tag{1.75}$$

$$Q_{\alpha,\mu\nu} = i\sum_{k_\alpha\in\alpha}(T_{\mu k_\alpha}\sigma_{k_\alpha\nu} - \sigma_{\mu k_\alpha}T_{k_\alpha\nu}) \tag{1.76}$$

the transient current through the L,R-interfaces can conveniently be calculated from the dissipation terms.

$$I_\alpha(t) = -\int_\alpha d\mathbf{r}\frac{\partial}{\partial t}\rho(\mathbf{r}, t) = -\sum_{l\in D} Q_{\alpha,\xi\xi} = -\mathbf{Tr}[Q_\alpha(t)] \tag{1.77}$$

In order to relate Q_α to quantities one can calculate, we first write down the Dyson equation for $G_{k_\alpha\nu}(t,t')$ as described in the appendix A of [52].

$$G_{k_\alpha\nu}(t,t') = \sum_{\xi\in D}\int_C d\tau g_{k_\alpha}(t,\tau)T_{k_\alpha\xi}(\tau)G_{\xi\nu}(\tau,t') \tag{1.78}$$

In order to convert this contour integral in Keldysh space into a real time integral, we have to employ a continuation rule which is derived from the

Langreth theorem [50]. The rule for our case reads:

$$D(t,t') = \int_C d\tau A(t,\tau)B(\tau,t') \rightarrow D^< = \int_{t=-\infty}^{t=\infty} (A^r B^< + A^< B^a) dt \tag{1.79}$$

Using it for the above Dyson equation, one obtains

$$\begin{aligned} G^<_{\nu k_\alpha}(t',t) &= -[G^>_{k_\alpha \nu}(t,t')]^* && (1.80) \\ &= \sum_{\xi \in D} \int_{-\infty}^{\infty} d\tau T_{\xi k_\alpha}(\tau) \cdot [g^<_{k_\alpha}(\tau,t) G^r_{\nu\xi}(t',\tau) + g^a_{k_\alpha}(\tau,t) G^<_{\nu\xi}(t',\tau)] && (1.81) \end{aligned}$$

Together with the following general relation between density matrix and lesser Green's function in the Keldysh formalism, where $t^+ = t + dt$:

$$\sigma_{\nu k_\alpha}(t) = -i G^<_{\nu k_\alpha}(t,t')|_{t'=t^+} \tag{1.82}$$

as well as the usual definition of the self-energies

$$\Sigma^a_{\alpha,\xi\mu}(t,\tau) = \sum_{k_\alpha \in \alpha} T_{\xi k_\alpha}(t) g^a_{k_\alpha}(t,\tau) T_{k_\alpha \mu}(\tau) \tag{1.83}$$

one obtains, after insertion into the EOM, an expression for the dissipation terms in the atomic basis [52]:

$$Q_{\alpha,\mu\nu}(t) = -\sum_{\xi \in D} \int_{-\infty}^{\infty} d\tau [G^<_{\mu\xi}(t,\tau)\Sigma^a_{\alpha,\xi\nu}(\tau,t) + G^r_{\mu\xi}(t,\tau)\Sigma^<_{\alpha,\xi\nu}(\tau,t) + h.c.] \tag{1.84}$$

Note that a prerequisite for this result derived with the Keldysh formalism is that the initial state of the propagation $\Psi(t_0)$ can be reached from the ground state of the isolated system Ψ_G by adiabatically switching on the couplings. If this is given, the result is exact, in other (rare) cases, it is only an approximation to the partition-free scheme [54], as pointed out and derived in the appendix of [52].

The Green's functions one has to calculate are connected to the respective self energies through the following equations of motion.

$$i\frac{\partial G^r_{\mu\nu}(t,\tau)}{\partial t} = \delta(t-\tau)\delta_{\mu\nu} + \sum_{\xi\in D} H_{\mu\xi}(t) G^r_{\xi\nu}(t,\tau) \tag{1.85}$$

$$+ \sum_{\xi\in D} \int_{-\infty}^{\infty} dt' \Sigma^r_{\mu\xi}(t,t') G^r_{\xi\nu}(t',\tau) \tag{1.86}$$

$$i\frac{\partial G^<_{\mu\nu}(t,\tau)}{\partial t} = \sum_{\xi\in D} \int_{-\infty}^{\infty} dt' [\Sigma^<_{\mu\xi}(t,t') G^a_{\xi\nu}(t',\tau) + \Sigma^r_{\mu\xi}(t,t') G^<_{\xi\nu}(t',\tau)] \tag{1.87}$$

$$+ \sum_{\xi\in D} H_{\mu\xi}(t) G^<_{\xi\nu}(t,\tau) \tag{1.88}$$

As in the time-independent case, the self-energies play the most important role for the transport properties. The first approximation one has to make in any case is extrapolating the device part electron density ρ_D onto the one in the leads ρ_α, which is possible according to the mentioned holographic electronic density theorem. This continuation implies that the lead electron density is a functional of the device electron density,

$$\rho_\alpha(\mathbf{r},t) = \rho_\alpha^{CT}[\mathbf{r},t;\rho_D(\mathbf{r},t)] \tag{1.89}$$

and thus it follows that the sought-after self energies are also explicit and implicit functionals of the device electron density.

$$\Sigma_\alpha^{<,a}(\tau,t) = \Sigma_\alpha^{<,a}[\tau,t;\rho_D,\rho_\alpha^{CT}[\rho_D]] \tag{1.90}$$

The device region therefore has to include a sufficient number of lead material layers to ensure a proper extrapolation of this kind.

Wide-band limit (WBL) approximation

Solving the problem at hand within the WBL [55] is in principle not necessary, but considerably speeds up the calculation while being a very good approximation for simple metal contacts with a smooth DOS and couplings at comparatively low bias. The self-energy is first split up into two real symmetric matrices which are a sum of left and right lead part, respectively - one hermitian level shift Λ_α and one anti-hermitian linewidth Γ_α,

$$\Sigma_\alpha^{r,a}(t,t') = (\Lambda_\alpha \mp i\Gamma_\alpha)\delta(t-t') \tag{1.91}$$

which are also related by the Kramers-Kronig relation [56]. The linewidths Γ_α are assumed to be energy-independent, resulting in the requirement for lead

DOS and device-lead coupling to be slowly varying in energy. Furthermore, the level shifts are approximated to be constant for all energy levels [52]. The lesser self-energies can now be written as [57]

$$\Sigma^{<}_{\alpha,nm}(t,t') = \frac{2i}{\pi}\Gamma_{\alpha} exp\left\{i\int_{t'}^{t} d\tau V_{\alpha}(\tau)\right\}\int_{-\infty}^{\infty} d\epsilon f^{\alpha}(\epsilon)e^{-i\epsilon(t-t')} \tag{1.92}$$

which also implies that the approximated self-energies Σ_{α} only depend on a fixed energy at which they are chosen to be evaluated. Usually, this is the Fermi energy of the combined system without bias. In the above equation, f^{α} is the Fermi distribution function of contact α. The wide-band dissipation term is now determined by the device Hamiltonian, the device reduced density matrix, and the self-energies containing the effect of the leads.

$$Q^{WBL}_{\alpha}(t) = K^{\alpha}(t) + i[\Lambda_{\alpha}, \sigma(t)] + \{\Gamma_{\alpha}, \sigma(t)\} \tag{1.93}$$

with the following abbreviations.

$$\begin{aligned} K_{\alpha}(t) &= -\frac{2i}{\pi}U_{\alpha}(t)\int_{-\infty}^{\mu_0}\frac{d\epsilon e^{i\epsilon t}}{\epsilon\mathbb{1} - H_D(0) - \Sigma^r}\Gamma_{\alpha} && (1.94)\\ &= -\frac{2i}{\pi}\int_{-\infty}^{\mu_0}[\mathbb{1} - U_{\alpha}(t)e^{i\epsilon t}]\frac{d\epsilon}{[\epsilon - V_{\alpha}(t)]\mathbb{1} - H(t) - \Sigma^r}\Gamma_{\alpha} + h.c. && (1.95) \end{aligned}$$

$$U_{\alpha}(t) = exp\left\{-i\int_{0}^{t}[H(\tau) + \Sigma^r - \mathbb{1}V_{\alpha}(\tau)]d\tau\right\} \tag{1.96}$$

Here, $V_{\alpha}(t)$ is the bias potential inducing a rigid shift at lead α.

Chapter 2

Implementation

In order to use DFTB in the time-dependent non-equilibrium context, one has to make some adaptions since the total energy of the system is no longer defined and there is no justification to use a ground state theory on time-dependent problems. As DFT has been generalized to dynamical problems in order to calculate excitation energies, frequency-dependent response properties or photoabsorption spectra, also DFTB was extended to TD-DFTB [11, 12, 13]. Additional modifications are needed to treat a system with open boundary conditions which are very similar to the ones frequently applied in time-independent DFT-NEGF transport calculations. As the boundary conditions of the device region potential are set by the applied bias in non-equilibrium situations, the Poisson equation has to be solved to obtain the potential profile from the charge density. The code is divided into three separate steps: the calculation of the Hamiltonian and the self-energy of the ground state using DFTB, the calculation of the initial density matrix for the propagation and the time-dependent evaluation itself. The latter two are combined into one subsection here.

2.1. Ground state calculation

The Hamiltonian is built using the DFTB method described above and therefore needs, apart from the system geometry, precalculated lookup-tables which will be called Slater-Koster-files (SK-files). They constitute input and have to be pre-calculated beforehand, in our case using the PBE functional. During this work, we use files describing the organic compounds with the elements hydrogen, carbon, sulfur and oxygen, in conjunction with the metals aluminum, copper and gold.

Since the interactions between the valence orbitals vanish after a certain cut-off, the Hamiltonian can be separated into a block structure.

$$H = \begin{pmatrix} \ddots & \ddots & & & & & & & \\ \ddots & H_L & T_{LL} & 0 & 0 & 0 & 0 & 0 & \\ & T_{LL}^\dagger & H_L & T_{LL} & 0 & 0 & 0 & 0 & \\ & 0 & T_{LL}^\dagger & H_L & T_{LD} & 0 & 0 & 0 & \\ & 0 & 0 & T_{LD}^\dagger & H_D & T_{DR} & 0 & 0 & \\ & 0 & 0 & 0 & T_{DR}^\dagger & H_R & T_{RR} & 0 & \\ & 0 & 0 & 0 & 0 & T_{RR}^\dagger & H_R & T_{RR} & \\ & 0 & 0 & 0 & 0 & 0 & T_{RR}^\dagger & H_R & \ddots \\ & & & & & & & \ddots & \ddots \end{pmatrix} \tag{2.1}$$

The repeating blocks in the leads are also called principal layers (PL) with Hamiltonians H_L and H_R. Together with the device Hamiltonian H_D and the couplings $T_{\alpha\beta}$ between the respective blocks, the system is fully described. The leads are treated as semi-infinite in a periodic calculation and therefore, their Hamiltonians have to be truncated. In tranDFTB, four principal layers are used to calculate the finite surface Green's function from which the self-energies may later be deducted. In its current version, the code forces the user to include one principal layer on each side of the device region which has to have translation symmetry with a fourth of one lead. This way, a smooth transition of the potential from the device to the leads is made sure and the coupling matrix from leads to device is identical to the one within the leads, which means that the self-energy can be calculated only from information given by the leads. The device region is not treated periodically in transport direction and consequently, the device charges are not calculated self-consistently in the ground state calculation since this would result in unphysical charging at the boundaries due to the leads not being coupled yet.

The device Hamiltonian in turn consists of one principal layer of lead material each, coupled by T_{LL} and T_{RR} to the main leads, and the Hamiltonian of the inner device region H_{ID} (usually a molecule) which is in turn coupled to the principal layers by T_{LD} and T_{RD}.

$$H_D = \begin{pmatrix} H_L & T_{LD} & 0 \\ T_{LD}^\dagger & H_{ID} & T_{DR} \\ 0 & T_{DR}^\dagger & H_R \end{pmatrix} \tag{2.2}$$

A coupling between the leads directly is not possible in our formulation.

In summary, the device region uses non-SCC-DFTB with periodic boundary conditions perpendicular to the transport direction, whereas the leads are treated at SCC-DFTB-level periodically in every direction. Since self-consistent charges are calculated for the leads, one also needs the $\gamma_{\alpha\beta}$-term of Eq. [1.27]. Its on-site value is determined by the Hubbard parameters U_α, which already include some correlation due to their DFT origin [58] and are also found in the Slater-Koster-files ($\gamma_{\alpha\alpha} = U_\alpha$). The long range behavior should be $\frac{1}{|\mathbf{R}_\alpha - \mathbf{R}_\beta|}$ and one needs an interpolation formula [37] between these two extrema. The interpolation depends on the density fluctuations $\delta\rho$ which, after employing the DFTB monopole approximation, look like

$$\delta\rho_\alpha(\mathbf{r}) = \frac{\Delta q_\alpha \tau_\alpha^3}{8\pi} e^{-\tau_\alpha|\mathbf{r}-\mathbf{R}_\alpha|} \tag{2.3}$$

subjected to the constraint

$$\int d\mathbf{r}\delta\rho_\alpha(\mathbf{r}) = \Delta q_\alpha \tag{2.4}$$

where one can see from $\gamma_{\alpha\alpha} = U_\alpha$ that

$$\tau_\alpha = \frac{16}{5} U_\alpha \tag{2.5}$$

In the code, $\gamma_{\alpha\beta}$ is divided into an Ewald sum consisting of a long-range and short-range part according to

$$\gamma(\tau_a, \tau_b, R) = \frac{1}{R} - \Xi(\tau_a, \tau_b, R) \tag{2.6}$$

of which the long-ranged decay is calculated in Fourier space and the short-ranged term $\Xi(\tau_a, \tau_b, R)$ in real space. As soon as the γ-matrix has been calculated and the initial unshifted Hamiltonian H and overlap matrices S have been constructed in block structure, the self-consistent charge cycle begins, starting with $\Delta q_\alpha = 0$. Optional k-points set by the user are distributed linearly over k-space. However, each of the calculations below were made at the Gamma point for numerical efficiency. In each cycle, the γ-matrix and the calculated Mulliken charge differences are used to shift the Hamiltonian (see Eq. 2.15 below). It is then diagonalized and its energy levels filled with electrons according to the Fermi function at temperature $\Theta \approx 0$K. Degenerate energy levels at the Fermi energy receive partial electrons. From the occupation numbers, the density matrix is constructed, which is then used to calculate the new

Mulliken charges and the total DFTB energy. The convergence towards the energy minimum is accelerated by a Broyden mixer [59] up to a set convergence criterion. As soon as the final SCC-shifted Hamiltonian for the leads is found together with the corresponding Fermi energy, the self-energies can be calculated in the next step.

2.2. Initial density matrix and time propagation

The following description is largely identical to the time-independent case of static transport first described for DFTB in [60]. Starting from the results of the previous section, the system Fermi energy is set as the arithmetic average of the lead Fermi energies. It is possible to manually shift them by an input parameter if one wants to evaluate the WBL self energies at a different energy than E_F.

To arrive at the self-energies, we first have to calculate the surface Green's functions g_α^s due to

$$\Sigma_\alpha^r(E_F) = (T_{\alpha D})^\dagger g_\alpha^s(E_F) T_{\alpha D} \tag{2.7}$$

As mentioned, each of the contacts is periodically semi-infinite and built out of four principle layers which only interact with their respective nearest layer. In a restatement of the standard renormalization technique [61], the recursive set of equations to be solved is given as:

$$g_\alpha^s(E) = (E\mathbb{1} - \xi_\infty^{-1}) \tag{2.8}$$

$$\begin{aligned}
\xi_{i+1} &= \xi_i + a_i(E\mathbb{1} - \eta_i)^{-1} b_i \\
\eta_{i+1} &= \eta_i + a_i(E\mathbb{1} - \eta_i)^{-1} b_i + b_i(E\mathbb{1} - \eta_i)^{-1} a_i \\
a_{i+1} &= a_i(E\mathbb{1} - \eta_i)^{-1} a_i \\
b_{i+1} &= b_i(E\mathbb{1} - \eta_i)^{-1} b_i \\
\xi_0 = H_\alpha, \eta_{\alpha,0} &= H_\alpha, a_0 = T_\alpha, b_0 = T_\alpha^\dagger
\end{aligned}$$

The initial values are obtained by a standard SCC-DFTB calculation applying periodic boundary conditions as described in the previous section. Using these unperturbed Green's functions of the contacts, one can then construct the self-energy matrices.

It is now time to also treat the device region at SCC level. The device Green's function of the coupled system

$$G_D^r(E) = [E\mathbb{1} - H_D(t = 0) - \Sigma(E)]^{-1} \tag{2.9}$$

can be used to calculate the initial device density matrix according to equilibrium Green's function theory before any bias is applied:

$$\sigma_D(t = 0) = \int_{-\infty}^{\infty} dE \frac{1}{2\pi} f(E) \mathrm{Im}\{G_D^r(E)\} \tag{2.10}$$

The integration of the Green's function can be treated analytically in the WBL, but general difficulties arise regarding the lower integration boundary which will be discussed in the next section. The Mulliken charges can now be obtained from

$$q_\alpha = \mathbf{Tr}_\alpha[\sigma_D S_D] \tag{2.11}$$

where $\mathbf{Tr}_\alpha$ is the trace over all atomic orbitals at site α. The charges yield the electronic density via Eq. 2.3 and the potential by solving the Poisson equation (at $V = 0$) for the potential δV_H induced by the difference density $\delta\rho$

$$\nabla^2 \delta V_H(\mathbf{r}) = -4\pi\delta\rho(\mathbf{r}) \tag{2.12}$$

on a real space grid forming a box which is enclosing the device region. The resulting potential is then projected onto the atomic sites by

$$\delta V_\alpha = \frac{\int_{box} d\mathbf{r} \delta V_H(\mathbf{r}) e^{-\frac{16}{5} U_\alpha |\mathbf{r} - \mathbf{R}_\alpha|}}{\int_{box} d\mathbf{r} e^{-\frac{16}{5} U_\alpha |\mathbf{r} - \mathbf{R}_\alpha|}} \tag{2.13}$$

which is then used to calculate the SCC addition to the zeroth-order DFTB Hamiltonian $H^0_{\mu\nu}[\rho_0]$ as

$$H_{\mu\nu} = H^0_{\mu\nu}[\rho_0] + \delta V_{\mu\nu}[\{\Delta q\}] \tag{2.14}$$

$$\delta V_{\mu\nu} = \frac{1}{2}(\delta V_\alpha + \delta V_\beta) S_{\mu\nu} \qquad \mu \in \alpha, \nu \in \beta \tag{2.15}$$

This leads to a self-consistent cycle which concludes with the density matrix that is used as a starting point for the time dependent propagation.

Using the initial density matrix and the self-energies, the dissipation terms Q_α can now be calculated from Eq. 1.93 in conjunction with Eq. 1.94. The density matrix is then propagated in time by the Runge-Kutta method, typically in fourth order (second and sixth order RK is also implemented). When the new density matrix at $\sigma_D(t + \Delta t)$ with chosen time step Δt has been constructed, the Poisson equation is solved again to update the DFTB Hamiltonian, which in turn yields the ingredients necessary for the next step in the propagation. At each time t, the current is calculated from

$$I_\alpha(t) = -\mathbf{Tr}[Q_\alpha(t)] \tag{2.16}$$

The history of the propagation is contained in the K-term of Eq. 1.94 through the propagator $U(t)$, the Hamiltonian itself is local in time and thus the exchange and correlation are treated adiabatically.

2.3. Test calculations and examples

2.3.1. Typical parameters, voltage profiles and systems

A model structure frequently encountered in this work is 1,4-benzenediol coupled to aluminum leads, see Fig. 2.1. The geometry of the hydrogen-passivated benzenediol-molecule had previously been optimized using DFTB and then symmetrically placed between the leads without further optimization. Generally, we do not account for changes of the geometry due to the time-dependent bias, since the corresponding mechanics are still unknown and should not play a major role for the qualitative information we are interested in. For the aluminum, the experimental bulk lattice constant of 4.05 Å [62] was used. In the same way, systems were constructed with the central molecule being alkanes and alkenes and used in this work.

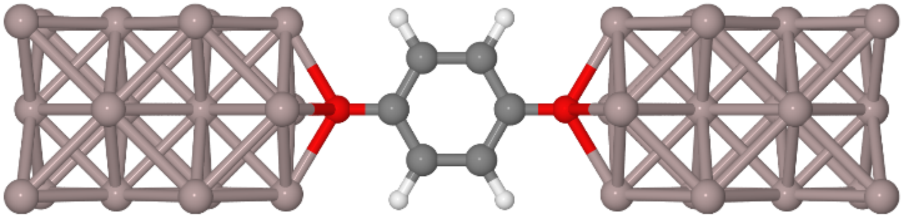

Figure 2.1: The device region of the Al-1,4-benzenediol-Al test system consisting of 48 atoms, in addition to the 144 atoms of the leads.

The transmission of our test system is small at the Fermi energy ($T(E_F) \approx 0.024$) and transport is carried by the π-orbitals of the conjugated structure. Throughout our projects, hydrogen atoms are described with their s-orbital whereas carbon, oxygen and aluminum are described with s- and p-orbitals. The calculations using gold additionally include its d-orbitals.

All calculations presented are converged with respect to the time step (typically Δt = 3-5 attoseconds). A small enough step size is crucial for the time propagation to be numerically sound and physically correct. The total evolution time varies depending on the goal of the calculation and is usually in the range of 30-50 fs for a total of roughly 10000 individual time steps. The input voltage profile is completely arbitrary and the amplitudes of the voltages used can go beyond linear response. However, very steep jumps should be avoided for numerical reasons. Fig. 2.2 shows common choices.

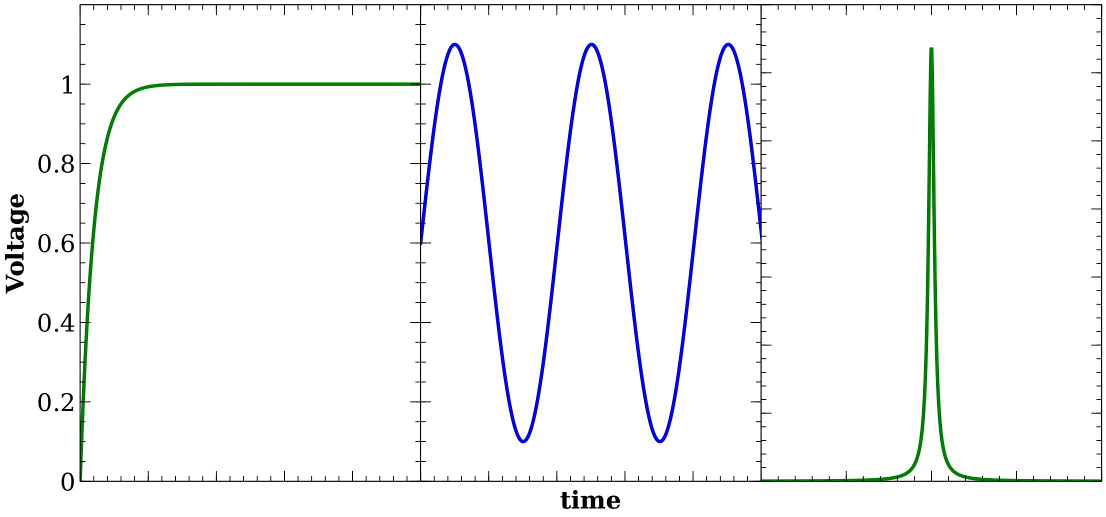

Figure 2.2: Typical input voltage profiles for tranDFTB used in this work: exponentially damped, sinusoidal and Lorentz shape.

Using the exponential voltage profile $V = V_0(1 - e^{-\frac{t}{t_0}})$ as depicted in Fig. 2.2 with different time constants, one can see in Fig. 2.3 that the initial turn-on increase of the voltage influences the transient current before a steady state is reached, but not the steady state itself [20]. Note that we always plot the current through only one of the interfaces (i.e. the left side), as the dc steady state is equal for both interfaces. Due to charging of the system, the currents at the two interfaces may be different under ac bias (see following chapters) and in transient times [63].

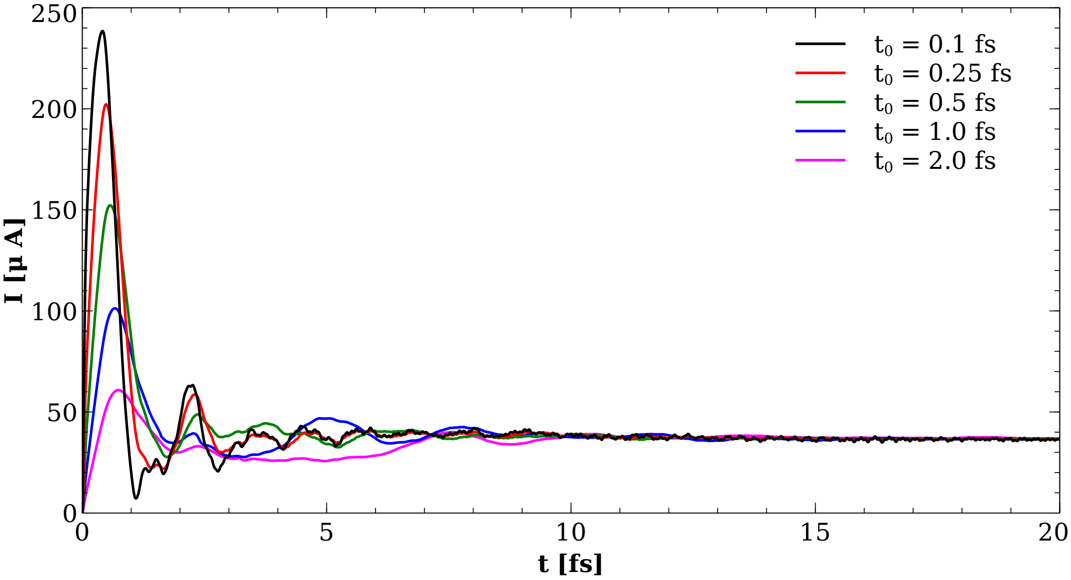

Figure 2.3: The influence of various time constants for the initial exponential damping on transients and the steady state. $V_0 = 3.5$V, Al-1,4-benzenediol-Al.

In the limit $I_{\infty}^{TD} = \lim_{t\to\infty} I(t)$, it is interesting to see if the steady state recovers the Landauer result (see also Ref. [64]), which doubles as a good test to verify the time propagation. In Fig. 2.4 you can see that for the whole voltage range of interest, the time-dependent steady state for $t \to \infty$ coincides almost exactly with the steady state obtained from a standard Landauer calculation. In both cases, the same Hamiltonian in the wide band limit was used, and the time-dependent current had to be averaged over the last 2 of 20 fs due to small oscillations still being present. As a byproduct, it can be concluded that for local functionals, the time-dependent propagation does not contain additional information when looking for steady state properties [63]. As discussed in Ref. [64] multiple or no steady states may exist in model systems, but weren't observed in the systems used within this work. However, sizeable differences between the standard Landauer NEGF current and the TD current are expected for non-local functionals even in the linear response regime.

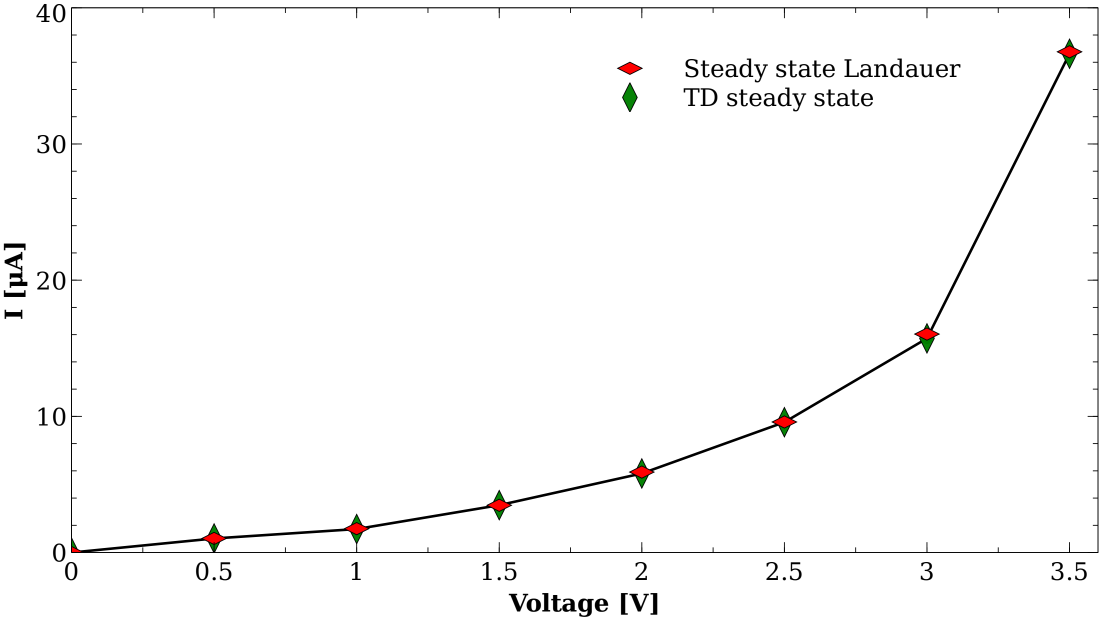

Figure 2.4: Comparison of time-independent Landauer steady state calculations using tranDFTB and the steady states that are reached by the time-dependent propagation.

2.3.2. The outer density matrix blocks in the WBL

The following is a discussion of a problem arising for the integration of the Green's function in the WBL, mentioned in the context of Eq. 2.10 found in the previous section. As mentioned, tranDFTB calculates the Mulliken charges from the device density matrix and the overlap according to

$$q_\alpha = \sum_{\mu\in\alpha}\sum_{\nu}(\sigma_D)_{\mu\nu}(S_D)_{\nu\mu} \tag{2.17}$$

with i denoting the orbital index of atom A and j the orbital index of the remaining system. In order to evaluate this product, one also needs blocks in the density matrix coupling the device to the leads, since

$$\sigma\cdot S = \begin{pmatrix} \sigma_L & \sigma_{LD} & 0 \\ \sigma_{LD}^\dagger & \sigma_D & \sigma_{DR} \\ 0 & \sigma_{DR}^\dagger & \sigma_R \end{pmatrix}\cdot\begin{pmatrix} S_L & S_{LD} & 0 \\ S_{LD}^\dagger & S_D & S_{DR} \\ 0 & S_{DR}^\dagger & S_R \end{pmatrix} \tag{2.18}$$

leads to

$$q_\alpha = \sum_{\mu\in\alpha}\left(\sum_\nu (\sigma_D)_{\mu\nu}(S_D)_{\nu\mu} + \sum_\nu (\sigma_{DL})_{\mu\nu}(S_{LD})_{\nu\mu} + \sum_\nu (\sigma_{DR})_{\mu\nu}(S_{RD})_{\nu\mu}\right) \tag{2.19}$$

for the atoms within the device region. The outer density matrix blocks σ_{DL} and σ_{DR} can be calculated from the full system Green's function in which the description of lead α is already replaced by the surface Green's function g^s_α

$$G^r_{full} = \begin{pmatrix} (g^s_L)^{-1} & T_{LD} & 0 \\ T_{DL} & ES_D - H_D & T_{DR} \\ 0 & T_{RD} & (g^s_R)^{-1} \end{pmatrix}^{-1} \tag{2.20}$$

Recursive blockwise matrix inversion yields

$$G^r_{full} = \begin{pmatrix} g^s_L + g^s_L T_{LD} G^r T_{DL} g^s_L & -g^s_L T_{LD} G^r & g^s_L T_{LD} G^r T_{DR} g^s_R \\ -G^r T_{DL} g^s_L & G^r & -G^r T_{DR} g^s_R \\ g^s_R T_{RD} G^r T_{DL} g^s_L & -g^s_R T_{RD} G^r & g^s_R + g^s_R T_{RD} G^r T_{DR} g^s_R \end{pmatrix} \tag{2.21}$$

with the device Green's function

$$G^r = [ES_D - H_D - \Sigma]^{-1} = [ES_D - H_D - T_{DL} g^s_L T_{LD} - T_{DR} g^s_R T_{RD}]^{-1} \tag{2.22}$$

In equilibrium, the density matrix is calculated from

$$\sigma = \frac{i}{\pi}\int \mathrm{d}E\, f(E)\,[G^r(E) - G^a(E)] = -\frac{2}{\pi}\mathrm{Im}\left(\int \mathrm{d}E\, f(E) G^r(E)\right) \tag{2.23}$$

the outer blocks can readily be identified as

$$\sigma_{DL} = \frac{2}{\pi}\mathrm{Im}\left(\int \mathrm{d}E\, f(E) G^r T_{DL} g^s_L\right) \tag{2.24}$$

$$\sigma_{DR} = \frac{2}{\pi}\mathrm{Im}\left(\int \mathrm{d}E\, f(E) G^r T_{DR} g^s_R\right) \tag{2.25}$$

The issue now arises when employing the wide band limit, as the surface Green's function and the coupling terms to the leads become independent of energy:

$$\sigma_{DL}^{WBL} = \frac{2}{\pi}\mathrm{Im}\left\{\left(\int_{E_B}^{E_F} \mathrm{d}E\ G^r\right) T_{DL} g_L^s\right\} \tag{2.26}$$

$$q_\alpha^{WBL} = -\sum_{\mu\in\alpha}\sum_{\nu}\frac{2}{\pi}\mathrm{Im}\left\{\left(\int_{E_B}^{E_F} \mathrm{d}E\ G^r\right)_{\mu\nu} (S_D - T_{DL} g_L^s S_{LD} - T_{DR} g_R^s S_{RD})_{\nu\mu}\right\} \tag{2.27}$$

The integral is now only carried out over G^r and no longer converges if the lower integration boundary is set to be $E_B \rightarrow -\infty$ as without the wide band limit, since the Green's function decays as $\frac{1}{E}$ below the lowest states of the system. Therefore, if the outer blocks are to be included in the calculation, one has to specify an artificial lower integration boundary for the above integral. On the other hand, omitting the outer blocks leads to unphysical charge buildups at the interface between device region and leads, as was first observed in a carbon chain, see Fig. 2.5

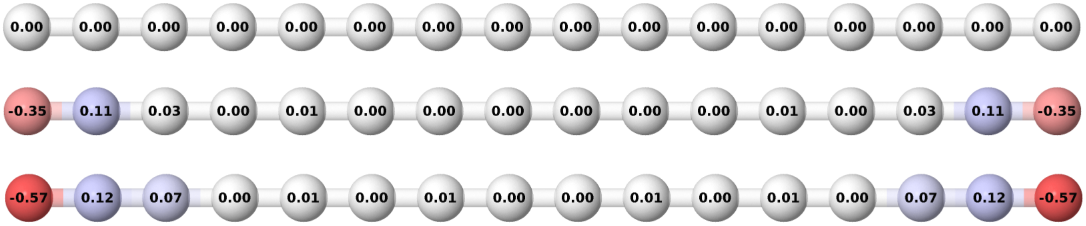

Figure 2.5: Effect of the outer density matrix blocks on a carbon chain in equilibrium. **Top**: non-WBL with outer blocks. **Center**: non-WBL without outer blocks. **Bottom**: WBL without outer blocks.

Intuitively, there should be no partial charges in a homogeneous carbon chain. Omitting the outer blocks leads to a charging of the atoms near the interface in addition to the charge error introduced by the wide band limit itself. The polarity of the additional charging depends on the atoms in question and may also lead to error correction in other systems. Since tranDFTB is tailored towards numerical efficiency, the WBL is crucial for the time-dependent part, and consistency demands that the WBL and the same choice for E_B are also used for the initial density matrix of the propagation calculated in the time-independent part of the code.

We explored various options how to specify the lower integration boundary. Dynamical approaches include setting it as the lowest energy of the surface density of states in the leads or choosing it in a way that the total difference charge of the whole system to the non-WBL result is close to zero. Our investigations showed that the time-dependent current was almost entirely independent of the charges at the boundary and the choice of E_B. For our usual test system Al-1,4-benzenediol-Al and other junctions with metallic leads, omitting the outer blocks led to considerable error correction with the wide band limit (see Fig. 2.6) and to charge distributions very close to the non-WBL including outer blocks.

This fact combined with the unwanted arbitrariness of the lower integration boundary led us to omitting the outer blocks in our test calculations below. However, one has to keep in mind that the error in the charge distribution might lead to effects in other quantities than the current and thus the influence of the outer blocks should always be checked. Especially when calculating the response to alternating currents, the charge distribution is crucial. We will therefore investigate the changes introduced by the outer blocks in the next chapter about dynamic admittance.

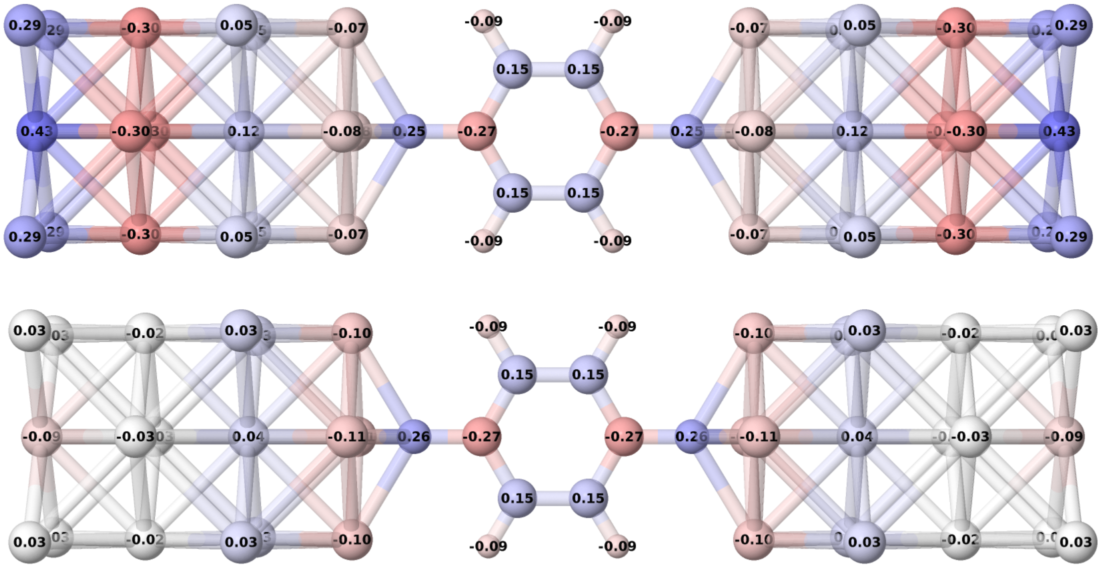

Figure 2.6: Error correction in the Al-1,4-benzenediol-Al test system. **Top**: WBL including the outer blocks with a cut-off at $E_B = -3.0$ H. **Bottom**: WBL without outer blocks.

Chapter 3

Dynamic admittance

3.1. Introduction

We first stay in the linear regime and focus on the full frequency-dependent ac response; its amplitude and phase shift with respect to the (small) voltage. Note that the code is fully capable of tackling this problem for finite bias, but the quantity we are investigating in this section is the frequency-dependent admittance $Y(\omega)$ defined in linear response. It connects the Fourier transforms of the current response $I_\alpha(t)$ and the voltage signal $V_\alpha(t)$ applied to lead α.

$$I_\alpha(\omega) = \sum_\beta Y_{\alpha\beta}(\omega) V_\beta(\omega) \tag{3.1}$$

Re$[Y(\omega)]$ will be called dynamic conductance, Im$[Y(\omega)]$ dynamic susceptance. We are only concerned with the current flowing through the device from one side to another in a two-terminal system without a gate, so we set $\alpha = \mathrm{L}$ (left device-lead-interface) and $\beta = \mathrm{R}$ (right device-lead interface) and thus $I = I_L$, $V = V_R$, $Y = Y_{LR}$. The input signal $V(t)$ is, for now, purely sinusoidal.

$$V(t) = V_{ac}\sin(\omega_0 t) \tag{3.2}$$

In recent years, theoretical descriptions of this quantity - although hard to access experimentally - became more numerous. The treatments include energy [65, 66, 67, 68] and time [69] domain approaches. In the following, we apply our time-resolved method to obtain information about the high frequency admittance in molecular junctions consisting of up to 200 atoms in the device region alone.

3.2. Connection of admittance and dc transmission

In 1993, Fu and Dudley [70] connected the linear response theory for the admittance with the Fisher-Lee relations [48] to obtain a Landauer-like expression for $Y(\omega)$ with transmission and reflection amplitudes described by Green's functions. This way, they could derive analytical expressions for the frequency-dependent admittance of a single level system. Given a resonant single level transmission as

$$T(E) = \frac{\gamma^2}{(E - E_0)^2 + \gamma^2} \tag{3.3}$$

with E_0 being the energy of the single level and γ its broadening, the admittance then reads

$$\mathrm{Re}[Y(\omega)] = G_0 \frac{\gamma}{2\omega} \left[\arctan\left(\frac{\mu - E_0 + \omega}{\gamma} \right) - \arctan\left(\frac{\mu - E_0 - \omega}{\gamma} \right) \right] \tag{3.4}$$

$$\mathrm{Im}[Y(\omega)] = G_0 \frac{\gamma}{4\omega} \ln \left\{ \frac{[(E_0 - \mu + \omega)^2 + \gamma^2][(E_0 - \mu - \omega)^2 + \gamma^2]}{[(E - \mu)^2 + \gamma^2]^2} \right\} \tag{3.5}$$

Here, μ is the chemical potential and G_0 the conductance quantum. In our time-resolved simulations, we obtain $Y(\omega)$ directly from the current and voltage signals:

$$Y(\omega) = \frac{I(\omega)}{V(\omega)} \tag{3.6}$$

To access $I(\omega)$, one can carry out multiple calculations of $I(t)$ for varying driving frequencies ω_0 and extract the respective amplitude and phase shift, or one uses a voltage input signal $V(t)$ which contains all frequencies and takes Fourier transforms of voltage and current. The latter certainly makes more sense when trying to access a frequency-dependent quantity in one single run, and while the numerical efficiency of TD-DFTB would allow both ways for junctions the size of our test systems, single frequency calculations are just a waste of resources and inconvenient for the very large systems we would like to investigate later.

In order to set up the Fourier (or rather: Laplace) transform, we conduct a small test to see which input signal works well as is also mentioned in [63]. Defining

$$V(\omega) = \int_0^\infty V(t) e^{i\omega t} dt \tag{3.7}$$

we look for a suitable temporal profile of the voltage which can in principle be arbitrary. However, our usual choice of an initially dampened exponential profile

$$V(t) = V_0(1 - e^{-\frac{t}{T}}) \tag{3.8}$$

turned out to be problematic since the Fourier transform does not exist for $\omega \to 0$ without the addition of an artificial dampening factor $e^{\kappa t}, \kappa < 0$. As the results for different choices of this arbitrary dampening where far from optimal, we tried a Lorentzian input signal of the form

$$V(t) = \frac{V_0}{\pi} \frac{\gamma}{(t - t_0)^2 + \gamma^2} \tag{3.9}$$

which yielded satisfying results (see Fig 3.1 for a comparison to single frequency calculations).

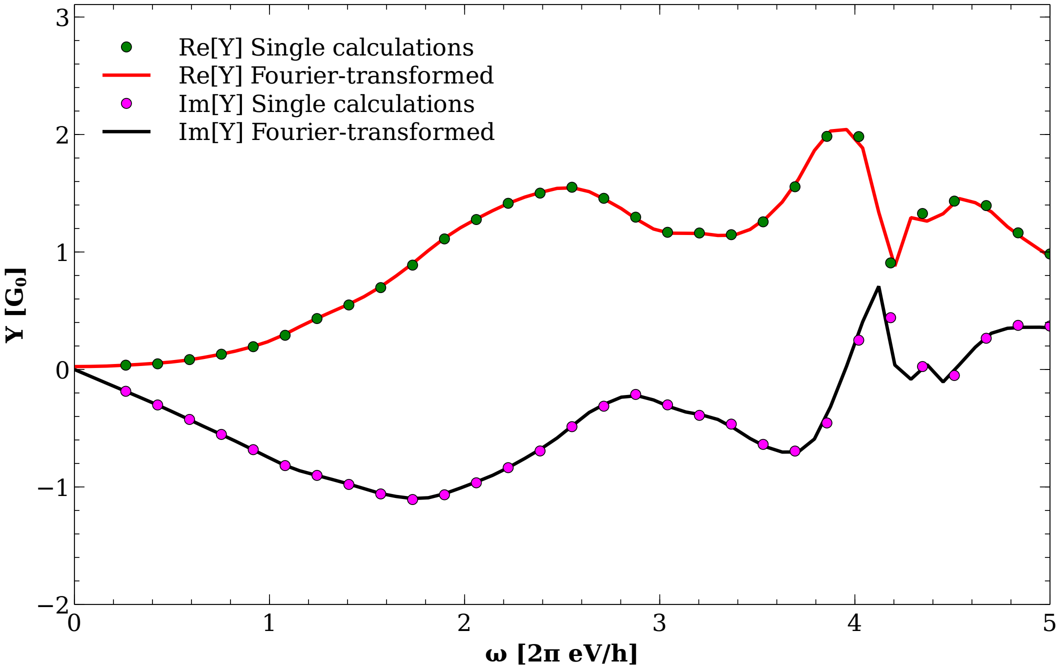

Figure 3.1: Reference from single frequency calculations compared to a Fourier-transformed Lorentz voltage profile.

Therefore we can use the Fourier transform of a Lorentzian voltage signal and its response in the following. Looking at the real and imaginary part of the admittance for our usual test system in Fig. 3.2 and comparing it with the Fu-Dudley result of a single level, we can see a qualitative resemblance [63]. The response of the system is capacitive, for small frequencies the real part increased quadratically whereas the imaginary part decreases linearly, in accordance to a classical RC circuit, where the admittance expanded to second order in frequency reads:

$$Y^{RC}(\omega) \approx -i\omega C + \omega^2 C^2 R \tag{3.10}$$

At first sight, the transmission obtained within tranDFTB using Eq. 1.55 certainly offers the interpretation of molecular levels inducing the features in the admittance. This can be seen by the Fu-Dudley result for a single level at $|\mu - E_0| = 2$ eV also shown in the picture, which roughly corresponds to the energy of the first larger broadenings in the transmission. A second large structure around $|\mu - E_0| = 4$ eV might then be responsible for the second Fu-Dudley-like resonance in the admittance with its again decreasing susceptance and increasing conductance. Since the effect of the level broadening on the admittance becomes smaller the further the resonance is away from the Fermi energy, the qualitative agreement seems very promising.

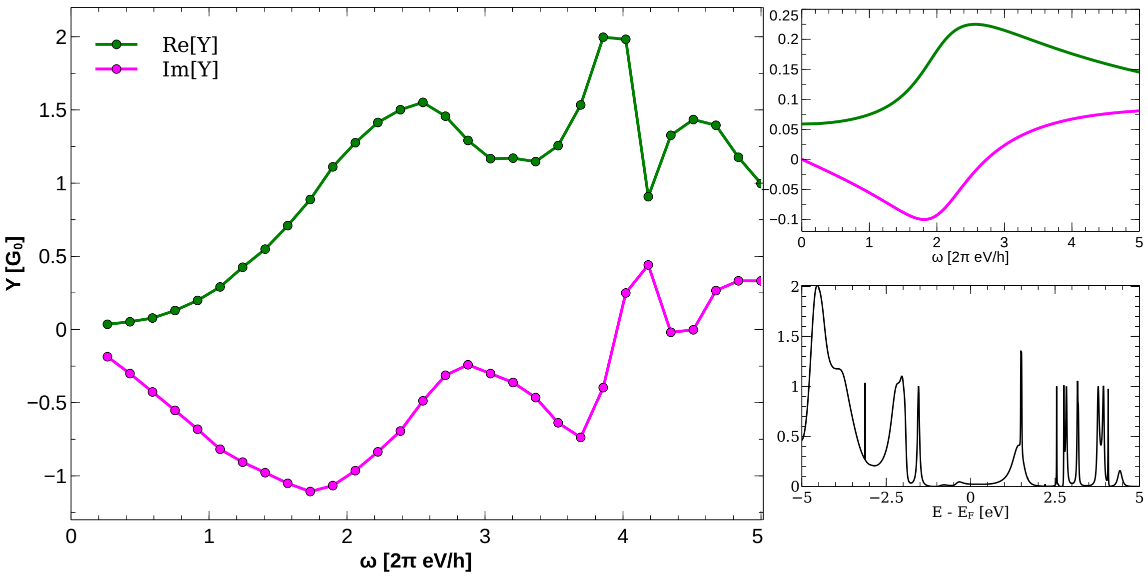

Figure 3.2: **Left**: Real and imaginary part of the admittance for the Al-1,4-benzenediol-Al system. **Top right**: Single level result for $|\mu - E_0| = 2$ eV and $\gamma = 0.5$ eV according to Fu and Dudley. **Bottom right**: transmission of the investigated system.

In order to test and demonstrate the numerical efficiency of our method, we then calculated the dynamic admittance for a comparatively large capacitive system, a hexene molecule contacted to gold leads at the (111) surface, see Fig. 3.3.

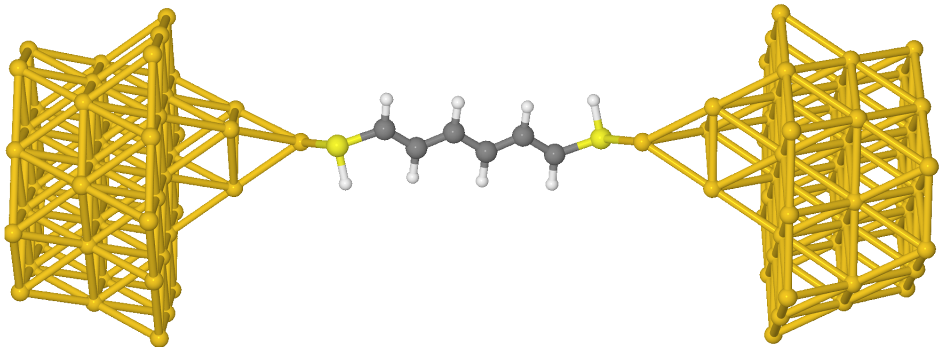

Figure 3.3: Au-Hexen-Au junction consisting of 172-86-172 atoms.

The device consists of 86 atoms, the leads of 172 atoms each. The experimental bulk lattice constant of roughly 4.08 Å is used [71] and the valence orbitals are captured up to l=2 for gold. A total evolution time of 40 fs with a time stepping of 0.04 fs means the calculation of 1000 individual time steps for a system this large. Fig. 3.4 shows the resulting admittance. In accordance to the earlier interpretation, the curve becomes more structured with a lot of smaller features, which would fit the larger amount of sharp peaks in the respective transmission.

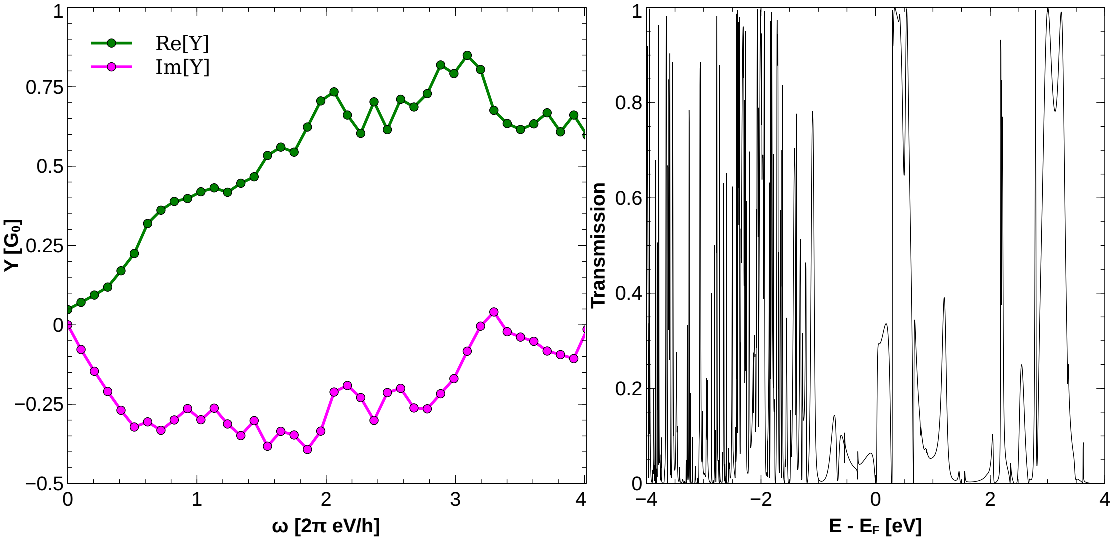

Figure 3.4: **Left**: Admittance curve for the Au-Hexen-Au system, calculated from the Fourier transform of a Lorentzian voltage input. **Right**: Transmission of the junction.

Encouraged by these results, we aimed to find a way of calculating or estimating the admittance out of the information contained in the dc steady state transmission for a multilevel system. The transmission was fitted by using the level positions and broadenings known from the equilibrium calculations leaving the interference phases between the peaks as free parameters. A superposition of interfering Fu-Dudley resonances was then constructed, but the predictions were far off compared to the admittance calculations. Further doubts regarding the interpretation of the dc transmission carrying the relevant information for the admittance arose when looking at other capacitive systems with aluminum leads. In Fig. 3.5 we show the admittance curves for Al-octane-Al and Al-octene-Al. The overall shapes are similar, the changes due to the different molecular transmission smaller than anticipated. It is not at all clear that one can find a one-to-one correspondence from transmission to admittance judging by these results.

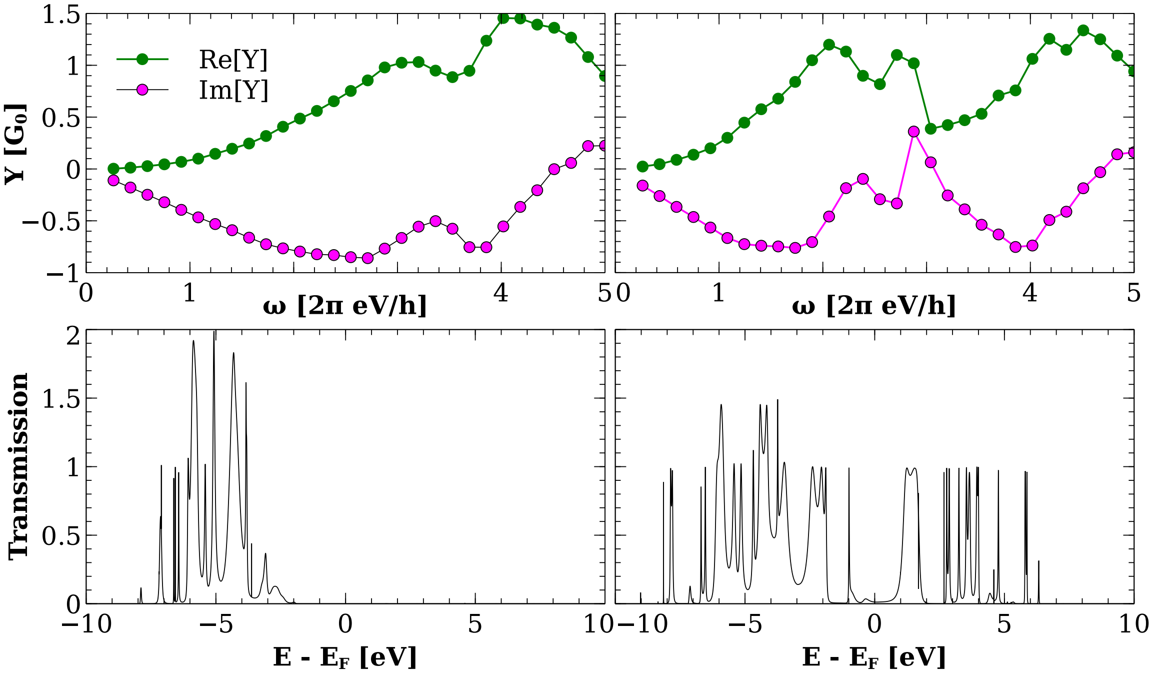

Figure 3.5: **Left**: Al-octane-Al admittance and transmission. The transmission features a large gap due to the lack of π-systems in the molecule. There is no transmission up to exceedingly high energies. **Right**: Al-octene-Al admittance and transmission.

We face a similar issue when now investigating an inductive system. In the following we look at a carbon chain with 16 atoms in the device region, inductive due to the perfect transmission at and near the Fermi energy originating from the π bonds.

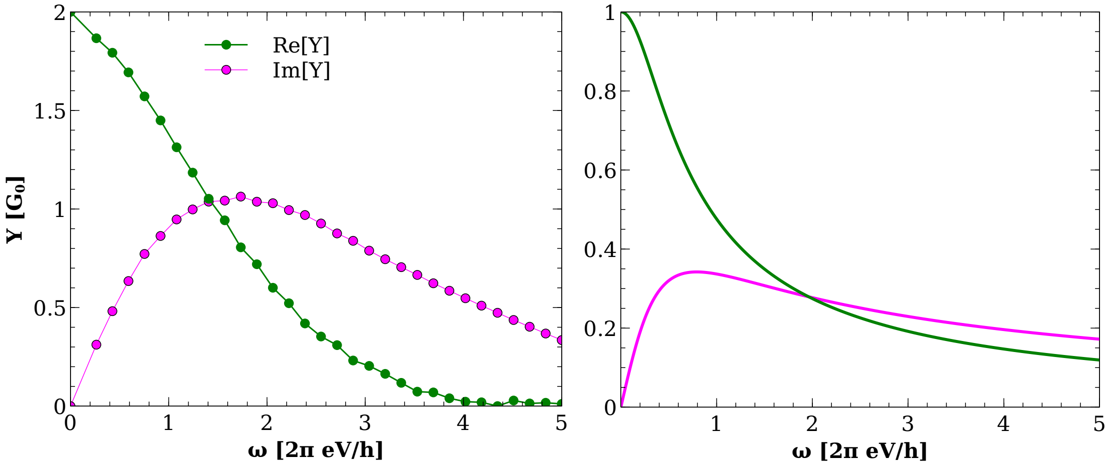

Figure 3.6: **Left**: carbon chain admittance and transmission. **Right**: Single level theory result for a level at $E = E_F$ with a width of $\gamma = 0.8$ eV

In Fig. 3.6 we see that the qualitative shape of the calculated carbon chain admittance is very similar to the Fu-Dudley approach for a single resonant level at the Fermi energy, just for a transmission of $T(E_F) = 2$ instead of 1. While the overall behavior is fine and expected, the transmission away from the Fermi energy does not drop significantly as it would in the single level picture. Looking for a connection between admittance and transmission, it apparently makes not much sense that the carbon chain admittance drops to zero at energies where it is still transparent to carriers, see Fig. 3.7.

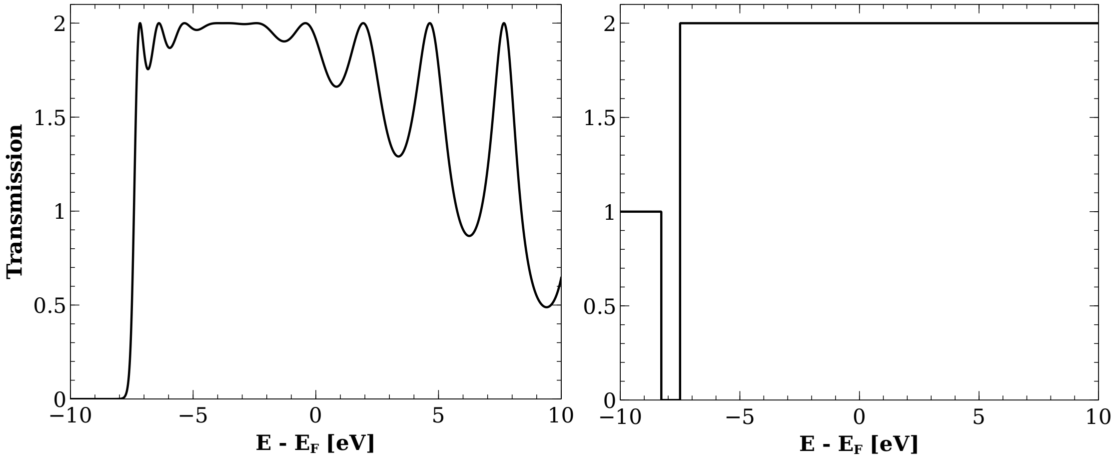

Figure 3.7: **Left**: carbon chain transmission in the wide band limit (WBL). **Right**: transmission without the use of the WBL. Both calculated within tranDFTB.

The unphysical oscillations in the carbon chain transmission are an artifact of the WBL and not limited to our code or approach. In the region of $E - E_F = \pm 5$ eV, the transmission is far too large for the admittance to drop asymptotically towards zero. So either the connection between transmission and admittance is far more complicated than previously thought, or the admittance behavior is decided to a very large extent solely by the transmission in the vicinity of the Fermi energy. There is no doubt in the identification of an inductive system in comparison to a capacitive junction, but a rigorous interpretation of the precise shape influenced by the molecular resonances is not possible at this point.

3.3. Influence of the contacts

When comparing capacitive systems, the qualitative shape of the admittance does not heavily depend on the molecule in the junction. In order to isolate the contribution of the displacement current and the influence of the leads, we constructed systems without any molecule inbetween, effectively plate capacitors with finite surface area. To our surprise, the admittance did not change much when we omitted the (capacitive) molecule, again suggesting that the molecular transmission is only important near the Fermi energy, see Fig. 3.8

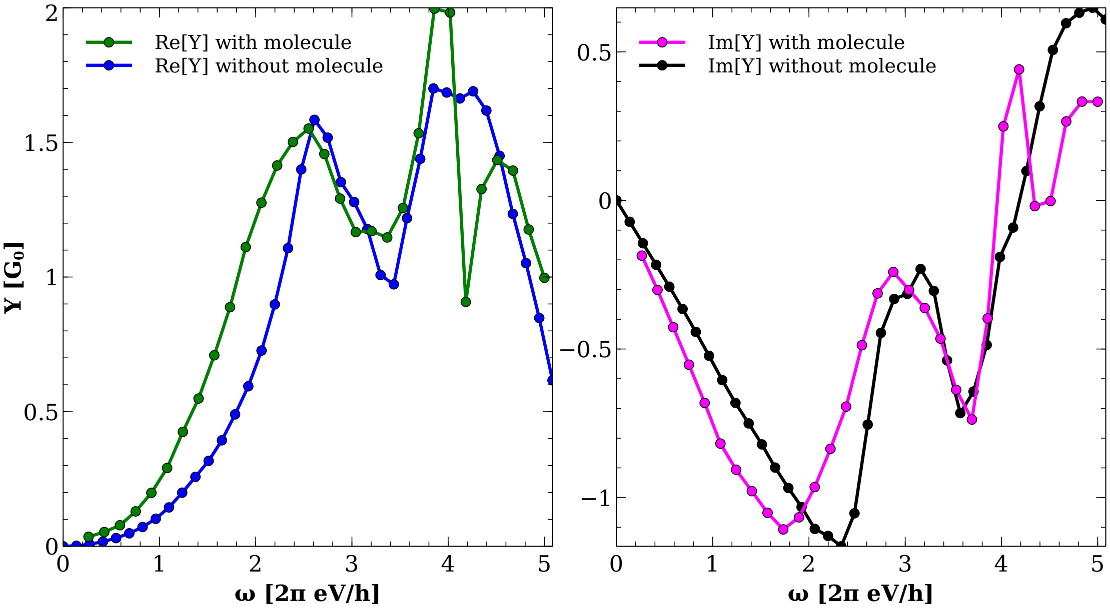

Figure 3.8: Comparison of the Al-1,4-benzenediol-Al system with and without the central molecule. **Left**: Real parts of the admittance, **Right**: Imaginary parts of the admittance

Therefore, if the molecule features a gap around the Fermi Energy and the system behaves like a capacitor in consequence, the admittance is dominated by the displacement currents in the leads even for frequencies high enough to reach molecular resonances. This is not straightforward as it could have been possible for the molecular resonances to bridge the capacitor, increasing the inductive features of the system.

If one simply replaces the contact aluminum atoms with gold atoms, the admittance curve retains the correct capacitive features, but still changes considerably, see Fig. 3.9. The absolute value of the conductance and susceptance becomes smaller, respectively, and the curve is more structured, presumeably due to the increased density of states and also observed in Fig. 3.4.

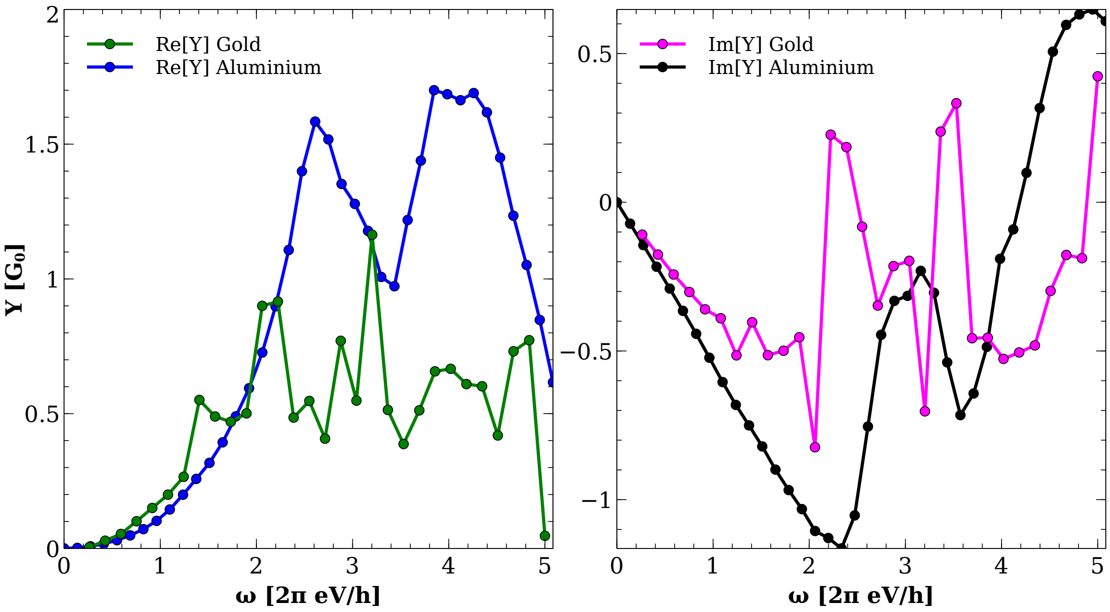

Figure 3.9: Otherwise identical plate capacitors made out of aluminum and gold, respectively. **Left**: Real parts of the admittance, **Right**: Imaginary parts of the admittance

In light of the importance of the contacts, the question might arise why the admittance curves of, for example, the octane molecule in Fig. 3.5 still look considerably different than the 1,4-benzenediol system. The reason is that in the former, the aluminum contacts have to be further apart to fit the molecule in, decreasing the geometrical capacitance of the system. Looking at Eq. 3.10, this in turn should result in a slower raise of the conductance and slower decline of the susceptance near the Fermi energy. This is exactly what happens, as can be seen in Fig. 3.10. Again, the capacitive molecule does not play a major role in comparison to the electronic structure and geometry of the leads.

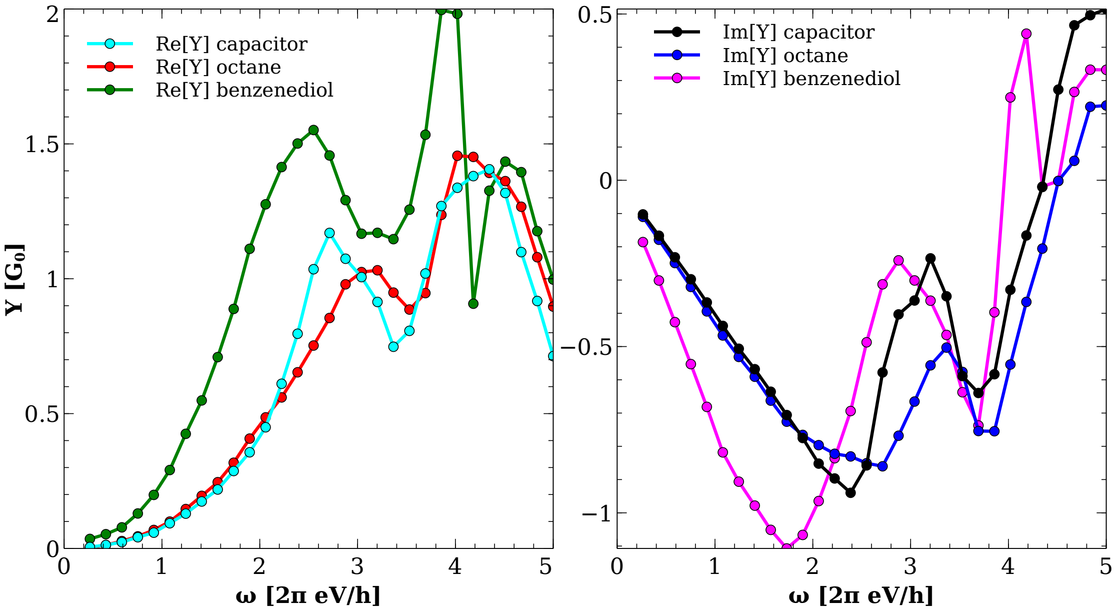

Figure 3.10: Al-1,4-benzenediol-Al, Al-octane-Al and a capacitor with surface distance equal to the one in the octane system. **Left**: Real parts of the admittance, **Right**: Imaginary parts of the admittance

3.4. Comparison with other approaches

In the literature, the theory of time dependent transport in the framework of the NEGF formalism was published in 1994 by Jauho et al. [72] and implications for ac transport further worked out by Anantram and Datta [10]. The main equation for the particle current in a two-terminal geometry reads according to Jauho et al.:

$$I(t) = -\frac{1}{\pi}\int_{-\infty}^{t} dt_1 \int d\epsilon \; \mathrm{Im}\mathrm{Tr}\left\{e^{-i\epsilon(t-t_1)}\Gamma^L(\epsilon, t, t')[G^<(t, t_1) + f_l(\epsilon)G^r(t, t_1)]\right\} \tag{3.11}$$

However, both publications only described the particle current as is sufficient for the calculation of time-averaged currents. While this expression is comprehensive for the purpose of describing rectification (discussed in the next chapter), calculation of ac quantities like the dynamic admittance also need displacement currents to be accounted for. As it stands, without displacement currents, the above equation satisfies neither current conservation nor gauge invariance [10, 73]. However, the total current including both particle and displacement current is conserved in systems with central inversion symmetry [74]. The total displacement current is accessible via the derivative of the ac induced total pile-up charge Q_D in the device region, $I^d(t) = \frac{dQ_D}{dt}$, but it was not straightforward how to distribute it over the probes of a multi-probe system. It was found that the total dynamic admittance from probe α to probe β looks like [75]

$$Y_{\alpha\beta} = Y^c_{\alpha\beta} - Y^d_\beta \frac{\sum_\gamma Y^c_{\alpha\beta}}{\sum_\gamma Y^d_\gamma} \tag{3.12}$$

with Y^c denoting the conduction from the particle current. For symmetric two-probe systems like ours, this reduces to the intuitive and simple form

$$Y_{\alpha\beta} = Y^c_{\alpha\beta} + \frac{1}{2} Y^d_\beta \tag{3.13}$$

as can be derived easily from current conservation and gauge invariance. This way to include displacement currents and restore the basic conservation laws is called the *current partitioning* approach. Additionally employing the wide band limit, the NEGF particle current and displacement current lead to an admittance of the form:

$$Y_{\alpha\beta}(\omega) = \frac{1}{2\pi\omega} \int_{-\infty}^{\infty} d\epsilon \, [f_\beta(\epsilon) - f_\alpha(\epsilon + \omega)] \times \tag{3.14}$$

$$\mathrm{Tr}[G(\epsilon + \omega)\Gamma_\beta G^\dagger(\epsilon)\Gamma_\alpha] - i\delta_{\alpha\beta}\mathrm{Tr}[G(\epsilon + \omega)\Gamma_\alpha - \Gamma_\alpha G^\dagger(\epsilon)] \tag{3.15}$$

$$- i\frac{1}{4\pi} \int_{-\infty}^{\infty} d\epsilon \, [f_\beta(\epsilon) - f_\beta(\epsilon + \omega)]\mathrm{Tr}[G(\epsilon + \omega)\Gamma_\beta G^\dagger(\epsilon)] \tag{3.16}$$

and the displacement current contribution in the third line disappears for $\omega \to 0$. To arrive at this equation, one also has to linearize the two-time Green's functions (or two-energy as in Ref.[10]) for small ac voltages with respect to the steady state and ignore the ac potential in the device region. Therefore, the above equation is clearly an approximation, although it should be a reasonable one when looking into linear response quantities like the admittance. On the other hand, it is unclear if the linearization holds up for frequencies in the optical regime and how significant the effect of ignoring the induced ac potential could prove.

In order to further investigate the shape of our admittance curves, we decided to compare our time-resolved results to an own implementation of the above formula. Due to the size of our systems, the brute force integration would take a considerable amount of time. However, defining

$$H^{eff}_{ij} = H_{ij} + (\Sigma^r_L)_{ij} + (\Sigma^r_R)_{ij} = \sum_k B_{ik} H_k (B^{-1})_{kj}$$

where the matrix B contains the eigenvectors of H^{eff} and H_k is a vector consisting of the respective eigenvalues, we quickly arrive at an analytical integration which can be calculated in a matter of minutes with the SCC-shifted Hamiltonian, the overlap matrix and the self-energy from the time-independent part of tranDFTB:

$$\begin{aligned}
&\left[\int_{E_F-\omega}^{E_F} dE\, G^r(E+\omega)\Gamma_\beta G^a(E)\right]_{in} \\
&= \sum_{kl} \int_{E_F-\omega}^{E_F} dE\, G^r_{ik}(E+\omega)(\Gamma^r_\beta)_{kl} G^a_{ln}(E) \\
&= \sum_{jklm} \int_{E_F-\omega}^{E_F} dE\, B_{ij}[E+i\eta-(H_j-\omega)]^{-1}(B^{-1})_{jk}(\Gamma^r_\beta)_{kl}(B^{-1})^*_{ml}[E-i\eta-H^*_m]^{-1}(B^*)_{nm} \\
&= \sum_{jklm} B_{ij}(B^{-1})_{jk}(\Gamma^r_\beta)_{kl}(B^{-1})^*_{ml} \int_{E_F-\omega}^{E_F} dE\, [E+i\eta-(H_j-\omega)]^{-1}[E-i\eta-H^*_m]^{-1}(B^*)_{nm} \\
&= \sum_{jklm} B_{ij}(B^{-1})_{jk}(\Gamma^r_\beta)_{kl}(B^{-1})^*_{ml} \int_{E_F-\omega}^{E_F} dE\, \frac{[E+i\eta-(H_j-\omega)]^{-1}-[E-i\eta-H^*_m]^{-1}}{[E-i\eta-H^*_m]-[E+i\eta-(H_j-\omega)]}(B^*)_{nm} \\
&= \sum_{jklm} B_{ij}(B^{-1})_{jk}(\Gamma^r_\beta)_{kl}(B^{-1})^*_{ml} \frac{\ln\left(\frac{E_F-(H_j+i\eta)+\omega}{E_F-(H_j+i\eta)}\right)-\ln\left(\frac{E_F-(H_m+i\eta)^*}{E_F-\omega-(H_m+i\eta)^*}\right)}{(H_j-i\eta-\omega)-(H_m-i\eta)^*}(B^*)_{nm} \\
&= \sum_{jm} B_{ij}R_{jm} \frac{\ln\left(\frac{E_F-(H_j+i\eta)+\omega}{E_F-(H_j+i\eta)}\right)-\ln\left(\frac{E_F-(H_m+i\eta)^*}{E_F-\omega-(H_m+i\eta)^*}\right)}{(H_j-i\eta-\omega)-(H_m-i\eta)^*}(B^*)_{nm}
\end{aligned}$$

Using this integration, Eq. 3.16 reproduces exactly the result of Fu and Dudley discussed earlier if applied on a single level.

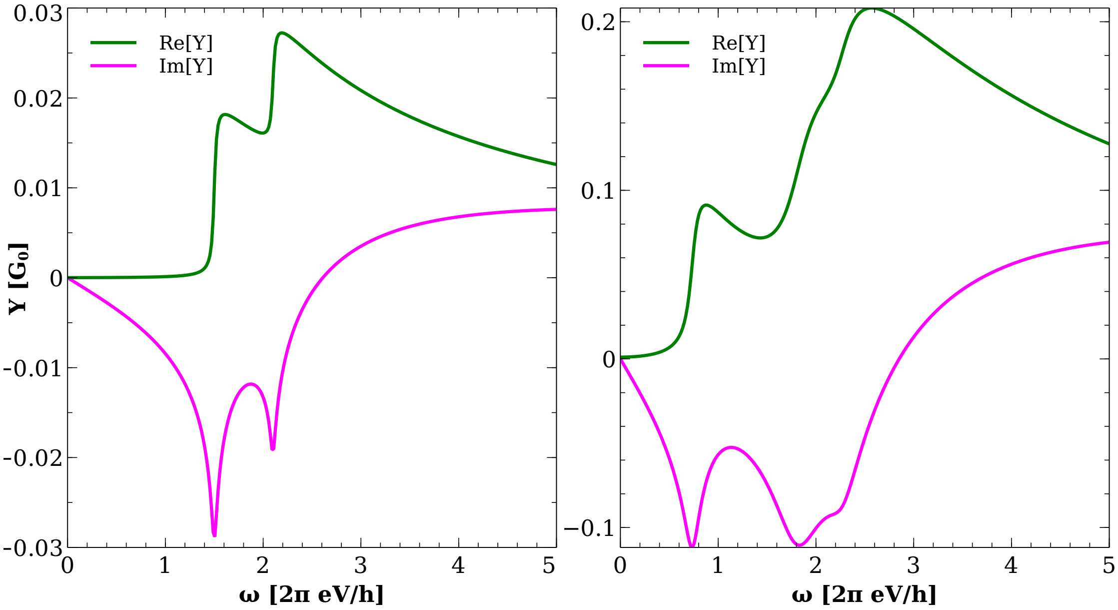

Figure 3.11: Example predictions for the admittance using linearized Green's functions in the wide band limit, as described in the text. **Left**: Two levels at $E_1 = 1.5$ eV and $E_2 = 2.1$ eV with $\Gamma = 0.02$ eV. **Right**: Three levels at $E_1 = 0.7$ eV, $E_2 = 1.8$ eV, $E_3 = 2.3$ eV and $\Gamma = 0.2$ eV.

In Fig. 3.11 one can see for two or three levels that the results of this equation look similar to superposed single level Fu-Dudley peaks. Their height depends mainly on the coupling of the respective levels to the contacts and their distance from the Fermi energy. While the qualitative shape of the single resonances is in good agreement with our results, the overall superposition for our test systems is not.

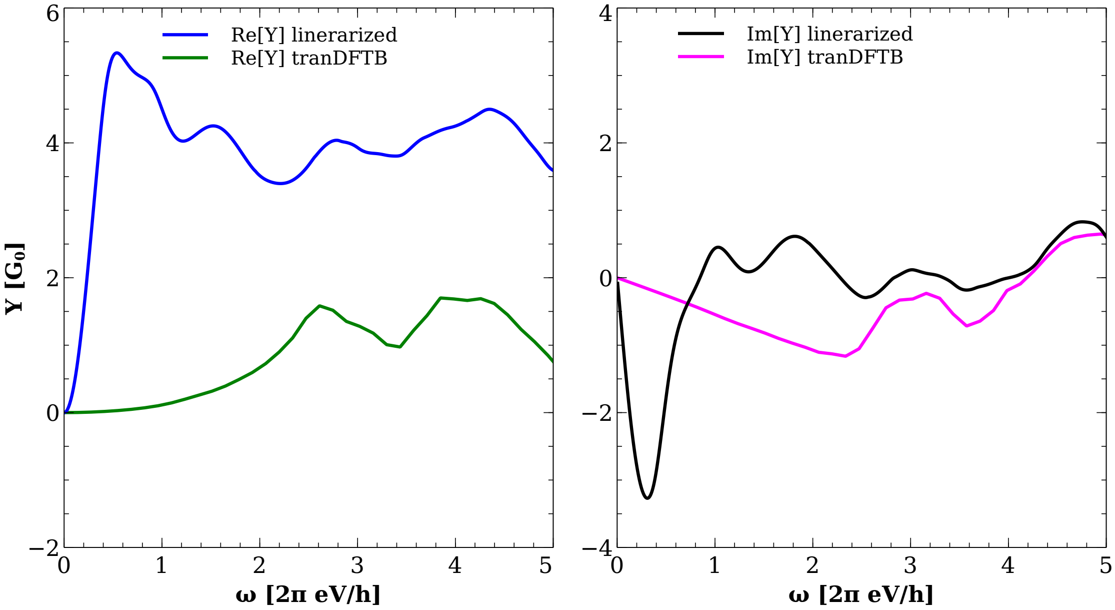

Figure 3.12: Comparison of the tranDFTB result for an aluminum capacitor with the linearized theory resulting from an own implementation. **Left**: real part of the admittance. **Right**: imaginary part of the admittance.

In Fig. 3.12 you can see that from $\hbar\omega \approx 2$ eV to higher energies there is a striking resemblance between the qualitative shape of the curves. However, especially the real part is much larger in the approach we chose to compare to, and the initial response at lower frequencies is completely different. While the agreement at higher energies is unlikely to be a coincidence, we initially could find no reason why the linearized approach exhibits such a large resonance at about 0.3 eV. However, we can easily remove one of the biggest differences between the approaches by turning off the self-consistent update of the ac device potential and carry out the propagation with the dc potential distribution only. The result is shown in Fig. 3.13. We now recover the peak positions, their relative heights and their broadening with satisfying accuracy, but the overall magnitude of the admittance is still different. Note that in order to match the first large peak, the result of the linearized approach had to be divided by two. This is a coincidence, as this factor is not systematic when looking at different junctions like the carbon chain below.

A very important point here is the massive influence of the ac potential on the admittance despite using very small ac amplitudes ($|V_{ac}| = 5 \cdot 10^{-7}$ V). Charge accumulations and lag between the outer field and the response of the potential within the device change the behaviour of the system considerably.

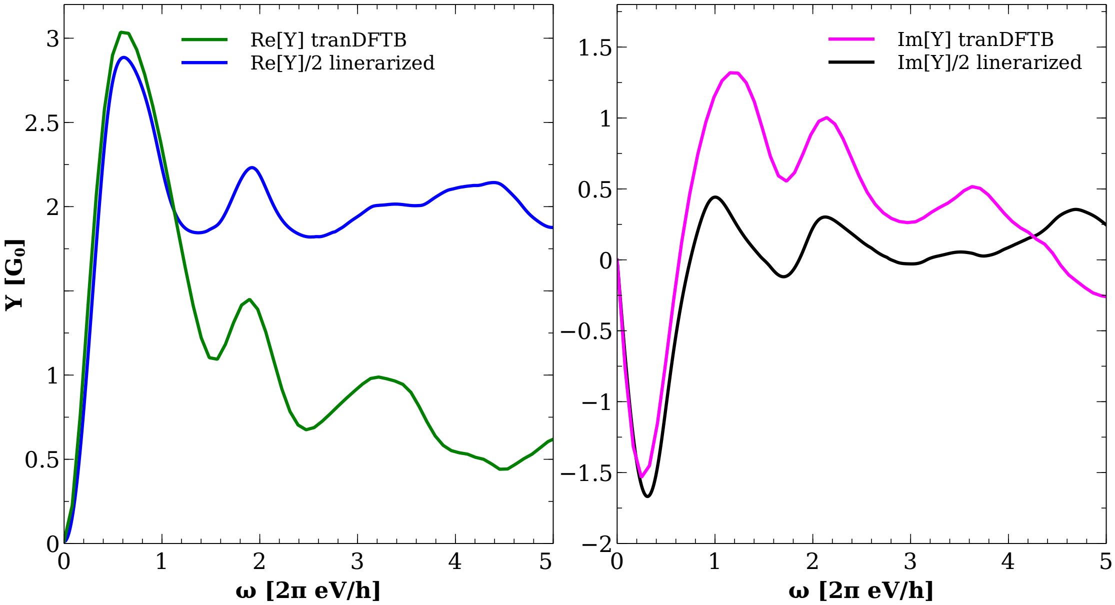

Figure 3.13: The above comparison between the linearized approach and the tranDFTB result with the self-consistent update of the device potential switched off. **Left**: real part of the admittance. **Right**: imaginary part of the admittance.

Just as a reminder: due to the system being a plate capacitor, there is zero dc transmission through the junction and the whole response is due to displacement current depending on the electronic structure of the leads. Thus, in equation 3.16, only the term in the last line contributes.

Next, we check the influence of the ac potential on the admittance of the carbon chain. First, we show the full tranDFTB including the potential update and compare it to the linearized approach, see Fig. 3.14.

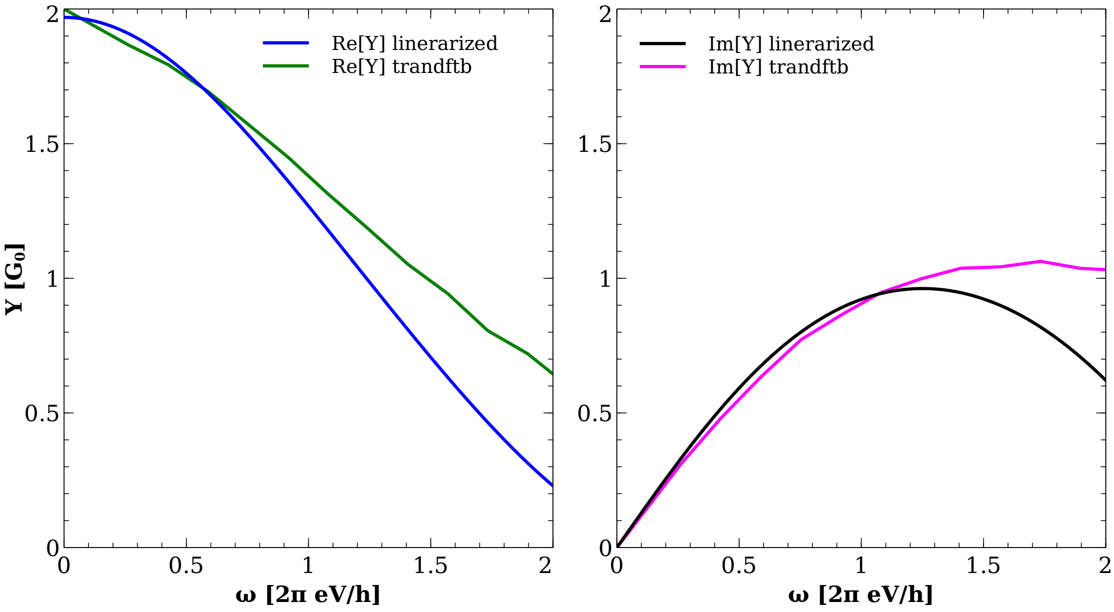

Figure 3.14: Comparison of the tranDFTB result for a carbon chain with the linearized theory resulting from an own implementation. **Left**: real part of the admittance. **Right**: imaginary part of the admittance.

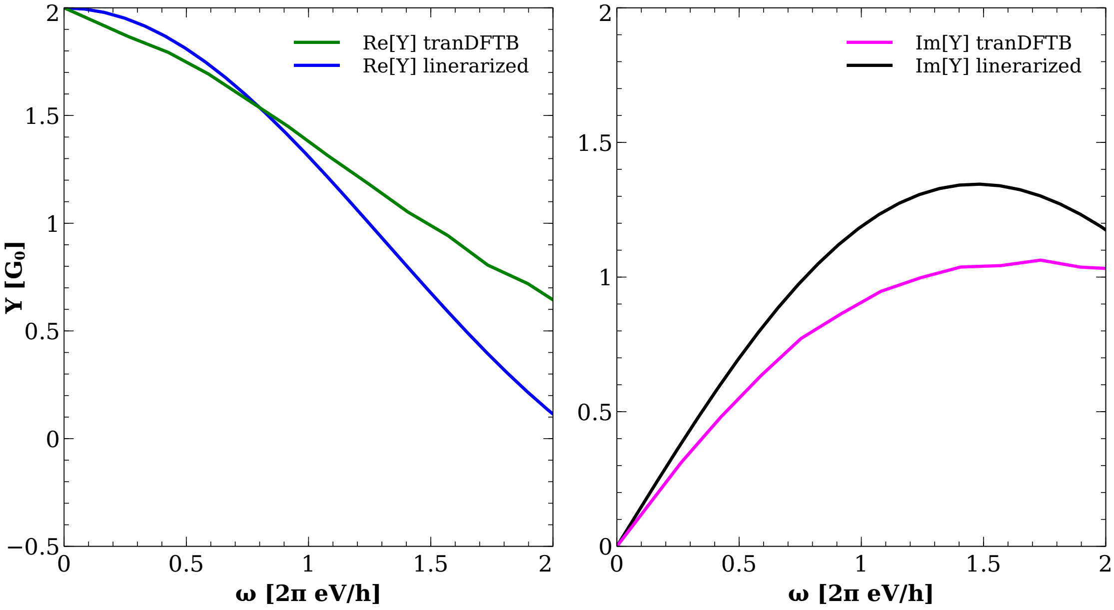

Figure 3.15: The above comparison between the linearized approach and the tranDFTB result with the self-consistent update of the device potential switched off. **Left**: real part of the admittance. **Right**: imaginary part of the admittance.

We see an inductive system in which the particle current contributes about a third to the total current, with the displacement current still dominating. Even with the potential update still turned on, we do not observe a large quantitative difference between the admittance curves of the carbon chain as present for the capacitive system. Upon neglecting the ac potential, there is also no systematic factor of two visible, as mentioned above (see Fig. 3.15). However in this case, the agreement becomes slightly worse.

It is striking that the corrections induced by taking into account the time-dependent ac potential within the device region are far larger for capacitive systems. It came to our attention that very recently, the current partitioning approach was compared to an analytical expression taking into account the self-consistent potential update [76]. The author shows that the current partitioning as used in the literature is only valid for perfect conductors. This does not only mean that the transmission near the Fermi energy has to be equal to the number of conduction channels, the system also has to stay perfectly conducting when applying an ac bias. This is in general not true since especially for higher frequencies, initially inductive systems can become capacitive [67].

This remark serves as a good explanation why the deviations induced by the ac potential profile are much stronger for a capacitive system (Fig. 3.12) compared to the carbon chain which is perfectly conducting in the vicinity of the Fermi energy (Fig. 3.14). The requirement of the system being a perfect conductor directly translates into the requirement of an uniform and flat potential distribution within the device region. Therefore, we investigate its shape as a function of frequency. To this end, we take the time-dependent potential $\delta V_H(\mathbf{r}, t)$ in the vicinity of the carbon chain atoms along the transport direction (x) and Fourier-transform the result, yielding $\delta V_H(x, \omega)$, then plot the distribution for various frequencies. The result is shown in Fig. 3.16. It turns out that the carbon chain potential, initially showing the flat shape in accordance to the current partitioning approach, becomes increasingly linear (i.e. it develops a resistance) for higher frequencies. This is in line with the report of [76].

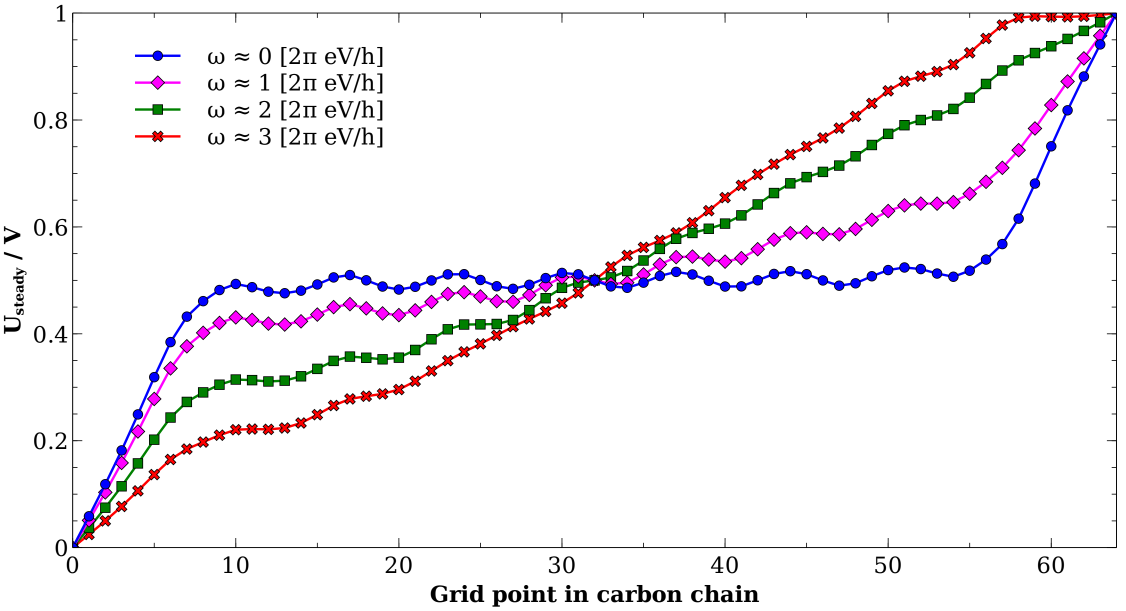

Figure 3.16: Plots of the device potentials induced by the ac voltage at various frequencies in the carbon chain.

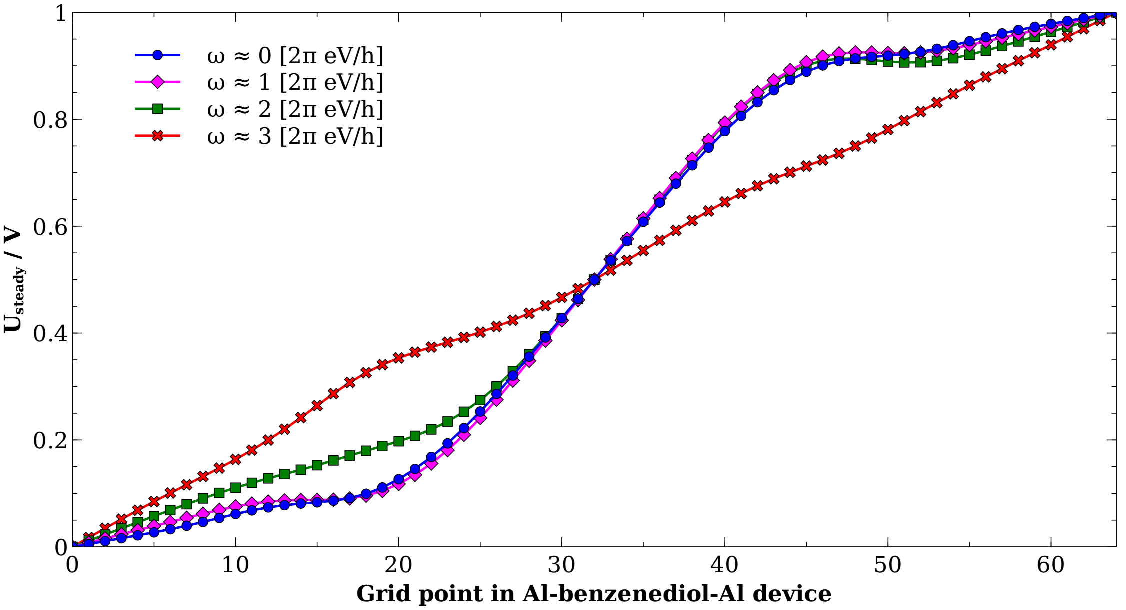

Figure 3.17: Plots of the device potentials induced by the ac voltage at various frequencies in the Al-benzenediol-Al system.

Therefore, the current partitioning approach is only a good approximation near the Fermi energy of the carbon chain, but becomes increasingly inaccurate the higher the frequency is chosen, supporting our admittance results in Fig. 3.14. In contrast, the Al-benzenediol-Al system acts as a resistance to ac transport even at low frequencies with a linear potential across the molecule. While the principle layers out of lead material are well conducting at first, even they develop a non-flat potential distribution beyond $\hbar\omega \approx 2$ eV. (see Fig. 3.17). For capacitive systems, the current partitioning approach is therefore inaccurate across the whole frequency range in use. Qualitative and quantitative deviations of unknown magnitude are expected and could well explain the large corrections by our approach in Fig. 3.12. Furthermore, the ac potential update is apparently shifting lead levels carrying the ac current, as can be seen from the peak positions in Fig. 3.13 relative to Fig. 3.12. It can now be assumed that the influence of these level shifts is larger in capacitive systems with their structured transmissions than in the carbon chain, where conducting levels are very numerous around the Fermi energy before and after the shift.

What is left to discuss is which approximations are responsible for the differences between the approaches still present even after switching off the ac potential update. It is possible that by doing this, we introduce errors to our method since one of the prerequisites for the propagation is a smooth transition of the potential from the device to the lead, as mentioned earlier. This was the reason why lead material had to be included into the device region in the first place. This requirement also does not allow for very simple test systems to be calculated, and we have to make due with large lead-molecule-lead systems or atomic chains. Therefore, when comparing different approaches for these large systems, it is also hard to identify which consequences result from certain approximations.

One deliberate error that is certainly present within our method is the neglection of the outer blocks of the density matrix in the steady state and the time dependent propagation, as described earlier. One has to make sure that the influence of the outer blocks on the admittance is small enough to justify this. As can be seen in Fig. 3.18, the comparison with a calculation including outer blocks with an arbitrary Green's function lower integration cutoff at $E_B = -3.0$ H did not change the admittance significantly. The same holds true for the carbon chain, our example for inductive systems.

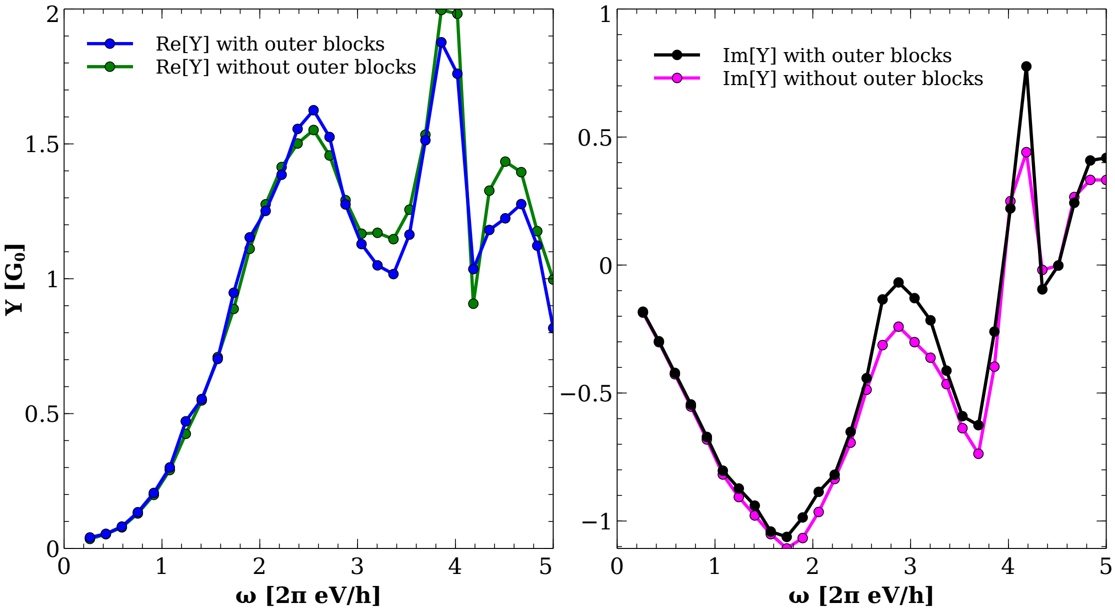

Figure 3.18: Al-1,4-benzenediol-Al with (integration cutoff $E_B = -3.0$ H) and without the outer blocks of the density matrix in the time-independent part. **Left**: real part of the admittance. **Right**: imaginary part of the admittance.

As can be seen from Eq. 3.10, the ominous factor of two appearing in the size of the first resonance of the capacitive system can be directly attributed to a larger capacitance. Therefore, we will further analyze the aluminum capacitor in the next section, checking the plausibility of its qualitative behaviour.

3.5. Capacitance and induced charges

The quantity we are interested in is the frequency dependent complex electrochemical capacitance $C(\omega)$, which is directly related to the admittance. [77, 78]

$$C(\omega) = i\frac{1}{\omega}Y(\omega) \tag{3.17}$$

Büttiker [79, 80] analyzed the electrochemical capacitance in the Thomas-Fermi approximation to the Lindhard description of screening; the major aspects about its differences to the conventional capacitance of a macroscopic capacitor will be restated in the following.

A macroscopic capacitor can be described by an electrostatic capacitance C_0 in series with two dc-resistances $R = R_1 + R_2$, the respective admittance given by Eq. 3.10. The frequency-dependent electrochemical capacitance $C(\omega)$ of a mesoscopic capacitor does now additionally depend on the generalized global density of states (GDOS) $D_{I,II}(\omega)$ of the respective plates:

$$\frac{1}{C(\omega)} = \frac{1}{C_0} + \frac{1}{D_I(\omega)} + \frac{1}{D_{II}(\omega)} \tag{3.18}$$

with

$$D_\alpha(\omega) = \mathrm{Tr} \int \frac{dE}{2\pi} \frac{f(E) - f(E+\omega)}{\omega} [G^r(E+\omega)\Gamma_\alpha G^a(E)] \tag{3.19}$$

and in our case $D_I(\omega) = D_{II}(\omega)$. One can picture Eq. 3.18 as an electrostatic capacitance in series with two frequency-dependent quantum capacitors. Depending on the size of the capacitor, the correction terms can be of the same order as the electrostatic (geometrical) capacitance. In the limit of a macroscopic capacitor, the GDOS become large enough for the corrections to vanish.

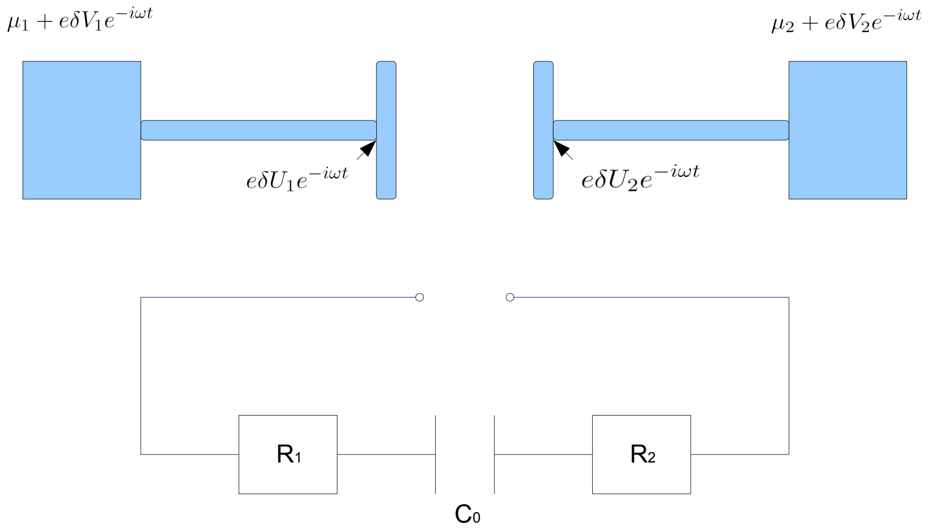

Figure 3.19: **Top:** Mesoscopic capacitor coupled to two reservoirs, where the oscillating outer potential changes $\delta V_1, \delta V_2$ introduce inner potentials changes $\delta U_1, \delta U_2$. **Bottom:** Macroscopic conductor described by three separate elements: dc resistances R_1, R_2 and an electrostatic capacitance C_0.

The electrochemical capacitance $C(\omega)$ of a mesoscopic conductor as shown in Fig. 3.19 is a thermodynamic quantity describing the system as a whole, in contrast to the parameters C_0, R_1 and R_2 of a macroscopic capacitor which are separate descriptions of the system constituents [80]. The quantum capacitance correction is a consequence of the Pauli principle, which needs an extra energy dependence in order to fill the limited space in a mesoscopic capacitor with electrons [77]. An applied electric field can not be screened completely, and the injected charge is stored inside the respective plate over a screening length penetrating it. This means that in contrast to a macroscopic conductor, the capacitively induced charges are not staying only at the surface. The $\delta U_1, \delta U_2$ depicted in Fig. 3.19 represent an average change of the inner potential in the respective plate and cannot be derived directly from the outer potential change $\delta V_1, \delta V_2$ [80].

It is not at all clear how the geometrical capacitance C_0 behaves exactly when the system parameters are changed. There is no such thing as a *plate* in our description, but rather single surface atoms with strong border effects, rendering it unlikely that the simple $C_0 \approx \frac{A}{d}$ (with A being the surface area and d the distance between the plates) is an approximation of any usefulness. However, qualitatively, an increased surface area or decreased distance should still result in higher capacitance. It was already shown in Fig. 3.10 that a larger distance between the plates increases the capacitance according to Eq. 3.10, as expected.

It is now crucial that this is not true for the linearized approach according to Eq. 3.16, since there is a one-to-one correspondence between the description of the displacement current in this formula (the third line) and the GDOS defined above. For a symmetrical system in which only the displacement part is non-zero, the capacitance becomes (according to 3.17 and 3.19) simply

$$\frac{1}{C(\omega)} = \frac{2}{D(\omega)} \tag{3.20}$$

with $D(\omega) = D_I(\omega) = D_{II}(\omega)$. Comparison to Eq. 3.18 reveals that no geometrical capacitance C_0 is taken into account. The linearized approach is therefore independent of the distance between the plates, offering an explanation for the large deviations still present in Fig. 3.13 which suggest a lower capacitance in the tranDFTB result. If only the surface area of the systems is increased, Eq. 3.16 will still yield a higher capacitance though, as the GDOS also becomes larger. To demonstrate this, a system with a broader surface area (see Fig. 3.20) has been calculated.

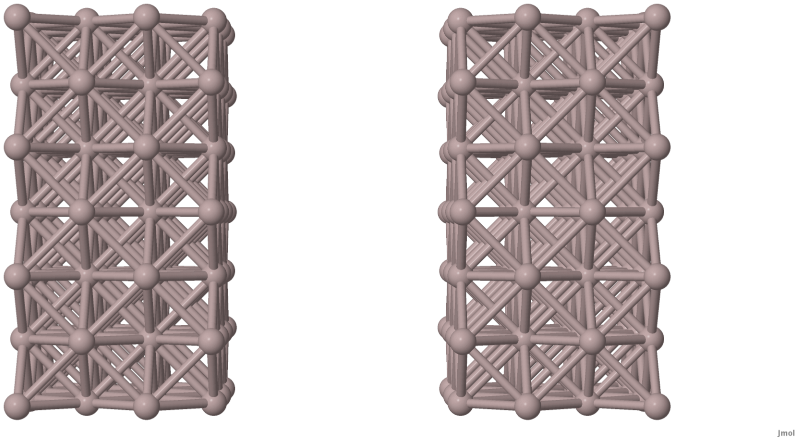

Figure 3.20: Aluminum capacitor with the same plate distance and surface orientations as the Al-1,4-benzenediol-Al test system - (100) along the transport direction - but with a larger surface area. The device region consists of 196 atoms in total.

The results can be seen in Fig. 3.21. Again, the admittance shows the expected behavior of a quadratically increasing dynamic conductance with a steeper slope for the larger surface area, and a steeper linear decrease of the dynamic susceptance. The surface area is larger by a factor of 9 and the corresponding change in the admittance near $\omega = 0$ is roughly a factor of 4, as can most easily be seen when looking at the imaginary part of the admittance. Since $C_0 \approx \frac{A}{d}$ is only a rough approximation in this case due to the finite plates and the quantum part of the capacitance is also changing slightly, quantitative deviations are expected. Still, the qualitative change of the capacitance is captured correctly within our approach.

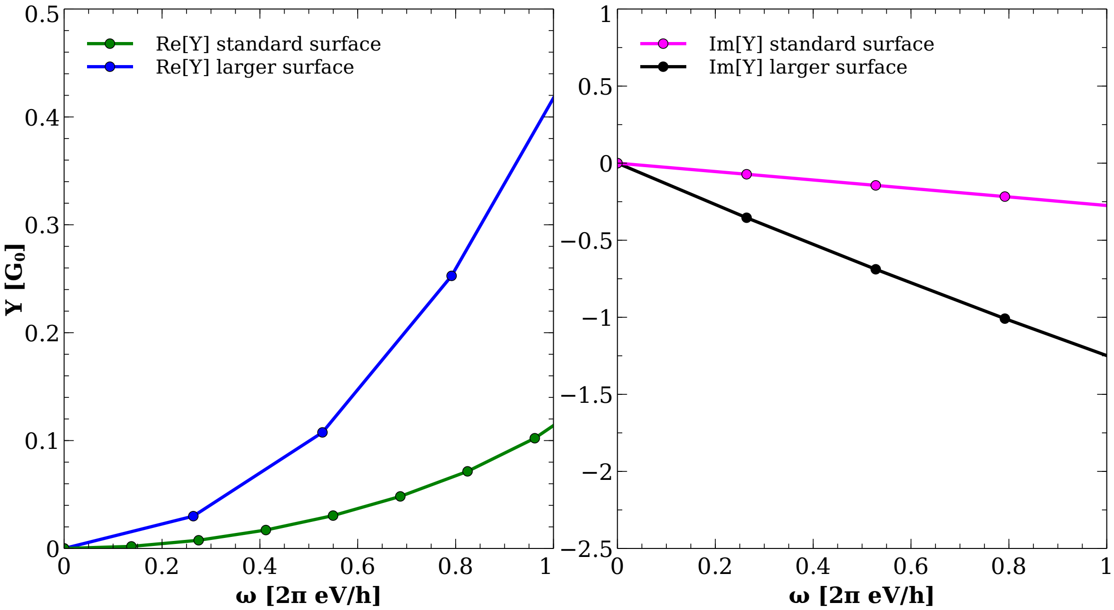

Figure 3.21: Capacitor resulting from omitting the molecule in the Al-1,4-benzenediol-Al system compared to a capacitor with a larger surface area ($A_1 \approx 16\text{Å}^2$ to $A_2 \approx 147\text{Å}^2$). **Left**: real part of the admittance. **Right**: imaginary part of the admittance.

3.6. Negative capacitance

As a side note, we will briefly discuss the occurrence of negative capacitances which were reported in the literature [81] for high frequencies. The lattice constant of the capacitors used in the previous section is $g_1 = 4.05\text{Å}$. By increasing it, we are essentially changing the coupling between the lead atoms and the entries of the self energy matrix become smaller. Fig. 3.22 shows that the capacitance stays largely constant for the first 1-2 eV and becomes negative at high frequencies.

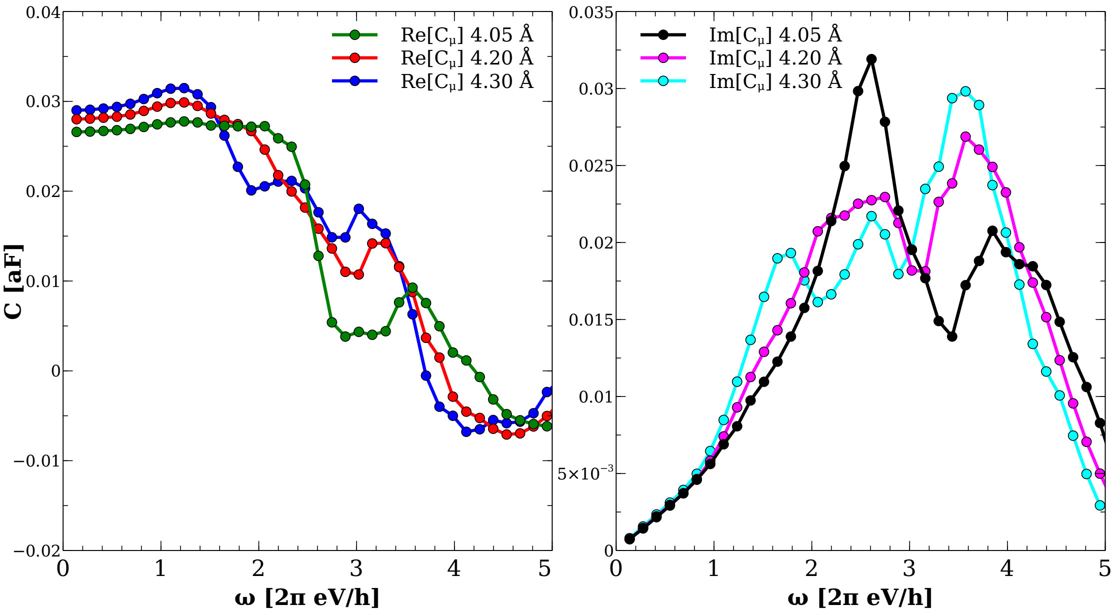

Figure 3.22: Frequency-dependent capacitance for different aluminum lattice constants, and thus different coupling. The experimental, previously used lattice constant is 4.05Å. **Left**: real part of the capacitance. **Right**: imaginary part of the capacitance.

The critical frequency at which the sign of the capacitance changes decreases systematically with smaller coupling Γ. This behavior has also been reported in Ref. [81] who used a quantum dot contact with a single channel plate. They interpreted the negative capacitances with the charge buildup not being able to follow the bias; the determining quantity for the critical frequency is thought to be the RC time $\tau_{RC} = RC$, which is considerably smaller in our systems and therefore, the corresponding frequency is much larger. We can therefore confirm the trends observed in the above publication. Note that the capacitance for small frequencies is slightly increasing with larger lattice constants, since the surface area is also becoming larger.

3.7. Short summary

The admittance properties of capacitive and inductive systems were analyzed, the respective identification of the system type is possible by looking at the dc transmission near the Fermi energy. Other than that, the dc transmission of the junction does not contain the information needed to construct the admittance curve, since the latter is dominated by displacement currents in the lead material. The qualitative shape of said curves is in line with a single level model employed for comparison. We also compare our results to multi level approaches in the frequency domain which do not take into account the device ac potential. We observe a very significant dependence of the admittance curve on the potential distribution for capacitive systems, and much less so for inductive systems. The large disagreement for capacitive systems is attributed to the non-flat potential distribution invalidating assumptions of the frequency domain method. In inductive systems, the approaches initially agree due to the flat potential across the device. Higher frequencies then render the initially inductive system resistive and therefore, disagreements appear. However, even when switching off the ac potential update, quantitative differences between the approaches remain and are explained by the neglection of the geometrical capacitance by the frequency domain approach. Our method yields qualitatively correct and largely expected results throughout, including the confirmation of negative capacitances which are briefly touched.

Chapter 4

Photon-assisted tunneling and higher harmonics

4.1. Introduction

Having investigated the full ac response for small voltages, we now look into rectification processes which are also called photon-assisted tunneling (PAT). Applying radiation of a fixed frequency to an atomic or molecular junction generally leads to the development of not only an oscillating ac current, but also modifies already existing dc currents flowing through the system. Even if no bias has been applied in the absence of the external radiation, asymmetries in the junction allow for the rectification to a dc current which is frequently labeled *photocurrent* indicating that it was exclusively induced by PAT processes [7, 82, 83]. The occurrence of PAT is well documented in the experimental literature and is found to be dominant over other light-induced transport mechanisms especially in the microwave regime and for lower frequencies [84], but depending on the junction also in the optical regime we are investigating. Apart from probing over which frequency range a certain transport mechanism is dominating for a specific system, the measurement of rectification processes gives indirect access to estimations for local field enhancement by surface plasmons. Corresponding experiments have been conducted recently using frequencies in the optical regime [85, 86].

The standard approach to PAT was introduced by Tien and Gordon [9, 87] and will be outlined in the following. Whereas this heuristic Tien-Gordon description does work well when compared with some experiments [85], the optically induced voltage oscillation V_{ac} is usually treated as a free fitting parameter as it is hard to be accessed otherwise. Furthermore, the agreement has only been reported for a limited voltage and frequency range, if the conductance does not change a lot due to radiation, and for certain systems like suspended wires. Consequently, there is room for a more sophisticated description of PAT. Our method provides significant improvements by taking into account the precise form of the time-dependent potential within the device region by self-consistent calculations. In the following, the results from both approaches will be compared.

4.2. Basics, Tien-Gordon approach

From the theoretical side, external radiation is usually modeled by an adiabatic oscillating shift of the lead potential(s). This is also the description in our approach, in which the Hamiltonian does not couple directly to the external field and therefore no true electron-photon interaction is described. It is in general unknown how the induced amplitude within the leads is connected to the external amplitude, and experimentally it is, as mentioned, usually treated as a free parameter fitted to theoretical models. The frequency of the induced field is assumed to be the same as outside, and the approaches are valid up to the plasma frequency of the respective lead material. Also note that when modelling interaction with light in this particular way, it implies that only the leads are hit by the photons.

In this spirit, the input voltage signal for our code describing the effects of external radiation looks like

$$V(t) = V_{dc}(1 - e^{-\frac{t}{t_0}}) + V_{ac} \sin \omega t \tag{4.1}$$

where the ac voltages will reach considerably beyond linear response. The initial exponential dampening of the dc voltage is for numerical reasons only; a sudden step-like raise at t=0 would lead to issues with the propagation. In order to obtain the presented results, one extracts information from the current signal after the initial effects of the switching-on wore off. The input signal used is therefore the same $V(t) = V_{dc} + V_{ac} \sin \omega t$ also discussed in the theoretical descriptions to follow. An example input and output can be seen in Fig. 4.1. How precisely monochromatic laser light in a real system is converted into an ac voltage within the leads depends on the system in question and is usually unknown. It can be extracted in cases where PAT is the only dominant transport mechanism by measuring the second derivative of the dc current with respect to an also applied dc voltage together with the rectified current (see [87] and the discussion about higher harmonics below). Note that the enhancement of the ac amplitude in the current is so large that the dc component can no longer be seen with the bare eye, since the test system used is capacitive as discussed earlier in the context of the dynamic admittance. It is important to keep in mind that the models presented below describe only the time-averaged current $\overline{I(t)}$ and not the full $I(t)$ response. Especially at high frequencies, the time-averaged current is much more accessible experimentally than the time-resolved ac current trace.

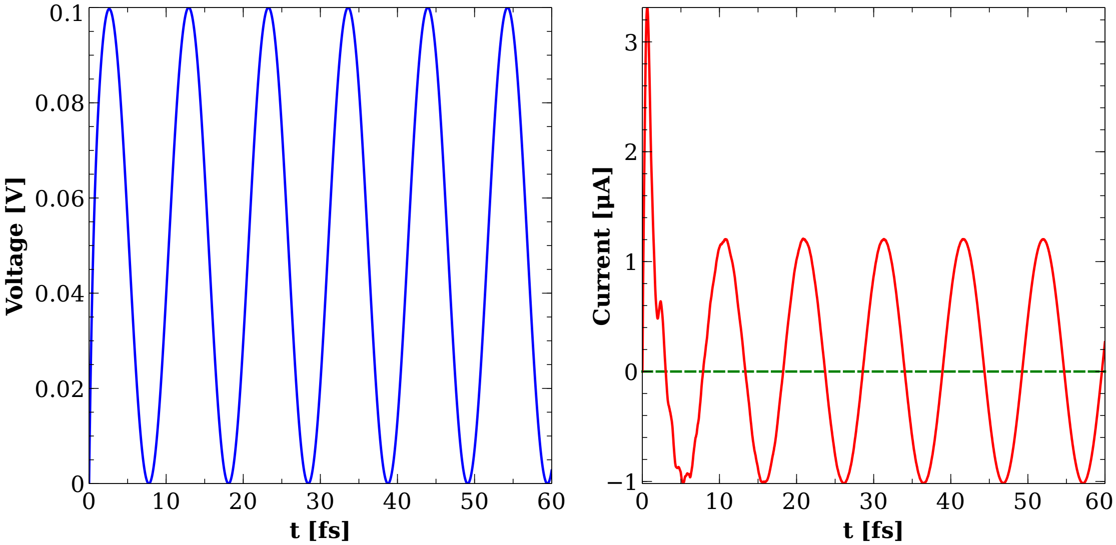

Figure 4.1: **Left:** Example input voltage signal for the Al-1,4-benzenediol-Al test system. $V_{dc} = 0.05$ V, $V_{ac} = 0.05$ V, $t_0 = 0.5$ fs, $\Delta t = 0.003$ fs, $t_{tot} = 60$ fs, $\hbar\omega = 0.4$ eV. **Right:** current response to the respective input signal.

When comparing with experiments, there are a number of transport mechanisms our approach does not capture. Since our Hamiltonian does not couple to external fields, there can be no intra-molecular transitions which might play a larger role in molecular systems at frequencies reaching into the optical regime. We also neglect temperature dependencies of any kind as well as the influence of the electrical fields on the geometry. Therefore we will not be able to describe thermoelectric currents which - for example - can originate from thermal expansion of the junction and the accompanying structural changes which influence bonding distances [7].

Besides the NEGF formalism, light-induced or light-enhanced transport can be described in a variety of approaches including Floquet theory and the scattering formalism (for a comprehensive review, see [84]). Recently, a sophisticated, gauge-invariant description of the problem to find the time-averaged (i.e. the rectified dc) current was derived in the framework of NEGF [88, 89] starting at Eq. 3.11 and using the assumption that the ac potential in the device region is of a simple, constant profile. Since this approach is still numerically very demanding, it has rarely been put to use in molecular systems without significant approximations. First, the wide band limit (which assumes the energyindependence of the lead self-energy) is employed. When applied to a single time-dependent resonant level, given small V_{ac}, ω and couplings to the leads of proportional strength, the approach then reduces to an expression for the dc current very similar to the heuristic formulation that was suggested over 50 years ago by Tien and Gordon. The deeper connection why the Tien-Gordon-result looks formally equal to the mentioned single level model is yet unknown [90]. Still, the similarities to the NEGF result add justification, and it yields good qualitative results in some cases when staying in the linear response and low frequency regime [9, 87]. The Tien-Gordon expression reads

$$\bar{I}(V_{dc}, V_{ac}, \omega) = 2 \sum_{l=-\infty}^{\infty} \left[J_l \left(\frac{V_{ac}}{2\omega} \right) \right]^2 \int dE \, T(E + l\omega)[f_L(E, V_{dc}) - f_R(E, V_{dc})] \tag{4.2}$$

which is fully determined by quantities that can be calculated without taking into account any external radiation. The usual dc Landauer transmission $T(E)$ carries the information where "photons" of energy $\hbar\omega$ are able to find transmission channels to contribute to the current, and the respective harmonics are weighted by the Bessel function of first order $J_l\left(\frac{V_{ac}}{2\omega}\right)$, strongly suppressing higher orders of inelastic scattering. We again stress that this equation is only expected to give good results for small V_{ac} and also for small frequency ω, which suggests that our approach valid for very high frequencies beyond linear response can offer significant improvements: we can account for the shortcomings of the Tien-Gordon-approach in the description of screening effects and phase shifts within the device. A visualization of the concept behind Eq. 4.2 can be found in Fig. 4.2 below.

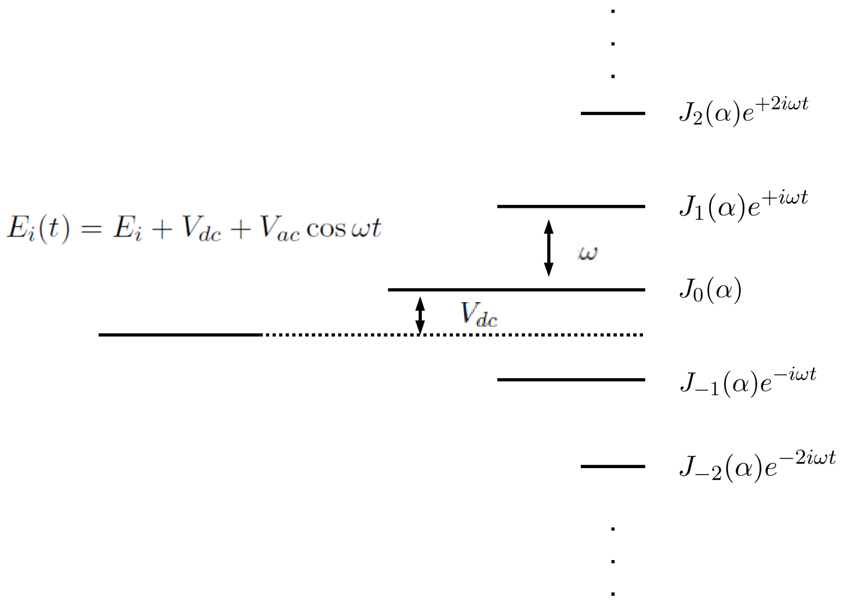

Figure 4.2: Visualization of the PAT concept in the Tien-Gordon picture. An unbiased level is shifted by the dc voltage and photon sidebands are opened up by the external radiation. They are weighted by Bessel functions of first order with $\alpha = \frac{V_{ac}}{\omega}$. Picture reproduced from Ref. [1].

4.3. PAT in symmetric junctions

In order to treat both approaches on equal footing, the transmission needed for the Tien-Gordon expression is obtained from the steady state NEGF calculation in our code. The charge-corrected device Hamiltonian and the self-energies are identical to the ones used for the initial conditions in the time propagation, which yields the presented PAT results and is calculated in the usual TD-DFTB framework with the PBE functional. For now, we are looking at the conductance only, for which a simple form can be obtained easily from Eq. 4.2:

$$G(V_{ac}, \omega) = G_0 \sum_{l=-\infty}^{\infty} \left[J_l \left(\frac{V_{ac}}{2\omega} \right) \right]^2 T(E_F + l\omega) \tag{4.3}$$

As earlier calculations have shown, the Al-1,4-benzenediol-Al test system stays in linear response for dc voltages up to $|V| = 0.1$ V. We choose $V_{dc} = 0.05$

V and investigate the frequency-dependent rectification for various finite ac voltages beyond linear response. All data presented has been obtained with a total evolution time of $t_{tot} = 60$ fs and a time step of $\Delta t = 0.003$ fs. As soon as the effects of the switching-on wore off, we extract a number of full periods depending on the frequency and calculate the time-average. Since the Tien-Gordon description becomes very unreliable for larger voltages as the precise shape of the induced ac potential becomes more and more important and a direct comparison is no longer meaningful, we will limit ourselves to the voltage range of [0:2.5V] for now.

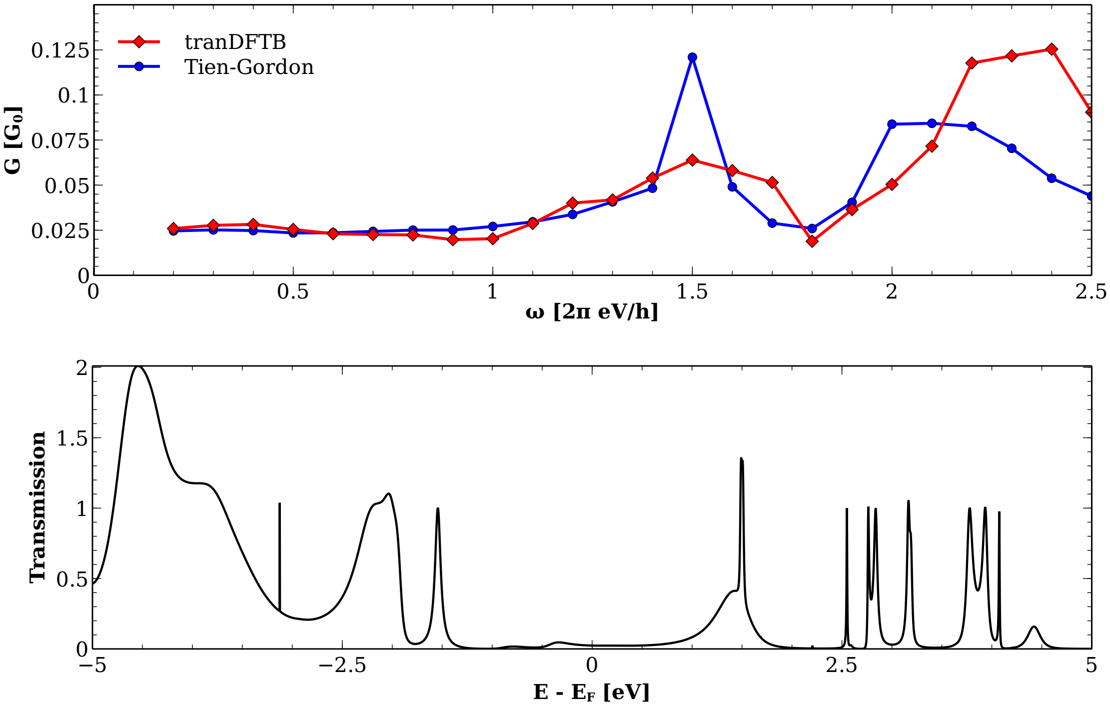

Figure 4.3: **Top:** Comparison between the results for the conductance obtained from tranDFTB and the Tien-Gordon approach using constant $\alpha = \frac{V_{ac}}{\omega} = 0.5$. The system is again Al-1,4-benzenediol-Al, the TD simulation parameters are $V_{dc} = 0.05V$, $\Delta t = 0.003$ fs, $t_{tot} = 60$ fs. **Bottom:** transmission of the system at V=0 calculated in tranDFTB.

In the literature, Tien-Gordon calculations are usually parametrized by a constant $\alpha = \frac{V_{ac}}{\omega}$ which means that the weighting of the various harmonics stays the same as frequency and ac voltage are both increased alongside. In Fig. 4.3 we plot our results for the rectified conductance together with the ones obtained from Tien-Gordon approach for constant $\alpha = 0.5$. This translates into a dc channel weighted by 88 % and a branching of roughly 6 % for processes absorbing or emitting a "‘photon"’ at the energies $E - E_F \pm \hbar\omega$, respectively. Higher orders are strongly suppressed for this value of α. Significant deviations from the dc conductance in the absence of radiation appear once the energy of these absorption or emission processes matches a transmission channel of a molecular resonance. For the Tien-Gordon approach, the position and broadening of these channels is given by the dc transmission. If one wants to keep the picture of electrons tunnelling at modified energies through a transmission, its shape is significantly altered within our approach.

In the case of Al-1,4-benzenediol-Al, it appears that we capture similar qualitative features as the Tien-Gordon theory, but the effect of the resonance at $|\hbar\omega| = 1.5$ eV is not as pronounced. Further analyzing these deviations, in Fig. 4.4 we fix the frequency at the large peak with the energy $\hbar\omega = 1.5$ eV and again compare the prediction for the conductance of the two approaches. The larger V_{ac} is chosen and thus the more we are leaving the ac voltage range in which the Tien-Gordon approach is a good approximation, the more the two descriptions disagree. Our results show more structure in comparison to the smooth and steady increase of conductance seen in the Tien-Gordon approach. The lower part of Fig. 4.4 shows how all absorption and emission channels are strongly suppressed in both approaches if the induced ac voltage is considerably smaller than the induced "‘photon"’ energy.

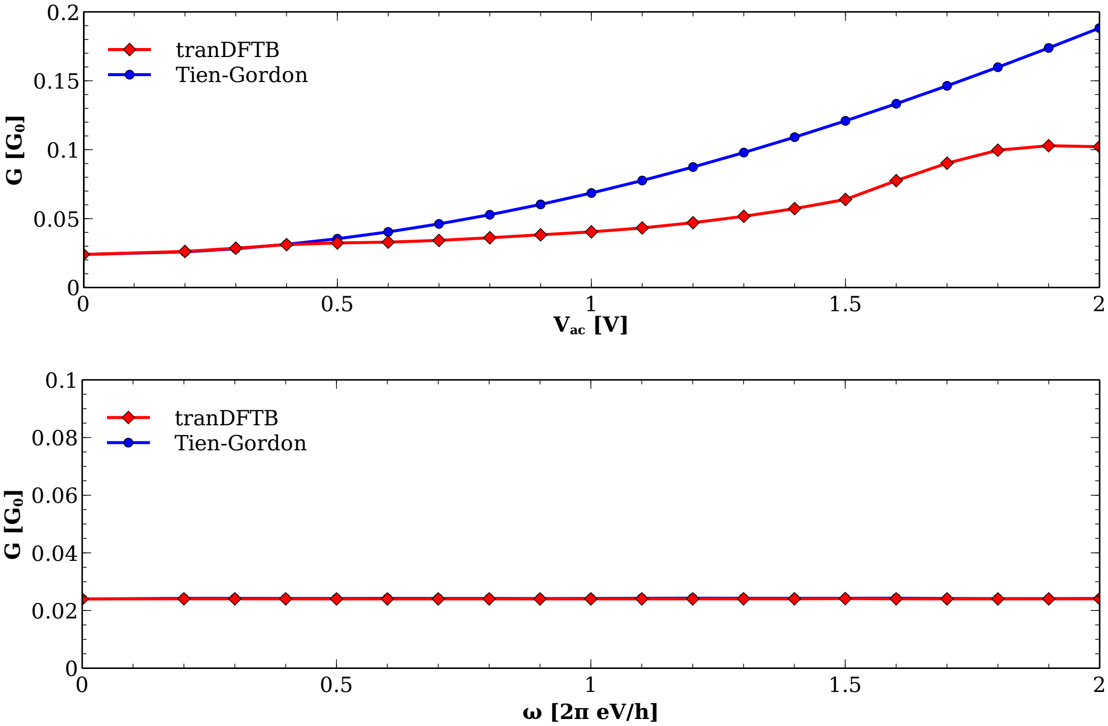

Figure 4.4: **Top:** Fixing the frequency of the induced oscillation to $\hbar\omega = 1.5$ eV which corresponds to the large resonance in Fig. 4.3, the amplitude of the ac voltage is varied to analyze the difference between the two approaches. The system and the other simulation parameters remain unchanged. **Bottom:** If the ac voltage is now fixed to $V_{ac} = 50$ mV, both approaches predict highly suppressed absorption and emission in the investigated frequency regime, the conductance stays at its dc value of roughly 0.024 G$_0$.

The main difference between the two approaches is the treatment of the potential in the device region. For the Tien-Gordon formula derived from NEGF, the total potential V_D (in tight-binding form of [88]) is assumed to look like

$$[V_D(t)]_{\mu\nu} = [S_D]_{\mu\nu}\frac{1}{2}[U_\mu(t) + U_\nu(t)] \tag{4.4}$$

$$U_\mu(t) = U_\mu^{dc} + U_\mu^{ac}\cos(\omega t) \tag{4.5}$$

where S_D is the overlap matrix in the device region and U_μ denote atomic potentials that are assumed to be identical for each orbital i in the same atom. U_μ^{dc} may now be included into the device Hamiltonian [88], therefore the main issue is the choice of U_μ^{ac}. It has to be fixed to simple forms in order to arrive at a tractable equation like 4.2, in this case a symmetrical voltage drop at the interfaces and zero ac potential inbetween them, i.e.

$$U_{\mu}^{ac} = \frac{U_L^{ac} + U_R^{ac}}{2} \tag{4.6}$$

with U_L^{ac} and U_R^{ac} denoting the potentials induced by the ac voltage in the respective leads. Although it has been claimed that the ac potential profile does not play a central role [88, 89], this conclusion was reached by comparing different simple shapes for U_{μ}^{ac}, like the mentioned drop only at the contact-device interfaces or a linear interpolation within the central region. Looking at Fig. 3.16, the potential distribution of a system with lead material in the device region is not necessarily linear. More importantly, the different potential profiles were only tested for very small voltages. We can therefore still expect sizeable improvements by calculating the potential self-consistently.

In Fig. 4.5 we show how the two approaches compare if we choose a large ac frequency of $V_{ac} = 1.5$ V throughout. The frequencies smaller than $\hbar\omega = 1.5$ eV are now combined with a larger ac voltage than in 4.3 and we observe that the qualitative agreement is worsening. A higher voltage/frequency-ratio means that the weight of absorption and emission processes is increased.

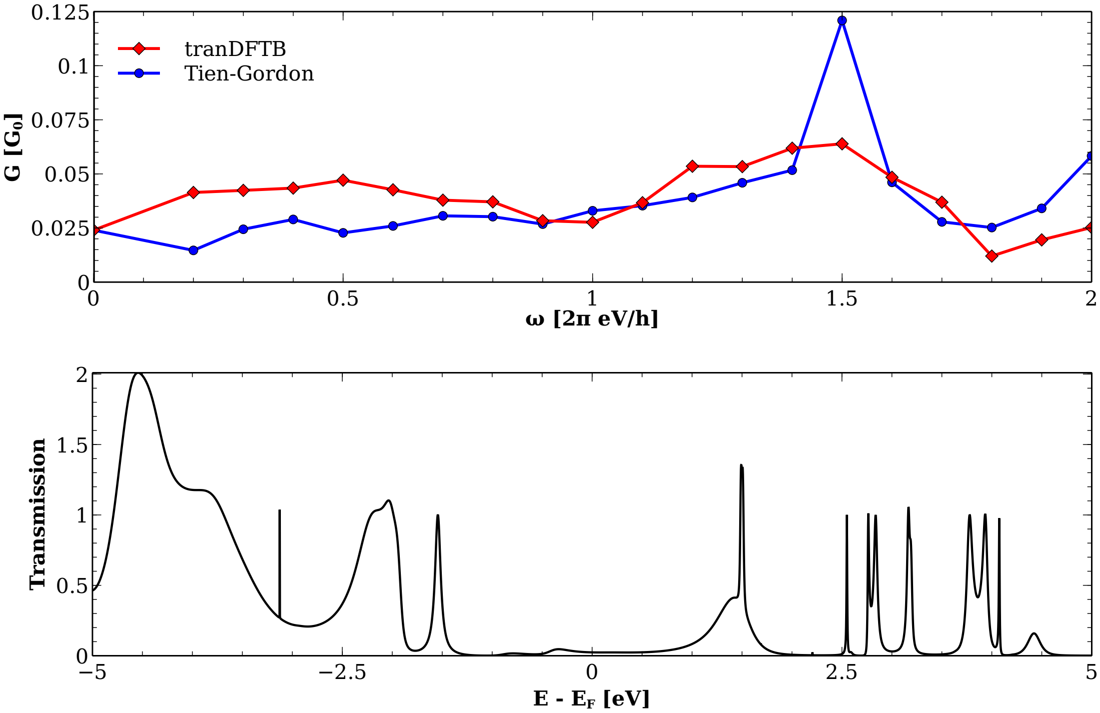

Figure 4.5: **Top:** The comparison of Fig. 4.3 for a fixed large ac voltage of V_{ac} = 1.5 V. The disagreements for lower frequencies increase significantly. **Bottom:** transmission of the system at V=0 calculated in tranDFTB.

When connecting the benzene molecule not to aluminum leads, but to carbon chains, the transmission is smoothed out due to the reduced number of highly transmitting channels. In consequence, also the rectification predictions in both approaches become smoothed out curves, as one can see in Fig. 4.6. This supports that in our method, the structure of the dc steady state transmission also seems to have an effect on the rectification properties, but as it turns out in the following, there is no one-to-one correspondence. The shape of the resonance at $E - E_F = 5$ eV cannot fully be captured since shortly above that energy value, the current becomes irregular due to numerical instabilities.

Also included within Fig. 4.6 is a plot in which the frequency is fixed at the position of the first larger resonances in the transmission, i.e. $\hbar\omega = 2.5$. Again, if one now changes V_{ac}, also α is varied, thereby increasing or decreasing the relative weight of emission and absorption processes.

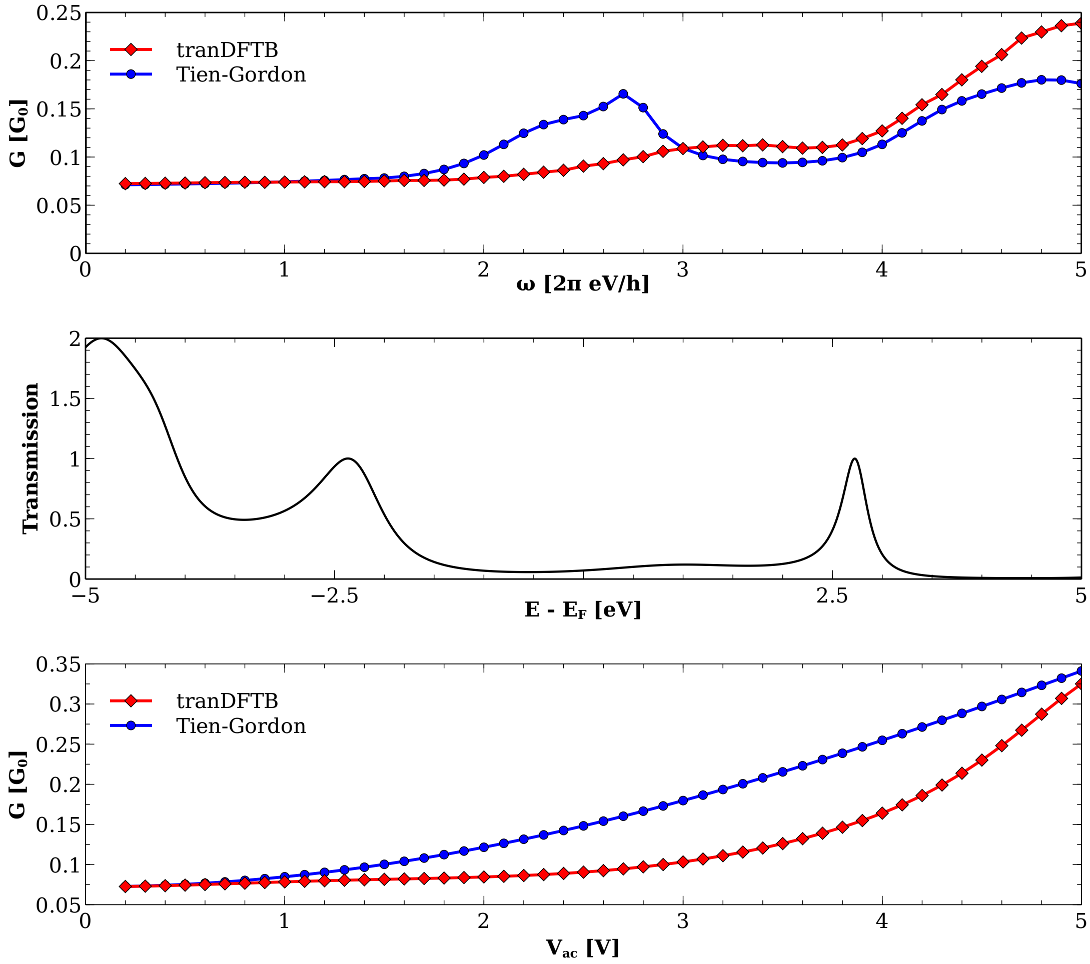

Figure 4.6: **Top:** Comparison using $\alpha = 0.5$ for 1,4-benzenediol coupled to carbon chains with an interatomic distance of 1.1 Å. The simulation parameters are the same as before. **Center:** Transmission of the system at V=0 calculated in tranDFTB. **Bottom:** Comparison at fixed frequency of $\hbar\omega = 2.5$ eV.

For the other systems we investigated, the results of our approach almost seem unrelated to the prediction by Tien-Gordon. For an octene molecule coupled to aluminum leads, we had to plot the results of the two approaches separately to make the structures comparable, since they strongly differ qualitatively and quantitatively, see Fig. 4.7. Closely following and examining the curves, one can see that the qualitative reaction on transmission features still agree in some of the cases, but at least quantitatively, there is no match. Given the limitations of the Tien-Gordon approach at high voltages and frequencies, this is understandable. The large deviations and proposed improvements are still surprising.

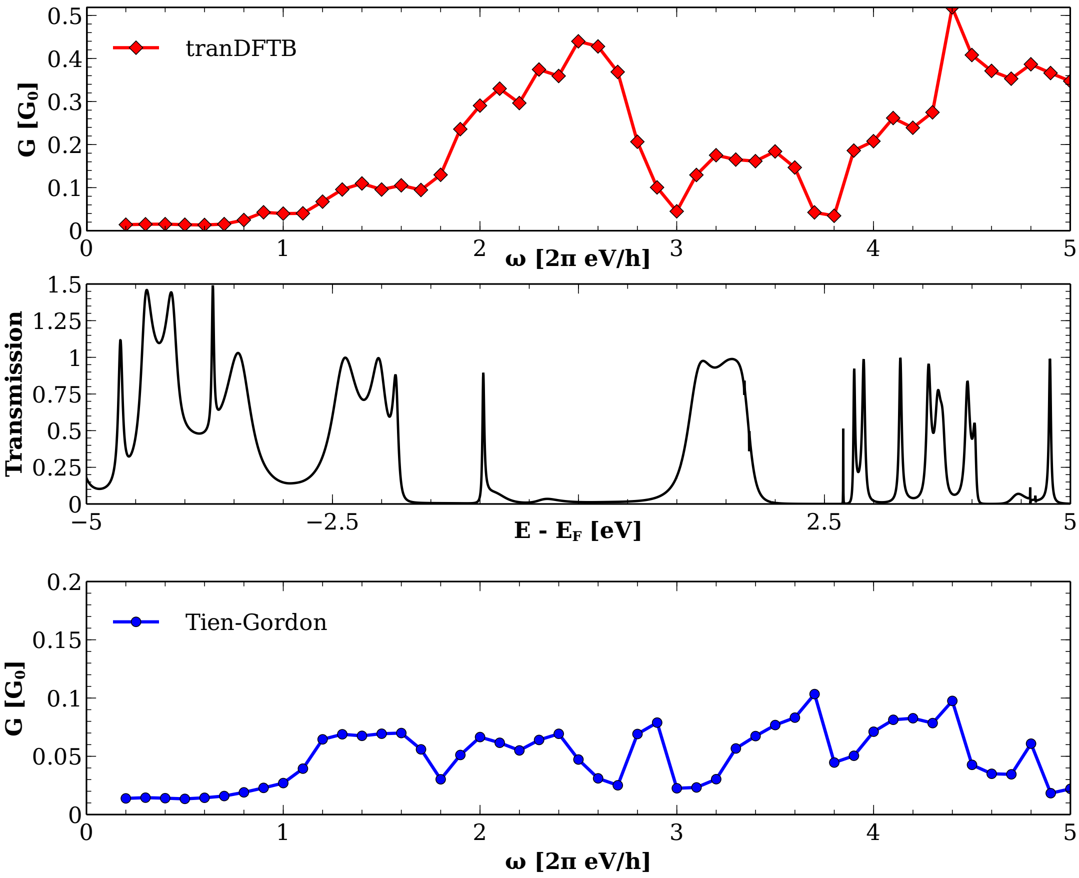

Figure 4.7: **Top:** tranDFTB result using $\alpha = 0.5$ for an octene molecule between aluminum leads. The simulation parameters are the same as before. **Center:** Transmission of the system at V=0 calculated in tranDFTB. **Bottom:** Corresponding Tien-Gordon result.

For a seven-membered carbon chain between aluminum leads, the disagreement becomes even stronger, see Fig. 4.8. There also seems to be no systematic explaining for which systems one can see an increased agreement. While this is clearly unsatisfying, there is also no apparent reason why the steady state transmission should be a valid approximation for the ac transmission at high voltages and frequencies. Since Tien-Gordon is still the prevalent theory in the literature, we have to present our corrections without further ways of validating them by comparison to other approaches.

As expected, a general statement true for all test systems is the increasing disagreement for voltages beyond linear response. While the Tien-Gordon approach is only valid for small voltages anyway, our time propagation may also run into numerical difficulties at voltages as high as 5V. While this regime is of course easy to reach on the computer, experimentally it makes not much sense to apply voltages that high onto a single molecule junction, as it will certainly be destroyed. We conclude that above linear response, the steady state transmission as used in the Tien-Gordon approach is not sufficient to predict the features of the frequency-dependent rectification, and the weight of the higher harmonics is much stronger than anticipated.

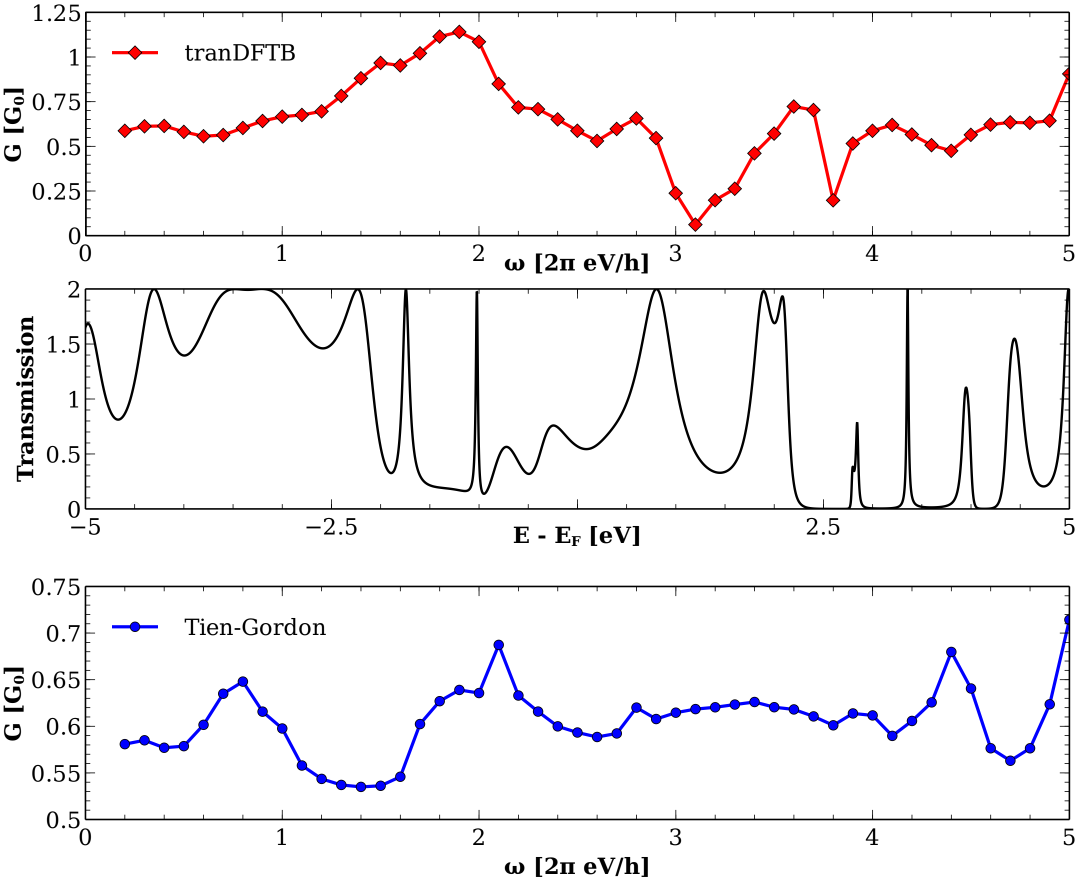

Figure 4.8: **Top:** tranDFTB result using $\alpha = 0.5$ for a seven-membered carbon chain between aluminum leads with an interatomic distance of 1.1 Å. The simulation parameters are the same as before. **Center:** Transmission of the system at V=0 calculated in tranDFTB. **Bottom:** Corresponding Tien-Gordon result.

4.4. Asymmetric junctions and photocurrent

What is left to discuss is rectification for vanishing dc bias, but asymmetric junctions, as mentioned in the introduction to this chapter. Pedersen and

Büttiker [91] pointed out that the Tien-Gordon result falsely predicts a rectified current completely independent of junction asymmetry, which they contribute to the lack of gauge invariance with respect to adding a constant potential. A symmetric junction can not exhibit a photocurrent by the basic symmetry argument that rectified currents flowing in two opposite directions have to cancel each other, i.e. $I_L = -I_R$. In the following we will show how our approach can account for this deficit.

Taking the usual Al-1,4-benzenediol-Al test system, we shifted the molecule by 0.1Å along the transport direction while the lead principal layers stay fixed, consequently there is an asymmetric coupling of the oxygen to the aluminum. The resulting current response signal is averaged over multiple full oscillation periods without including those that are visibly affected by the initial switch-on. Note that due to the finite time stepping in both voltage signal and current, we introduce an error by averaging, and there will be traces of the initial overshoot left in the signal even at later times. The rectified currents appearing are very small compared to the large ac current induced by the voltage of 1.5 V, leading to large relative error bars. That is the reason why in Fig. 4.9, also the fully symmetric system seems to show rectification. A sensitivity analysis showed that error bars of ±25 to ±30 nA are appropriate for the used time step of $\Delta t = 3$ attoseconds and total evolution time of $t_{tot} = 60$ fs, leaving the expected result of the photocurrent $I_{rect} = 0$ within the accuracy limits. The estimated error bars were obtained by observing the effect of omitting or adding one more data point in the current average.

Due to the sensitivity regarding the time step, the asymmetric data was repeated using a much shorter time step of $\Delta t = 0.5$ attoseconds with a total of 120.000 individual steps. Far outside the error bars of this expensive calculation, rectification occurs for the asymmetric junction.

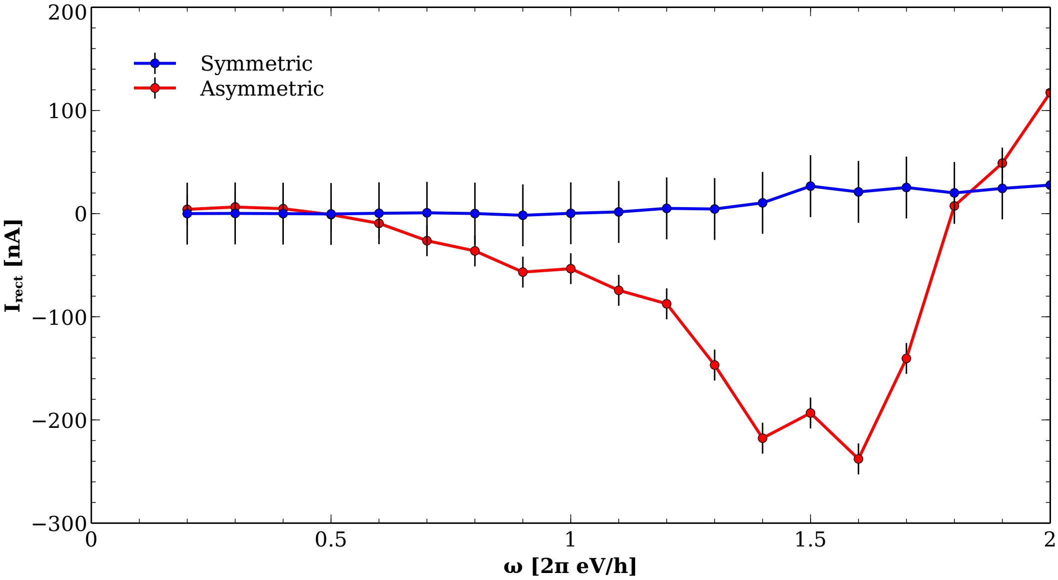

Figure 4.9: Rectified current (photocurrent) at $V_{dc} = 0$ with $V_{ac} = 1.5$V for a symmetric Al-1,4-benzenediol-Al junction and an asymmetric junction with the molecule displaced by 0.1Å along the transport direction

4.5. Higher harmonics and the quasi-static current approximation

In this section, we repeat the arguments given in the second part of our publication [92] about a closely related topic, the analysis of higher harmonics in the induced oscillating voltage and the corresponding current. Their appearance can be made obvious if one assumes that the current response to an ac bias of the form

$$V(t) = V_{dc} + V_{ac}\cos(\omega_0 t) \tag{4.7}$$

can be approximated by inserting the voltage into the current-voltage-characteristic without any external radiation, $I_{dc}(V_{dc})$, at each point in time. This would require the current to follow the voltage instantaneously and constitutes a quasi-static picture. The expansion

$$\begin{aligned} I(t) &\approx I_{dc}(V_{dc} + V_{ac}\cos(\omega_0 t)) \quad (4.8)\\ &= I_{dc}(V_{dc}) + \sum_{n=1}^{\infty} \frac{1}{n!}\frac{d^n I_{dc}}{dV^n}\Big|_{V_{dc}} (V_{ac}\cos(\omega_0 t))^n \quad (4.9) \end{aligned}$$

truncated after second order yields

$$I(t) \approx I_{dc}(V_{dc}) + \left.\frac{dI_{dc}}{dV}\right|_{V_{dc}} V_{ac}\cos(\omega_0 t) + \frac{1}{4}\left.\frac{d^2 I_{dc}}{dV^2}\right|_{V_{dc}} V_{ac}^2[1 - \cos(2\omega_0 t)] \qquad (4.10)$$

showing that for a non-linear current characteristic there are not only additional contributions to the zeroth order as found in the rectification calculations above, but also that the current signal will incorporate higher harmonics. As mentioned earlier, the induced oscillating ac field V_{ac} is usually unknown as it depends on screening and possible plasmonic excitations. By measuring the second derivative of the dc current with respect to the voltage as well as the rectified current, one can get an estimation of the induced field and can therefore also access the local field enhancement of the external voltage. [93, 94]

The question to ask is now under which circumstances the above approximation is good enough for this estimation to be reasonable. It appears to be a crude to assume that the current response can be obtained from the I-V-curve in absence of radiation and in full neglect of quantum effects like the absorption or emission of photonic quanta described by the Tien-Gordon approach of the last section. While for specific choices of systems (showing a flat transmission) or simulation parameters ($\alpha = \frac{V_{ac}}{\omega}$ small) the influence of these inelastic processes is indeed small, the ac current amplitude and the phase between current and voltage can change massively with frequency, as we saw in the chapter about dynamic admittance.

The truncation after second order in Eq. 4.10 requires a small V_{ac} and the non-linearities of I_{dc} around V_{dc} must not be too large. In molecular systems, I_{dc} will show strongly non-linear behavior when hitting molecular resonances. For weak bias, a larger gap positively influences the quality of this approximation, meaning that fully saturated compounds will be more likely to match the criteria than the molecular systems we are investigating.

In Fig. 4.10 one can see the phase difference between current and voltage by a plot of current and voltage for an irradiated junction. The current leads the voltage, indicating capacitive ac transport. As in Fig. 4.1, despite the voltage being positive at all times, the amplitude enhancement in the current is so large that it is changing signs. Also included in the picture is the sum of the currents through the left and right interfaces. A nonzero sum means charging and decharging of the device region which is properly accounted for in our code.

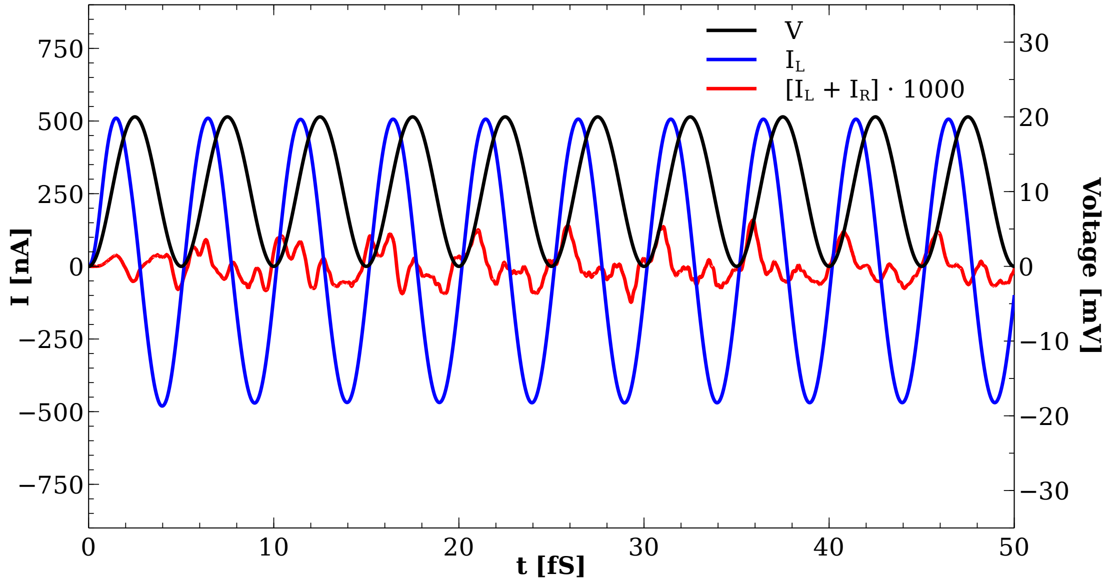

Figure 4.10: Depiction of current and voltage for $V_{dc} = -V_{ac} = 0.01$V after the initial switch-on effects have worn off, showing their phase shift as calculated by tranDFTB for the Al-1,4-benzenediol-Al test system. The smaller red curve is the sum of the currents through left and right interfaces enhanced by a factor of 1000. It indirectly shows the time-dependent charging of the device region.

The quality of the quasi-static approximation may now be tested by inserting $V(t)$ into the I-V-curve calculated by the static NEGF-Landauer module in our code and comparing it with the true time-dependent $I(t)$ including quantum effects and phase differences. First, Fig. 4.11 shows the I-V-curve, which is obtained by 80 individual static calculations and fitted with a high order polynomial, together with the resulting quasi-static current.

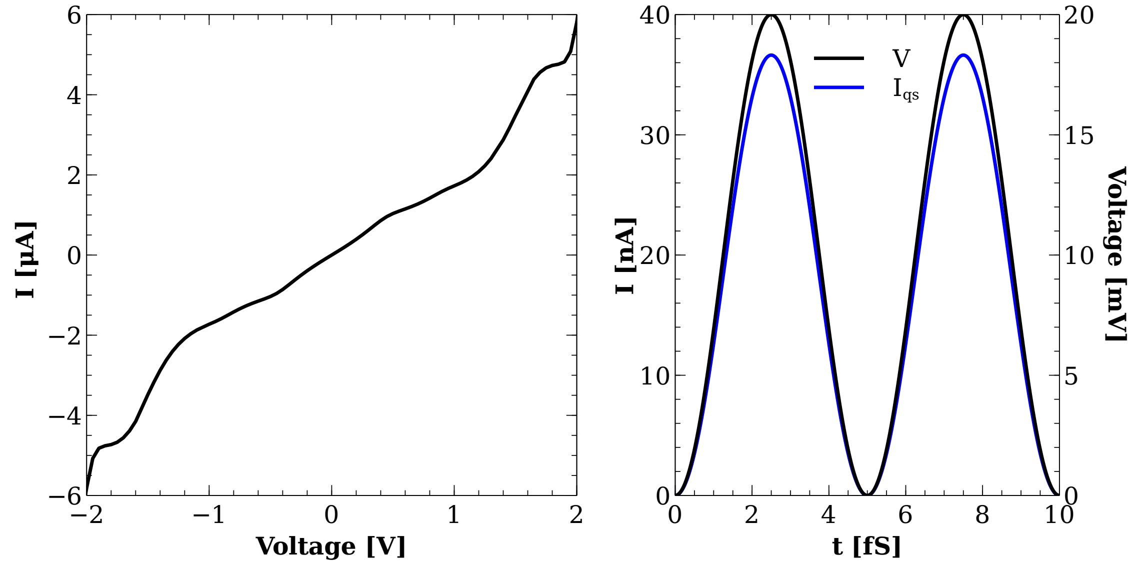

Figure 4.11: **Left:** Fitted I-V-curve $I_{dc}(V_{dc})$ from the static NEGF-Landauer module of tranDFTB obtained using the same Hamiltonian as the TD calculation. **Right:** Time-dependent external voltage $V(t)$ and the corresponding quasi-static approximation $I_{dc}(V(t))$ to the current.

It is in phase with the voltage inducing it and does have the same bias polarity at all times, in contradiction to the full TD current above. The I-V-curve shows a point symmetry at the origin due to the symmetry of the junction and stays roughly in linear response for up to $\pm 0.2V$. Strong non-linearities at around $2V$ are a consequence of the increased transmission due to the lowest unoccupied molecular orbital (LUMO) coming in range. By looking at the full quantum $I(t)$ curve in Fig. 4.10 one can see that its amplitude is larger by roughly a factor of 15 in comparison to the quasi-static current. About the same difference is also observed when increasing the voltage amplitude to $1V$, as can be seen in Fig. 4.12 which contains a plot of the current signal for an evolution time of 20 fs.

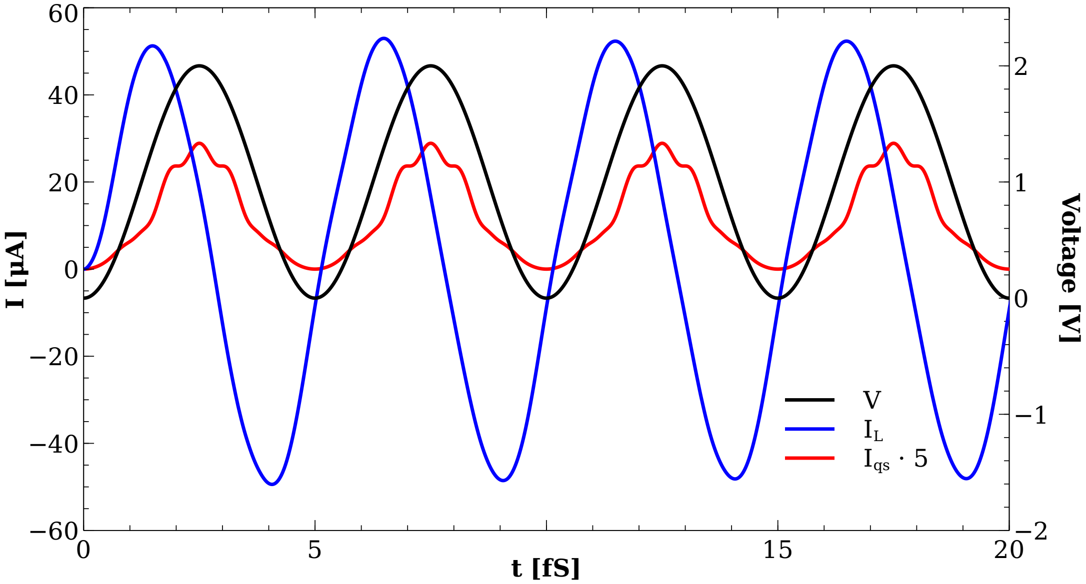

Figure 4.12: Comparison between the full TD current and the quasi-static approximation $I_{dc}(V(t))$ for a voltage amplitude of $V_{dc} = -V_{ac} = 1$V. The amplitude of the quasi-static current is much smaller (enhanced by a factor of 5 in the picture) and keeps the same polarity for the whole evaluation time.

In addition, the full $I(t)$ stays smooth at all times whereas the quasi-static current follows the I-V-profile and consequently makes the non-linearities induced by the molecular resonances clearly visible in the signal.

We now take a look at the higher harmonics by Fourier-transforming the current responses. Starting with the smaller voltage of 0.01V, Fig. 4.13 shows the full $I(t)$ and the quasi-static current in frequency space. The plots are in units of the frequency of the voltage oscillation ω_0. $I(t)$ exhibits no visible higher harmonics at this low voltage, while they can clearly be spotted for the quasi-static approximation, consequently overestimating the effect of non-linearities in the current already for low bias. The limit $\omega \to 0$ also gives access to the rectified current included in the signal. The change of the dc component $\frac{\overline{I(t)}-I_{dc}}{I_{d}c}$ is +0.8% for the quasi-static current and −1.1% for the full $I(t)$, revealing the importance of quantum effects.

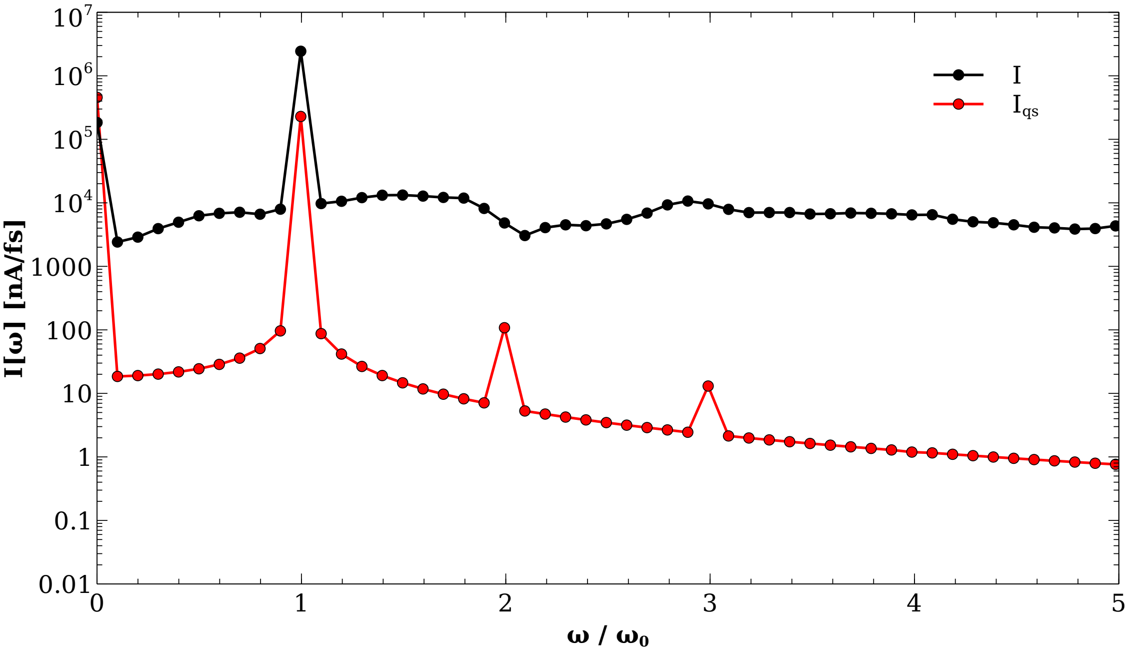

Figure 4.13: Fourier transforms $|I(\omega)|$ of the full quantum $I(t)$ and its quasi-static approximation for $V_{dc} = -V_{ac} = 0.01V$. The energy resolution is ≈0.08 eV with a total evolution time of 50 fs.

Increasing the voltage to $1V$ as plotted in Fig. 4.14 leads to more non-linearities in both signals as expected. The $I(\omega)$ of our full quantum simulation now shows higher harmonics which are clearly visible up to fifth order, while the quasi-static signal also includes higher orders in considerable amplitude. The rectification now leads to an increase of 60.8% in the dc component of the full $I(t)$ and 39.7% for the quasi-static approximation.

In both plots, it is striking that the full $I(t)$, while featuring fewer orders of higher harmonics, shows also higher amplitudes. Furthermore, the peaks are not as distinct as for the quasi-static current since they do not fall off as much between the multiples of ω_0. We suspect that this is a remnant effect of the transients induced by the initial voltage raise during the switch-on process.

Concluding, one can see decisive differences between a full atomistic quantum simulation and the classical quasi-static approximation. The amplitude of the current response in time and frequency space, the smoothness of the signal as well as the number of higher harmonics disagree significantly even for voltages as low as 0.01V. The quality of the quasi-static approach increases if the transmission is flat in the energy regime of interest, as the I-V-curve will show weaker non-linearities. However, when analyzing molecular systems irradiated by light which induces oscillating lead potentials with a frequency in the microwave or optical regime, the structure of the molecular transmission will show too extensive non-linear features for the approximation to hold. Consequently, the estimation of the rectified current by measuring $\frac{d^2I}{dV^2}$ becomes unreliable quickly when investigating molecular junctions. In contrast, it is possible to make theoretical predictions about rectification from full atomistic quantum simulations like established in our method.

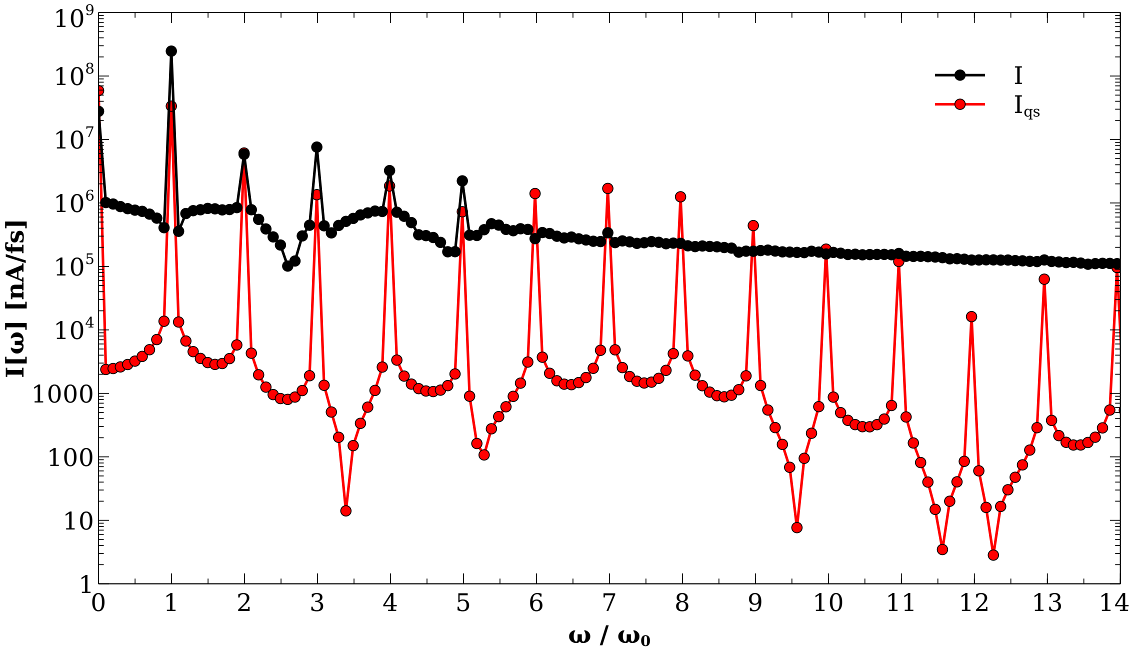

Figure 4.14: Fourier transforms $|I(\omega)|$ of the full quantum $I(t)$ and its quasi-static approximation for $V_{dc} = -V_{ac} = 1$V. The energy resolution is ≈0.08 eV with a total evolution time of 50 fs.

4.6. Short summary

We present the application of our time-resolved transport approach to photon-assisted tunnelling. We observe strong qualitative and quantitative disagreements with the established description of PAT introduced by Tien and Gordon. This is to be expected, since our approach calculates the ac potential within the device self-consistently, can therefore account for screening and charge accumulation, and is valid for arbitrary voltages and frequencies. In consequence, we offer a prediction for experiments in the high frequency regime and improve on the inherently limited description of Tien and Gordon. We also show that our approach correctly predicts photocurrents ($V_{dc} = 0$) to be dependent on junction symmetry and vanish in the case of symmetric junctions - in contrast to the Tien-Gordon picture.

It is also discussed that a quasi-static approach to the current response is in general an insufficient approximation, especially in the case of molecular systems in which the transmission is not flat. Even within linear response, the number of higher harmonics, the rectified current and the smoothness of the signal differs significantly from the full atomistic quantum simulations we employ.

Chapter 5

Time-independent transport through flexible adsorbed molecules

5.1. Introduction

During the early stages of this work, we were approached to help analyzing an experimentally observed phenomenon which appeared when lifting a large, flexible molecule off a copper surface using a scanning tunnelling microscope (STM) tip. Understanding how molecules with significant conformational flexibility change their electrical properties when subjected to forces is of major interest, since it may be possible to find structures in which the conductance can be modified by external forces in a way that molecular switches are feasible.

Specifically, the molecule 1,4-Bis(Pyridin-4-ylEthynyl)Benzene (BPEB) is adsorbed on a copper surface and pulled up by the STM tip, also made of copper. Judging by the frequency shifts during the atomic force microscopy (AFM), the molecule undergoes plastic and elastic deformations. Most likely connected to these deformations are changes in the conductance, which features characteristic jumps (see Fig. 5.1). At position A, a stable and conducting bond between the surface and the molecule is believed to have formed. Since during retraction, the conductance is not decreasing with the same exponential distance dependence as within the approach, the molecule is thought to bridge the tip and the surface and being pulled up. Strong changes in the conductance (one order of magnitude) are observed at position B and C which can also be reproduced in similar molecules.

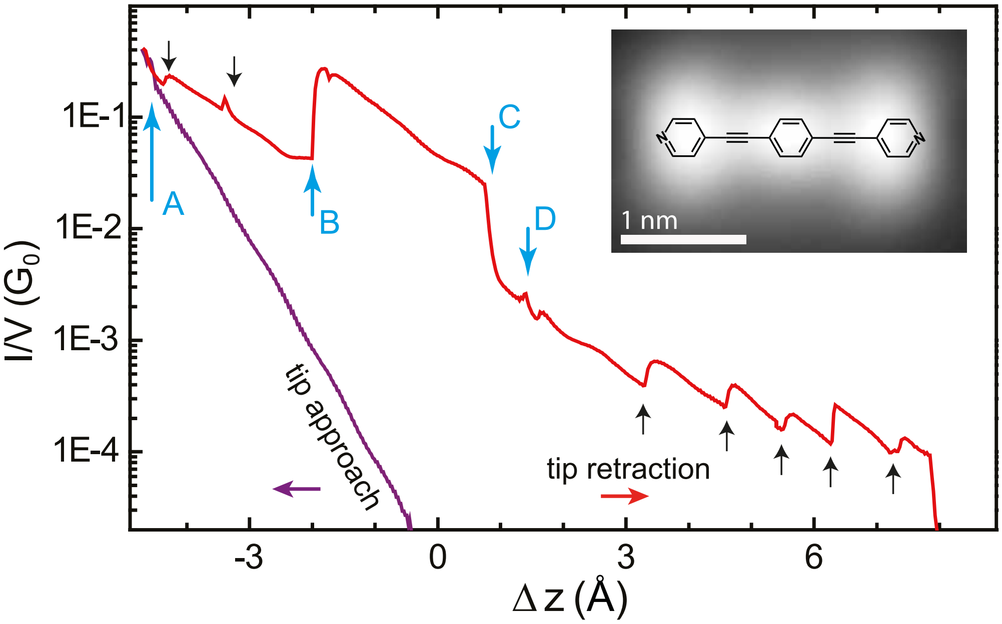

Figure 5.1: The linear conductance from tip to surface during approach and retraction of the tip. The inset shows a Lewis structure of the molecule on top of an STM image. This can be used to identify the position of the nitrogen atom at which the tip is connecting and pulling up the molecule. Picture taken from our publication [95].

First theoretical estimations of what was happening came from empirical force field geometry optimizations. They were suggesting that the aromatic system of the molecule breaks down and joins again multiple times when dragged up, as the angle of the aromatic rings relative to each other changes over time. We were to confirm these findings with more accurate DFT calculations, provide details on the binding characteristics and calculate the current through the optimized structures in order to explain the conductance features.

The project has been a joint effort of several groups in Germany, Spain and Italy [95]. By the author of this thesis, the initial geometry was constructed to model the experimental setup and later-on, binding curves and force calculations were added to the analysis. Another member of our group, Setianto, conducted snapshot geometry optimizations for the process of pulling up the molecule with an STM tip. Later, our colleagues in Rome calculated the current through these structures and compared them with the experiment. This chapter will mainly focus on the details of the theoretical calculations that were conducted within this thesis, for a more thorough description of the experimental setup and the current calculations we refer to the mentioned publication.

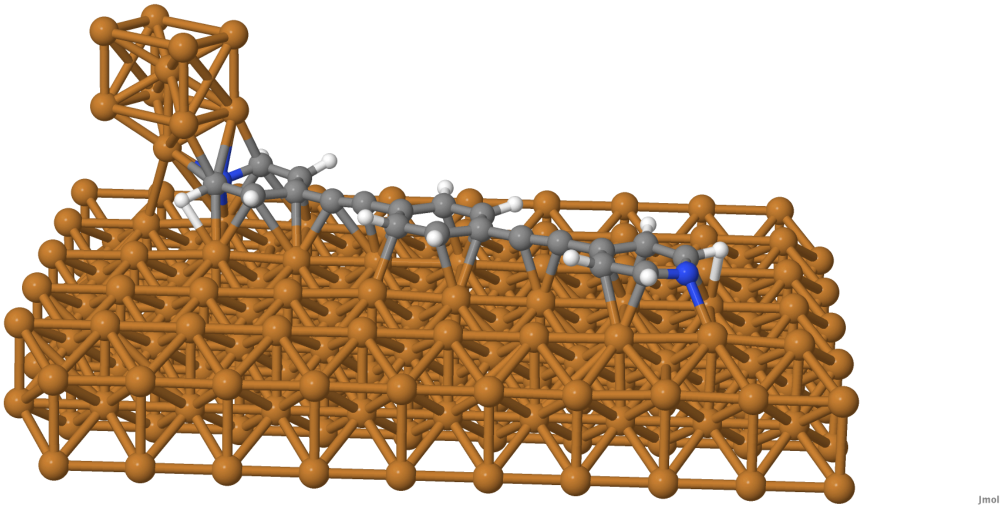

Figure 5.2: The setup: BPEB lying flat on a copper surface and being picked up with a simulated copper STM tip.

A visualization of the setup can be seen in Fig. 5.2. The first step was the recreation of the system geometry which was most likely present in experiment. Since it took place in a low temperature environment (5K), the global minimum of the potential energy surface (PES) had to be found to start from the correct orientation of the molecule on the surface.

5.2. The initial geometry

First, the copper surface itself had to be created. All DFT calculations were carried out with the Siesta software package [96] using public pseudo-potentials which were provided on the Siesta homepage and originate from the AbInit [97] project. The LDA potentials are constructed using Ceperley-Alderley correlation terms [98], the PBE pseudo-potentials are of the Troullier-Martins [99] type. In order to construct the surface, a copper fcc primitive unit cell was relaxed in a bulk environment by the use of periodic boundary conditions and a (8x8x8) Monkhorst-Pack mesh [100]. The LDA functional was used in conjunction with a special basis set for copper which is optimized for the description of bulks [101]. With the resulting lattice constant, larger cells (24 and later 96 atoms) were subsequently created and again optimized, which led to small corrections. Following this procedure, the resulting bulk lattice constant (a_{LDA} = 3.56 Å) is a bit smaller than the experimental one (a_{exp} = 3.60 Å) [102] and larger than the LDA bulk lattice constant reported in the literature ($a_{LDA-Lit}$ = 3.53 Å) [103]. The underestimation of lattice constants is a general property of LDA, while our deviation from other LDA calculations can be attributed to our special basis set which should yield better results.

Using our result, a surface consisting of a total of 280 copper atoms and four layers was created. The two topmost layers which will later point towards the molecule were again relaxed with LDA and the special basis set. In a separate calculation, the geometry of the molecule was optimized using LDA and a double-zeta basis set with polarization functions (DZP) in the gas phase. In order to get a rough estimate of the binding distance between surface and molecule, single point calculations at fixed geometry for varying distances were carried out. For the description of the final system, the PBE functional including van-der-Waals interactions approximated by the use of a Grimme s6 potential [104] would surely be more accurate than LDA. However, the calculations would be considerably more expensive which led us to testing if the LDA might be good enough, since its systematical overbinding leads to error correction with its lack of a description of van der Waals interactions. The binding distance predicted by the mentioned single-point calculations for PBE-vdW of $z_{PBE} = 2.4$Å was close to and still larger than the prediction of LDA without any vdW-interactions, $z_{LDA} = 2.25$Å, justifying the usage of the LDA for all further calculations. Note that these binding distances result from unrelaxed single point calculations with a flat, inflexible molecule. The binding distance upon full relaxation may vary slightly.

From the experiment the exact location and orientation of the molecule on the surface was unknown. In order to find the global minimum of the potential energy surface, the whole system geometry was fully LDA-optimized from various initial guesses, while only the topmost copper layer was allowed to relax along with the molecule. The molecule-surface distance was set to be near the previously found optimum. In order to test all possible orientations on the surface, the molecule was rotated by various angles (six rotations of 15 degrees each were enough due to symmetry) in each of seven initial positions relative to the surface copper atoms (42 combinations in total). The optimal, diagonal orientation of the molecule allowed some copper atoms to be cut out, leaving a surface of 200 atoms. In all of these and the following calculations, only the Gamma point was used. The mesh grid cutoff was set to 200 Ry (for details please consult the Siesta manual). Finally, the result can be seen in Fig. 5.3. To this optimized geometry, a static copper STM tip consisting of 10 atoms was added, docking at one of the nitrogens (blue). The flat adsorption of the molecule is in agreement with the STM images.

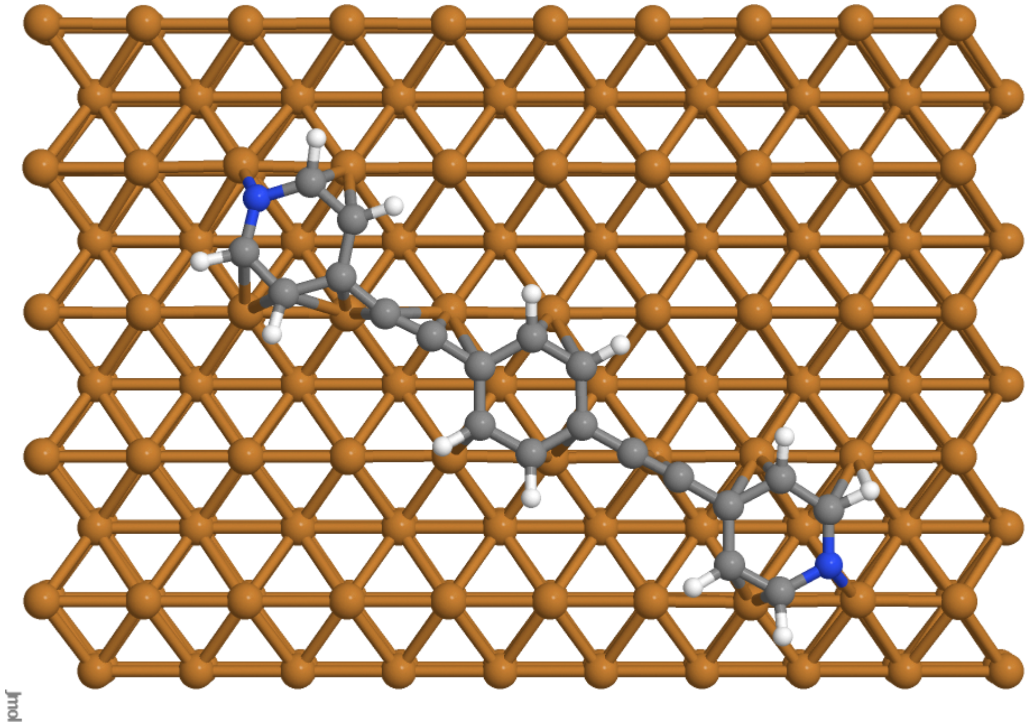

Figure 5.3: The fully optimized initial geometry with the energetically most favorable molecule orientation (LDA).

5.3. Conformational Changes during retraction

The following is a short and selective summary of the theoretical results obtained by our co-workers trying to explain the experimentally observed behaviour. After the initial geometry had been constructed, geometry optimizations at DFT-LDA level using the special basis set for Cu and a DZP basis set for the other atoms were carried out. The tip was placed above one of the nitrogen atoms of its respective pyridine group, which in turn centered above a copper surface atom, as can be seen in Fig. 5.4 a.). Keeping all copper atoms (surface and tip) fixed, the tip was now raised by 24 steps of 0.25 Å, fully relaxing the molecule in each.

The calculations hint that the first pyridine ring forms a single-molecule junction which is present in a certain distance range between tip and surface. These observations are in line with the general features of the conductance measurements in experiment. For a more detailed explanation, see Fig. 5.4 c-f.).

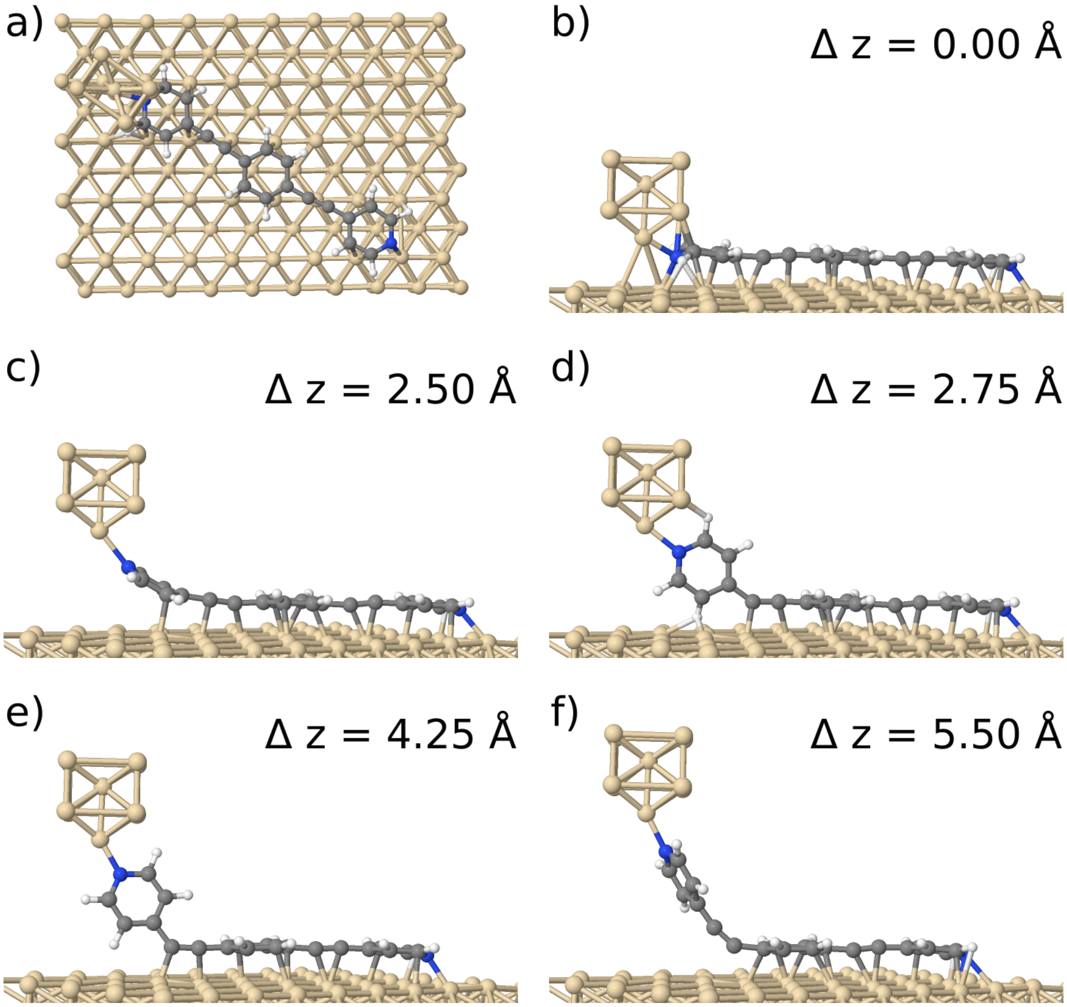

Figure 5.4: Conformational changes during the process of pulling up the molecule. $\Delta z = z - z_0$ is the tip displacement with respect to the initial distance of the tip to the molecule of $z_0 = 2.76$ Å. **a.), b.)** Starting geometry including tip from the top and sideways. **c.)** The tip is being pulled up and the molecule detaches. The conductance decreases, which corresponds to $A \rightarrow B$ in Fig. 5.1. **d.)** The bond angle of the pulled-up pyridine ring with the body of the molecule rotates by 90 degrees. The respective bond loses sp-character and the ring is now bridging to the surface. The conductance increases sharply (point B). **e.)** The anchoring direct bond breaks, the conductance drops again (point C). **f.)** The first ring rotates back to its original confirmation, the initial decline of the conductance continues (beyond point C onwards).

5.4. Binding energy and forces

Another contribution to the project by the author of this thesis is the calculation and comparison of binding energies and in consequence, also the forces acting on the tip. The analysis was done for the LDA functional and the PBE functional including van-der-Waals interactions as introduced earlier. Intuitively, the binding energy E_{Bind} used is defined as

$$E_{Bind}(z) = E_{T+S+M}(z) - E_S - E_{T+M} \tag{5.1}$$

with E_{T+S+M} being the energy of the final system, E_S the energy of the fully relaxed surface alone and E_{T+M} the energy of the fully relaxed tip+molecule alone. Note that the latter geometry can and will be significantly different from the orientation of the molecule on the surface. The accuracy of determining such a binding energy suffers from the basis set superposition error (BSSE), a consequence of the finite basis sets used. In short range interactions, the basis sets will overlap, therefore increase the basis set size and improve the description of the respective atoms, while this is not possible for larger interaction distances. There are ex-ante and ex-post ways of correcting for this error, we choose the popular counterpoise correction [105]. There is no feature in the Siesta package to correct the BSSE automatically. However, the code offers to define so-called *ghost* atoms which do not interact at all, but their respective basis functions are still centered at the specified positions. These ghost atoms can be used to calculate the counterpoise correction [106] [107].

In order to test the setup and the application of the correction under known circumstances, a benzene ring adsorbing on a Cu(110) surface was constructed. We obtained a LDA binding energy of $E_{Bind} = 1.04$ eV, well in line with the theoretical ($E_{Bind_{theo}} = 1.10$ eV [108]) and experimental ($E_{Bind_{exp}} = 1.03$ eV [109]) literature, previously correcting for a severe overestimation introduced by the BSSE. We are therefore confident to accurately predict the binding energy of a very similar system as the one shown in Fig. 5.2.

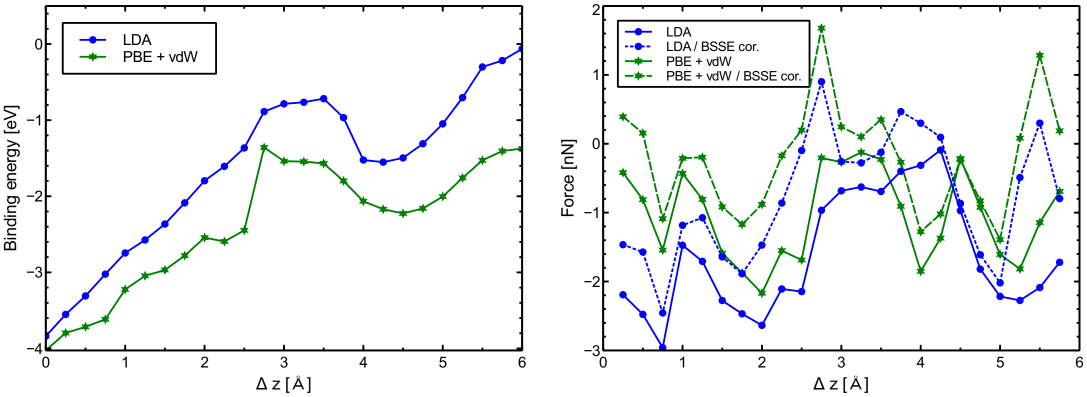

Figure 5.5: **Left:** Binding energies for the LDA functional and the PBE functional with Grimme-type van der Waals interactions, respectively. **Right:** Calculated forces on the tip with and without the counterpoise correction to the BSSE for both functionals.

Since the geometry optimization steps during retraction of the tip were only carried out at LDA level, we were limited to compare the binding energies of LDA and PBE on these LDA-optimized geometries alone. However, the PBE-vdW results only play the role of additional information, since LDA was used throughout the whole project. In Fig. 5.5, one can see the binding energies of LDA and PBE-vDW, respectively. Also shown are the forces acting on the tip, which are described by the sum of all forces in z-direction acting on the tip atoms. The forces yet uncorrected and coming straight out of the DFT calculations are available from the code output. However, the ex-post counterpoise correction provides only distinct values at each geometry step, and its force contribution has to be calculated by the use of numerical derivatives. Since the individual displacement between the geometry steps is rather large (Δz = 0.25 Å), so is the relative error introduced. We show the obtained forces in Fig. 5.5 with and without the counterpoise correction applied. One can see that its effect is significant.

5.5. Short summary

We discussed a project investigating the conformational changes of an oligophenyl molecule when being lifted off a copper surface by an STM tip. The experimentally observed jumps in the conductance could be explained with theoretical DFT-LDA calculations showing that one of the pyridine groups is rotating, bridging to the molecule and forming a single molecule junction. This junction is stable over the range of three Å in the mentioned calculations. Within this thesis, the initial geometry was constructed and for later analysis, the binding energies and forces on the tip were determined.

Chapter 6

Results and conclusions

We used a time-resolved transport approach on the basis of the Liouville-van Neumann equation for the reduced density matrix of the device region. It is combined with the efficient time-dependent density functional tight binding in order to make the expensive calculations feasible. As one of the possible applications, we analyzed ac transport through molecular junctions and atomic chains in order to gain information about their interaction with external radiation. We aimed to improve existing descriptions of the dynamic admittance and rectification properties of these systems. One major advantage is the explicit calculation of the time-dependent device potential distribution which is not captured in the existing frequency domain approaches to the sought-after quantities.

As for the dynamic admittance, we can easily distinguish between systems that act capacitively and such that act inductively. We find that ac transport is dominated by the metallic leads and the dc transmission of the molecule has only a very small influence away from the Fermi energy. In comparison to the current partitioning approach popular in the literature, we show that the correction introduced by taking into account the device potential distribution is very large for capacitive systems and a lot less significant for inductive systems. For the latter, we demonstrate that the agreement between both approaches is good if the potential distribution is flat as assumed by the current partitioning, and becomes increasingly worse when the distribution loses its flatness for higher frequencies. As an interesting test system due to vanishing dc current, we show that our methods describes capacitors correctly and also captures the geometrical capacitance ignored by the popular current partitioning approach.

Our description of photon-assisted tunneling is compared to the traditional, but inferior Tien-Gordon theory, which is only valid for small voltages and small frequencies, ignores the device potential distribution and falsely predicts a rectified current at vanishing dc bias for symmetric junctions. Our approach is not limited by any of these points and therefore vastly improves on Tien-Gordon. Given our experiences with the importance of the potential distribution for the dynamic admittance, we now additionally use larger voltages and therefore attribute the large disagreements of the approaches to the significant limitations of Tien-Gordon, especially in the optical regime and for finite bias. The dc transmission is again not carrying the information needed to predict the rectification properties of the systems. We also briefly demonstrate that a quasi-static approximation to the current is insufficient even in linear response to analyze higher harmonics and PAT.

In addition, we discussed a project in which a large, flexible, organic molecule is experimentally lifted off a copper surface using an STM tip. The conformational changes it experiences lead to characteristic jumps in the conductance, which are well described with time-independent DFT calculations.

Concluding, we show that the time-resolved approach in use fulfills the expectations of improving on the existing descriptions of PAT and the dynamic admittance. The effect of the time-dependent device potential distribution is significant, the method itself is fast enough even for systems with over a hundred atoms in the device region alone, and the qualitative results are in line with similar approaches. We therefore offer a way of interpreting experiments in the high frequency regime (optical). As for admittance properties, these frequencies are not yet accessible, while for PAT, the latter has to be identified in a regime where other, additional transport mechanisms play a role. Despite the difficulties to apply our predictions to the experiment, we offer a contribution to the theory behind the mentioned fields. It is also important to keep in mind that the approach is not limited to ac transport. Bias profiles of arbitrary shape and magnitude can be specified and leave applications like the analysis of transient current responses in large molecular systems to interested users.

Acknowledgements

First and foremost I would like to thank my supervisor, Prof. Thomas Niehaus, for all the support throughout the years. He managed to keep a great atmosphere while giving extensive guidance on the physical topics.
In addition, my thanks go out to Björn Korff for tremendous help with our code tranDFTB, Manohar Awasthi for technical support, Klaus Richter for co-refereeing my thesis, and Vitalij Lutsker for his friendship as a fellow PhD student.

References

[1]E. Scheer, *Molecular electronics: an introduction to theory and experiment*, vol. 1. World Scientific, 2010.

[2]G. Cuniberti, G. Fagas, and K. Richter, *Introducing molecular electronics: A brief overview.* Springer, 2005.

[3]A. Aviram and M. A. Ratner, "Molecular rectifiers," *Chemical Physics Letters*, vol. 29, no. 2, pp. 277–283, 1974.

[4]M. Galperin and A. Nitzan, "Optical properties of current carrying molecular wires," *The Journal of chemical physics*, vol. 124, no. 23, p. 234709, 2006.

[5]S. Battacharyya, A. Kibel, G. Kodis, P. A. Liddell, M. Gervaldo, D. Gust, and S. Lindsay, "Optical modulation of molecular conductance," *Nano letters*, vol. 11, no. 7, pp. 2709–2714, 2011.

[6]B. L. Feringa and W. R. Browne, *Molecular switches*, vol. 42. Wiley Online Library, 2001.

[7]S. Grafstrom, "Photoassisted scanning tunneling microscopy," *Journal of applied physics*, vol. 91, no. 4, pp. 1717–1753, 2002.

[8]D. C. Guhr, D. Rettinger, J. Boneberg, A. Erbe, P. Leiderer, and E. Scheer, "Influence of laser light on electronic transport through atomic-size contacts," *Physical review letters*, vol. 99, no. 8, p. 086801, 2007.

[9]P. Tien and J. Gordon, "Multiphoton process observed in the interaction of microwave fields with the tunneling between superconductor films," *Physical Review*, vol. 129, no. 2, p. 647, 1963.

[10]M. Anantram and S. Datta, "Effect of phase breaking on the ac response of mesoscopic systems," *Physical Review B*, vol. 51, no. 12, p. 7632, 1995.

[11]T. A. Niehaus, S. Suhai, F. Della Sala, P. Lugli, M. Elstner, G. Seifert, and T. Frauenheim, "Tight-binding approach to time-dependent density-functional response theory," *Physical Review B*, vol. 63, no. 8, p. 085108, 2001.

[12]T. A. Niehaus, D. Heringer, B. Torralva, and T. Frauenheim, "Importance of electronic self-consistency in the tddft based treatment of nonadiabatic molecular dynamics," *The European Physical Journal D-Atomic, Molecular, Optical and Plasma Physics*, vol. 35, no. 3, pp. 467–477, 2005.

[13]T. A. Niehaus, "Approximate time-dependent density functional theory," *Journal of Molecular Structure: THEOCHEM*, vol. 914, no. 1, pp. 38–49, 2009.

[14]J. K. Tomfohr and O. F. Sankey, "Time-dependent simulation of conduction through a molecule," *physica status solidi (b)*, vol. 226, no. 1, pp. 115–123, 2001.

[15]N. Bushong, N. Sai, and M. Di Ventra, "Approach to steady-state transport in nanoscale conductors," *Nano letters*, vol. 5, no. 12, pp. 2569–2572, 2005.

[16]S. Kurth, G. Stefanucci, C.-O. Almbladh, A. Rubio, and E. K. Gross, "Time-dependent quantum transport: A practical scheme using density functional theory," *Physical Review B*, vol. 72, no. 3, p. 035308, 2005.

[17]G. Stefanucci, S. Kurth, E. Gross, and A. Rubio, "Molecular and nano electronics: analysis, design and simulation," 2006.

[18]G. Stefanucci, S. Kurth, A. Rubio, and E. Gross, "Time-dependent approach to electron pumping in open quantum systems," *Physical Review B*, vol. 77, no. 7, p. 075339, 2008.

[19]D. Porezag, T. Frauenheim, T. Köhler, G. Seifert, and R. Kaschner, "Construction of tight-binding-like potentials on the basis of density-functional theory: Application to carbon," *Physical Review B*, vol. 51, no. 19, p. 12947, 1995.

[20]Y. Wang, C.-Y. Yam, T. Frauenheim, G. Chen, and T. A. Niehaus, "An efficient method for quantum transport simulations in the time domain," *Chemical Physics*, vol. 391, no. 1, pp. 69–77, 2011.

[21]K. Capelle, "A bird's-eye view of density-functional theory," *Brazilian Journal of Physics*, vol. 36, no. 4A, pp. 1318–1343, 2006.

[22]C. Fiolhais, F. Nogueira, and M. A. Marques, *A primer in density functional theory*, vol. 620. Springer, 2003.

[23]F. Jensen, *Introduction to computational chemistry.* John Wiley & Sons, 2007.

[24]P. Hohenberg and W. Kohn, "Inhomogeneous electron gas," *Phys. Rev.*, vol. 136, pp. B864–B871, Nov 1964.

[25]W. Kohn and L. J. Sham, "Self-consistent equations including exchange and correlation effects," *Phys. Rev.*, vol. 140, pp. A1133–A1138, Nov 1965.

[26]R. G. Parr and W. Yang, *Density-functional theory of atoms and molecules*, vol. 16. Oxford university press, 1989.

[27]T. Koopmans, "Über die zuordnung von wellenfunktionen und eigenwerten zu den einzelnen elektronen eines atoms," *Physica*, vol. 1, no. 1, pp. 104–113, 1934.

[28]E. J. Baerends and O. V. Gritsenko, “A quantum chemical view of density functional theory,” *The Journal of Physical Chemistry A*, vol. 101, no. 30, pp. 5383–5403, 1997.

[29]E. K. Gross and R. M. Dreizler, *Density functional theory*. Springer, 1995.

[30]J. P. Perdew and Y. Wang, “Accurate and simple analytic representation of the electron-gas correlation energy,” *Phys. Rev. B*, 1992.

[31]O. Gunnarsson and B. I. Lundqvist, “Exchange and correlation in atoms, molecules, and solids by the spin-density-functional formalism,” *Phys. Rev. B*, 1976.

[32]J. P. Perdew, K. Burke, and M. Ernzerhof, “Generalized gradient approximation made simple,” *Physical review letters*, vol. 77, no. 18, p. 3865, 1996.

[33]J. C. Slater and G. F. Koster, “Simplified lcao method for the periodic potential problem,” *Physical Review*, vol. 94, no. 6, p. 1498, 1954.

[34]C. Goringe, D. Bowler, and E. Hernandez, “Tight-binding modelling of materials,” *Reports on Progress in Physics*, vol. 60, no. 12, p. 1447, 1997.

[35]D. Chadi, “Atomic and electronic structures of reconstructed si (100) surfaces,” *Physical Review Letters*, vol. 43, no. 1, p. 43, 1979.

[36]W. M. C. Foulkes and R. Haydock, “Tight-binding models and density-functional theory,” *Physical review B*, vol. 39, no. 17, p. 12520, 1989.

[37]M. Elstner, D. Porezag, G. Jungnickel, J. Elsner, M. Haugk, T. Frauenheim, S. Suhai, and G. Seifert, “Self-consistent-charge density-functional tight-binding method for simulations of complex materials properties,” *Physical Review B*, vol. 58, no. 11, p. 7260, 1998.

[38]H. Eschrig, “Optimized lcao method and the electronic structure of extended systems,” *Series: Research Reports in Physics, ISBN: 978-3-662-02564-2. Springer Berlin Heidelberg (Berlin, Heidelberg), Edited by Helmut Eschrig*, vol. 1, 1989.

[39]R. Pariser, “Theory of the electronic spectra and structure of the polyacenes and of alternant hydrocarbons,” *The Journal of Chemical Physics*, vol. 24, no. 2, pp. 250–268, 1956.

[40]L. P. Kadanoff and G. Baym, *Quantum statistical mechanics: Green’s function methods in equilibrium and nonequilibrium problems*. Benjamin New York, 1962.

[41]S. Datta, *Electronic transport in mesoscopic systems*. Cambridge university press, 1997.

[42]R. Landauer, “Spatial variation of currents and fields due to localized scatterers in metallic conduction,” *IBM Journal of Research and Development*, vol. 1, no. 3, pp. 223–231, 1957.

[43]M. Büttiker, “Four-terminal phase-coherent conductance,” *Physical Review Letters*, vol. 57, no. 14, p. 1761, 1986.

[44]J. Taylor, H. Guo, and J. Wang, “Ab initio modeling of quantum transport properties of molecular electronic devices,” *Physical Review B*, vol. 63, no. 24, p. 245407, 2001.

[45]F. Evers, F. Weigend, and M. Koentopp, “Conductance of molecular wires and transport calculations based on density-functional theory,” *Physical Review B*, vol. 69, no. 23, p. 235411, 2004.

[46]M. Di Ventra, *Electrical transport in nanoscale systems*, vol. 14. Cambridge University Press Cambridge, 2008.

[47]Y. Meir and N. S. Wingreen, “Landauer formula for the current through an interacting electron region,” *Physical review letters*, vol. 68, no. 16, p. 2512, 1992.

[48]D. S. Fisher and P. A. Lee, “Relation between conductivity and transmission matrix,” *Physical Review B*, vol. 23, no. 12, pp. 6851–6854, 1981.

[49]A. M. Zagoskin, *Quantum theory of many-body systems.* Springer, 1998.

[50]D. C. Langreth and P. Nordlander, “Derivation of a master equation for charge-transfer processes in atom-surface collisions,” *Physical Review B*, vol. 43, no. 4, p. 2541, 1991.

[51]G. H. Chen, C. Y. Yam, S. Yokojima, W. Z. Liang, X. J. Wang, F. Wang, and X. Zheng, “http://yangtze.hku.hk/lodestar/lodestar.php,”

[52]X. Zheng, F. Wang, C. Y. Yam, Y. Mo, and G. Chen, “Time-dependent density-functional theory for open systems,” *Physical Review B*, vol. 75, no. 19, p. 195127, 2007.

[53]J. Riess and W. Münch, “The theorem of hohenberg and kohn for subdomains of a quantum system,” *Theoretica chimica acta*, vol. 58, no. 4, pp. 295–300, 1981.

[54]M. Cini, “Time-dependent approach to electron transport through junctions: General theory and simple applications,” *Physical Review B*, vol. 22, no. 12, p. 5887, 1980.

[55]A. P. Jauho, N. Wingreen, and Y. Meir, “Time-dependent transport in interacting and noninteracting resonant-tunneling systems,” *Phys. Rev. B, Vol. 50 Nr.8*, 1994.

[56]S. Yokojima, G. Chen, R. Xu, and Y. Yan, "A dynamic mean-field theory for dissipative interacting many-electron systems," *Chemical physics letters*, vol. 369, no. 3, pp. 495–503, 2003.

[57]X. Zheng, F. Wang, and G. H. Chen, "arxiv:quant-ph/0606169," *unpublished*, 2006.

[58]T. A. Niehaus, M. Rohlfing, F. Della Sala, A. Di Carlo, and T. Frauenheim, "Quasiparticle energies for large molecules: A tight-binding-based green's-function approach," *Physical Review A*, vol. 71, no. 2, p. 022508, 2005.

[59]C. G. Broyden, "The convergence of a class of double-rank minimization algorithms 1. general considerations," *IMA Journal of Applied Mathematics*, vol. 6, no. 1, pp. 76–90, 1970.

[60]A. Pecchia, G. Penazzi, L. Salvucci, and A. Di Carlo, "Non-equilibrium green's functions in density functional tight binding: method and applications," *New Journal of Physics*, vol. 10, no. 6, p. 065022, 2008.

[61]M. L. Sancho, J. L. Sancho, and J. Rubio, "Highly convergent schemes for the calculation of bulk and surface green functions," *Journal of Physics F: Metal Physics*, vol. 15, no. 4, p. 851, 1985.

[62]W. Witt, "An absolute precision measurement of lattice constants on ge and al monocrystals with electron diffraction," *Z Naturforsch.*, vol. 22, no. 1, pp. 92–95, 1967.

[63]C. Oppenländer, B. Korff, T. Frauenheim, and T. A. Niehaus, "Atomistic modeling of dynamical quantum transport," *physica status solidi (b)*, vol. 250, no. 11, pp. 2349–2354, 2013.

[64]C. Yam, X. Zheng, G. Chen, Y. Wang, T. Frauenheim, and T. A. Niehaus, "Time-dependent versus static quantum transport simulations beyond linear response," *Physical Review B*, vol. 83, no. 24, p. 245448, 2011.

[65]Y. Yu, B. Wang, and Y. Wei, "ac response of a carbon chain under a finite frequency bias," *The Journal of chemical physics*, vol. 127, no. 10, p. 104701, 2007.

[66]K. Sasaoka, T. Yamamoto, S. Watanabe, and K. Shiraishi, "ac response of quantum point contacts with a split-gate configuration," *Physical review B*, vol. 84, no. 12, p. 125403, 2011.

[67]T. Yamamoto, K. Sasaoka, and S. Watanabe, "Universal transition between inductive and capacitive admittance of metallic single-walled carbon nanotubes," *Physical Review B*, vol. 82, no. 20, p. 205404, 2010.

[68]D. Hirai, T. Yamamoto, and S. Watanabe, “Theoretical analysis of ac transport in carbon nanotubes with a single atomic vacancy: Sharp contrast between dc and ac responses in vacancy position dependence,” *Applied Physics Express*, vol. 4, no. 7, p. 075103, 2011.

[69]C. Yam, Y. Mo, F. Wang, X. Li, G. Chen, X. Zheng, Y. Matsuda, J. Tahir-Kheli, and W. A. Goddard Iii, “Dynamic admittance of carbon nanotube-based molecular electronic devices and their equivalent electric circuit,” *Nanotechnology*, vol. 19, no. 49, p. 495203, 2008.

[70]Y. Fu and S. C. Dudley, “Quantum inductance within linear response theory,” *Physical review letters*, vol. 70, no. 1, pp. 65–68, 1993.

[71]B. Dutta and B. Dayal, “Lattice constants and thermal expansion of gold up to 878 c by x-ray method,” *physica status solidi (b)*, vol. 3, no. 3, pp. 473–477, 1963.

[72]A.-P. Jauho, N. S. Wingreen, and Y. Meir, “Time-dependent transport in interacting and noninteracting resonant-tunneling systems,” *Physical Review B*, vol. 50, no. 8, p. 5528, 1994.

[73]M. H. Hettler and H. Schoeller, “Anderson model out of equilibrium: time-dependent perturbations,” *Physical review letters*, vol. 74, no. 24, p. 4907, 1995.

[74]M. Büttiker, A. Prêtre, and H. Thomas, “Dynamic conductance and the scattering matrix of small conductors,” *Physical review letters*, vol. 70, no. 26, p. 4114, 1993.

[75]B. Wang, J. Wang, and H. Guo, “Current partition: A nonequilibrium green’s function approach,” *Physical review letters*, vol. 82, no. 2, p. 398, 1999.

[76]Y. Zhenyu, *Quantum transport theory for AC response and its combination with the electromagnetic method.* PhD thesis, 2014.

[77]S. Luryi, “Quantum capacitance devices,” *Applied Physics Letters*, vol. 52, no. 6, pp. 501–503, 1988.

[78]T. Smith, B. Goldberg, P. Stiles, and M. Heiblum, “Direct measurement of the density of states of a two-dimensional electron gas,” *Physical Review B*, vol. 32, no. 4, pp. 2696–2699, 1985.

[79]M. Büttiker, “Capacitance, admittance, and rectification properties of small conductors,” *Journal of Physics: Condensed Matter*, vol. 5, no. 50, p. 9361, 1993.

[80]M. Büttiker, H. Thomas, and A. Prêtre, “Mesoscopic capacitors,” *Physics Letters A*, vol. 180, no. 4, pp. 364–369, 1993.

[81]J. Wang, B. Wang, and H. Guo, "Quantum inductance and negative electrochemical capacitance at finite frequency in a two-plate quantum capacitor," *Physical Review B*, vol. 75, no. 15, p. 155336, 2007.

[82]P. Cutler, T. Feuchtwang, T. Tsong, Y. Kuk, H. Nguyen, and A. Lucas, "Proposed use of a scanning-tunneling-microscope tunnel junction for the measurement of a tunneling time," *Physical Review B*, vol. 35, no. 14, p. 7774, 1987.

[83]M. Völcker, W. Krieger, and H. Walther, "Laser-driven scanning tunneling microscope," *Physical review letters*, vol. 66, no. 13, p. 1717, 1991.

[84]G. Platero and R. Aguado, "Photon-assisted transport in semiconductor nanostructures," *Physics Reports*, vol. 395, no. 1, pp. 1–157, 2004.

[85]R. Arielly, A. Ofarim, G. Noy, and Y. Selzer, "Accurate determination of plasmonic fields in molecular junctions by current rectification at optical frequencies," *Nano letters*, vol. 11, no. 7, pp. 2968–2972, 2011.

[86]D. R. Ward, F. Hüser, F. Pauly, J. C. Cuevas, and D. Natelson, "Optical rectification and field enhancement in a plasmonic nanogap," *Nature nanotechnology*, vol. 5, no. 10, pp. 732–736, 2010.

[87]J. R. Tucker and M. J. Feldman, "Quantum detection at millimeter wavelengths," *Reviews of Modern Physics*, vol. 57, no. 4, p. 1055, 1985.

[88]J. Viljas and J. Cuevas, "Role of electronic structure in photoassisted transport through atomic-sized contacts," *Physical Review B*, vol. 75, no. 7, p. 075406, 2007.

[89]J. K. Viljas, F. Pauly, and J. C. Cuevas, "Modeling elastic and photoassisted transport in organic molecular wires: Length dependence and current-voltage characteristics," *Physical Review B*, vol. 77, no. 15, p. 155119, 2008.

[90]A.-P. Jauho, "Photon side-bands in mesoscopics," *arXiv preprint cond-mat/9711141*, 1997.

[91]M. H. Pedersen and M. Büttiker, "Scattering theory of photon-assisted electron transport," *Physical Review B*, vol. 58, no. 19, p. 12993, 1998.

[92]C. Oppenländer, B. Korff, and T. A. Niehaus, "Higher harmonics and ac transport from time dependent density functional theory," *Journal of Computational Electronics*, vol. 12, no. 3, pp. 420–427, 2013.

[93]X. Tu, J. Lee, and W. Ho, "Atomic-scale rectification at microwave frequency," *The Journal of chemical physics*, vol. 124, no. 2, pp. 021105–021105, 2006.

[94]D. Ward, G. Scott, Z. Keane, N. Halas, and D. Natelson, "Electronic and optical properties of electromigrated molecular junctions," *Journal of Physics: Condensed Matter*, vol. 20, no. 37, p. 374118, 2008.

[95]C. Lotze, J. Li, C. Herranz-Lancho, G. Schulze, M. Corso, Setianto, C. Oppenländer, M. Ruben, K. J. Franke, A. Pecchia, T. A. Niehaus, and J. I. Pascual, “The effect of conformational flexibility on the electrical transport through flexible molecules,” *to be published*, 2014.

[96]J. M. Soler, E. Artacho, J. D. Gale, A. García, J. Junquera, P. Ordejón, and D. Sánchez-Portal, “The siesta method for ab initio order-n materials simulation,” *Journal of Physics: Condensed Matter*, vol. 14, no. 11, p. 2745, 2002.

[97]X. Gonze, J.-M. Beuken, R. Caracas, F. Detraux, M. Fuchs, G.-M. Rignanese, L. Sindic, M. Verstraete, G. Zerah, F. Jollet, *et al.*, “First-principles computation of material properties: the abinit software project,” *Computational Materials Science*, vol. 25, no. 3, pp. 478–492, 2002.

[98]D. M. Ceperley and B. J. Alder, “Ground state of the electron gas by a stochastic method,” *Phys. Rev. Lett.*, vol. 45, pp. 566–569, Aug 1980.

[99]N. Troullier and J. L. Martins, “Efficient pseudopotentials for plane-wave calculations,” *Phys. Rev. B*, vol. 43, pp. 1993–2006, Jan 1991.

[100]H. J. Monkhorst and J. D. Pack, “Special points for brillouin-zone integrations,” *Physical Review B*, vol. 13, no. 12, p. 5188, 1976.

[101]S. García-Gil, A. García, N. Lorente, and P. Ordejon, “Optimal strictly localized basis sets for noble metal surfaces,” *Physical Review B*, vol. 79, no. 7, p. 075441, 2009.

[102]P. Haas, F. Tran, and P. Blaha, “Calculation of the lattice constant of solids with semilocal functionals,” *Physical Review B*, vol. 79, no. 8, p. 085104, 2009.

[103]V. N. Staroverov, G. E. Scuseria, J. Tao, and J. P. Perdew, “Tests of a ladder of density functionals for bulk solids and surfaces,” *Physical Review B*, vol. 69, no. 7, p. 075102, 2004.

[104]S. Grimme, “Semiempirical gga-type density functional constructed with a long-range dispersion correction,” *Journal of computational chemistry*, vol. 27, no. 15, pp. 1787–1799, 2006.

[105]S. F. Boys and F. d. Bernardi, “The calculation of small molecular interactions by the differences of separate total energies. some procedures with reduced errors,” *Molecular Physics*, vol. 19, no. 4, pp. 553–566, 1970.

[106]C. Hobbs, L. Kantorovich, and J. D. Gale, “An ab initio study of c60 adsorption on the si (001) surface,” *Surface science*, vol. 591, no. 1, pp. 45–55, 2005.

[107]C. Song, Y. Xia, M. Zhao, X. Liu, B. Huang, F. Li, and Y. Ji, "Self-assembly of base-functionalized carbon nanotubes," *Physical Review B*, vol. 72, no. 16, p. 165430, 2005.

[108]B. Rogers, J. Shapter, and M. J. Ford, "Ab initio study of benzene adsorption on the cu (110) surface and simulation of stm images," *Surface science*, vol. 548, no. 1, pp. 29–40, 2004.

[109]J. R. Lomas, C. J. Baddeley, M. S. Tikhov, and R. M. Lambert, "Ethyne cyclization to benzene over cu (110)," *Langmuir*, vol. 11, no. 8, pp. 3048–3053, 1995.